STATUS REPORTS

to the

PAPERMAKING

PROJECT ADVISORY COMMITTEE

VOLUME II

March 23, 1998

INSTITUTE OF PAPER SCIENCE AND TECHNOLOGY

Atlanta, Georgia

ANNUAL PROGRAM REVIEW

PAPERMAKING

VOLUME II

March 23, 1998

February 16, 1998

TO: MEMBERS OF THE PAPERMAKING PROJECT ADVISORY COMMITTEE

Attached for your review are the Status Reports for the projects to be discussed at the Papermaking Project Advisory Committee meeting being held at the Institute of Paper Science and Technology. The Program Review is scheduled for Monday, March 23, 1998, from 1:00 p.m. to 5:00 p.m. and the PAC Committee Meeting will meet on Tuesday, March 24, from 1:00 p.m. to 5:00 p.m.

We look forward to seeing you at this time.

Sincerely,

David I. Orloff

David I. Orloff, Ph.D.
Professor of Engineering & Director
Engineering and Paper Materials Division

DIO/map

Attachments

Institute of Paper Science and Technology, Inc.

500 10th Street, N.W.
Atlanta, GA 30318-5794

Telephone 404-894-5700
FAX# 404-894-IPST (4778)

PAPERMAKING
PROJECT ADVISORY COMMITTEE

IPST Liaison: Dr. David Orloff (404) 894-6649; FAX (404) 894-1496
RAC Liaison: Mr. John Bergin (715) 422-2239; FAX (715) 422-2227

Dr. Dwight E. Anderson *(2001)
Project Manager
Weyerhaeuser Company
WTC 2F39
Post Office Box 2999
Tacoma, WA 98477-2999
(253) 924-6466
(253) 924-6541 FAX

Mr. Jack Burke *(1999)
Principle Project Manager
Radian International LLC
1979 Lakeside Parkway
Suite 800
Tucker, GA 30084
(770) 414-4522
(770) 414-4919 FAX

Mr. William O. Burns *(1999)
Director, Manufacturing Technology
Fort James Corporation
1915 Marathon Avenue
Post Office Box 899
Neenah, WI 54957-0899
(920) 729-8437
(920) 729-8597 FAX

Dr. Partha S. Chaudhuri *(1999)
Senior Scientist, Papermaking
Champion International Corporation
Technical Center
West Nyack Road
West Nyack, NY 10994
(914) 578-7123
(914) 578-7474 FAX

Mr. Frank Cunnane *(1999)
Vice President, Technology
Asten, Inc.
4399 Corporate Road
Post Office Box 118001
Charleston, SC 29423
(803) 747-7800
(803) 747-3856 FAX

Mr. Marcel Dauth *(1998)
St. Laurent Paperboard Inc.
630 Rene Levesque Blvd, West
Suite 3000
Montreal, Quebec H3B 5C7, CANADA
(514) 864-5108
(514) 861-9559 FAX

Dr. Christopher P. Devlin *(2001)
Process Engineering Manager
Inland Eastex
A Temple-Inland Company
Post Office Box 816
Silsbee, TX 77656
(409) 276-3190
(409) 276-3419 FAX
cdevlin@iccnet.com

Mr. William Haskins *(1998)
Market Development Manager
Specialty Minerals Inc.
35 Highland Avenue
Bethlehem, PA 18017
(610) 882-8652
(610) 882-8760 FAX

Mr. Neil E. Johnson *(2000)
Research Engineering
Potlatch Corporation
20 North 22nd Street
Cloquet, MN 55720
(218) 879-2321
(218) 879-2375 FAX

Dr. Charles Kramer *(1998)
Director
Albany International Research Company
Post Office Box 9114
Mansfield, MA 02048
(508) 337-9541
(508) 339-4996 FAX

Mr. David J. Lacz *(2001)
Technical Associate
Eastman Kodak Company
Paper Support Division B-319
1669 Lake Avenue
Rochester, NY 14652-3622
(716) 477-6301
(716) 588-2680 FAX
dlacz@kodak.com

Mr. Joseph P. MacDowell *(1999)
Research Project Supervisor - Coated
and Uncoated
P.H. Glatfelter Co.
228 South Main Street
Spring Grove, PA 17362-1000
(717) 225-4711
(717) 225-7454 FAX
jmacdowell@glatfelter.com

* The dates in ( ) indicate the final year of the appointment.

Dr. Michael Marziale *(1999)
Technical Assistant to the Wickliffe Mill Manager
Westvaco Corporation
1724 Westvaco Road
Post Office Box 278
Wickliffe, KY 42087-0278
(502) 335-4203
(502) 335-4101 FAX

Mr. Vic Nisita *(2001)
Operations Superintendent
Wisconsin Tissue Mills
Chicago Operations
13101 S. Polaski Road
Alsip, IL 60658
(708) 824-4397
(708) 389-4901 FAX

Dr. Franco Palumbo *(1997)
Riverwood International Corporation
Post Office Box 35800
West Monroe, LA 71294-5800
(318) 362-2000
(318) 362-2133 FAX

Mr. Jason R. Panek *(2001)
Technical Director
Manistique Papers
453 S. Mackinac Avenue
Manistique, MI 49854
(906) 341-2175
(906) 341-5635 FAX

Dr. Paul R. Proxmire *(2001)
Research Associate
Appleton Papers Inc.
Post Office Box 359
Appleton, WI 54912-0359
(920) 730-7254
(920) 991-7243 FAX

Mr. Jeffrey R. Reese *(2001)
Consultant, Paper Mill
Georgia-Pacific Corporation
133 Peachtree Street, NE
18th Floor
Atlanta, GA 30303
(404) 652-4880
(404) 584-1466 FAX
JReese@GAPAC.com

Mr. Thomas E. Rodencal *(Alternate)
Sr. Paper Mill Staff Engineer
Georgia-Pacific Corporation
133 Peachtree Street, NE
18th Floor
Atlanta, GA 30303
(404) 652-4514
(404) 584-1466 FAX

Mr. John Rogers *(1997)
Technical Director
Sandusky International Inc.
Post Office Box 5012
Sandusky, OH 44870-8012
(419) 626-5340
(419) 626-8674 FAX

Dr. Jay A. Shands *(2001)
Manager, Forming Systems
Beloit Corporation
Rockton Research Center
1165 Prairie Hill Road
Rockton, IL 61072-1595
(608) 364-8501
(608) 364-8600 FAX

Mr. Stephen G. Simmons *(1998)
Technical Manager, Fiber Development
The Mead Corporation
Mead Central Research Laboratories
232 Eighth Street
Chillicothe, OH 45601-5700
(614) 772-3051
(614) 772-3595 FAX
stephen_simmons@mead.com

Mr. Jay Thiessen *(2000)
Consolidated Papers, Inc.
Post Office Box 8050
Wisconsin Rapids, WI 54495-8050
(715) 422-1616
(715) 422-1639 FAX

Mr. David G. Thurman *(Alternate)
Project Leader, Board
EKA Chemicals Inc.
2211 Newmarket Parkway
Suite 106
Marietta, GA 30067

* The dates in ( ) indicate the final year of the appointment.

Revised 02/03/98:at

Mr. Thomas K. Toothman *(Alternate)
Paper Mill Superintendent
Wisconsin Tissue Mills Inc.
Third & Tayco Streets
Post Office Box 489
Menasha, WI 54952
(920) 725-2431
(920) 727-2940 FAX

Mr. Lloyd O. Westling *(1999)
Vice President, Production Planning
Longview Fibre Company
Post Office Box 639
Longview, WA 98632
(360) 425-1550
(360) 575-5925 FAX

Mr. Jim Watson *(2001)
Sr. Technical Sales Representative
EKA Chemicals Inc.
2211 Newmarket Parkway
Suite 106
Marietta, GA 30067

Dr. David E. White *(2001) (Chairman)
Research Associate
Union Camp Corporation
Post Office Box 3301
Princeton, NJ 08543-3301
(609) 844-7249
(609) 844-7366 FAX
Dave_E._ White@ucamp.com

* The dates in ( ) indicate the final year of the appointment.

Revised 02/03/98:at

PAPERMAKING
PROJECT ADVISORY COMMITTEE MEETING

March 23, 1998

Institute of Paper Science and Technology
Atlanta, Georgia

PROGRAM REVIEW AGENDA

Seminar Room 114

1:00 p.m. - 1:10 p.m.	Opening Remarks Review Antitrust Statement Confidentiality Statement		David White
1:10 p.m. - 1:25 p.m.	Welcome from Vice President of Research		Gary Baum
1:25 p.m. - 1:35 p.m.	Overview of IPST Papermaking Research		David Orloff
1:35 p.m. - 2:10 p.m.	Project F004	Approach Pipe Systems	Xiaodong Wang
2:10 p.m. - 2:55 p.m.	Project F005	Headbox and Forming Hydrodynamics	Cyrus Aidun
2:55 p.m. - 3:10 p.m.	Break		
3:10 p.m. - 3:40 p.m.	Project F003	Fundamentals of Coating Systems	Cyrus Aidun
3:40 p.m. - 4:10 p.m.	Project F002	Fundamentals of Web Heating	Tim Patterson
4:10 p.m. - 5:10 p.m.	Project F001	Status of Impulse Drying Commercialization	David Orloff
5:10 p.m. - 6:00 p.m.	Sub Committee Discussions of Projects		

PAPERMAKING
PROJECT ADVISORY COMMITTEE MEETING

March 24, 1998

Institute of Paper Science and Technology
Atlanta, Georgia

COMMITTEE DISCUSSIONS AGENDA

Room 177

1:00 p.m. - 1:10 p.m.	Convene - Antitrust Statement - Confidentiality Statement - New Members - Acceptance of Fall, 1997 minutes - Review of agenda	White
1:10 p.m. - 1:40 p.m.	RAC Report Research Roadmap	John Bergin David White, David Orloff
1:40 p.m. - 2:00 p.m.	Project F022 Flow Through Porous Media presentation	Seppo Karrila
2:00 p.m. - 2:20 p.m.	Project F021 Drying presentation	Fred Ahrens
2:20 p.m. - 2:50 p.m.	Approach Flow Systems (F004-Wang)	**Johnson,** Westling, Marziale, Thiessen
2:50 p.m. - 3:00 p.m.	Break	
3:00 p.m. - 3:30 p.m.	Headbox and Forming Hydrodynamics (F005- Aidun)	**Shands**, Anderson, Burns, Devlin, Panek
3:30 p.m. - 4:00 p.m.	Fundamentals of Coating Systems (F003-Aidun)	**Simmons**, Proxmire, Bergin
4:00 p.m. - 4:30 p.m.	Web Heating and Pressing of Heated Webs (F002-Patterson)	**Cunnane**, MacDowell, Lacz
4:30 p.m. - 5:00 p.m.	Impulse Drying (F001- Orloff)	**Kramer**, Rogers, Haskins
5:00 p.m. - 5:30 p.m.	Pressing, Drying (F021, F022)	**Chaudhuri**, Palumbo, Nisita, White, Reese

TABLE OF CONTENTS

FUNDAMENTALS OF COATING SYSTEMS

STATUS REPORT

FOR

PROJECT F003

Cyrus K. Aidun

March 23-24, 1998

Institute of Paper Science and Technology
500 10th Street, N.W.
Atlanta, Georgia 30318

DUES-FUNDED PROJECT SUMMARY

Project Title:	Fundamentals of Coating Hydrodynamics
Project Code:	COAT
Project Number:	F003
PAC:	Engineering
Project Staff	
Faculty/Senior Staff:	C. Aidun
Staff:	H. Huang
FY 98-99 Budget:	$47,000
Allocated as Matching Funds:	
Time Allocation	
Faculty/Senior Staff:	10%
Support:	100%
Supporting Research	
M.S. Students:	K. Yanagisawa
Ph.D. Students:	C. Chen, C. Cody
External:	

RESEARCH LINE/ROADMAP: Paper Machine Productivity

To enhance coating quality and productivity by reducing coating defects and increasing coating speed.

PROJECT OBJECTIVE:

Objectives of this project are to

1. investigate the cause and origin of coat weight nonuniformities reported in high-speed blade coating of paper and board,

2. explore novel coating systems for application of a more uniform coat weight profile at higher machine speeds,

3. develop methods for analysis of suspension dynamics and rheology of coating suspensions under high-shear regions in blade coating processes

PROJECT BACKGROUND:

SCOPE

The focus of the project during the 1996-97 has been to:

1. evaluation of the computational method for analysis of suspensions in coating systems and interaction of the coating with the substrate;
2. preparation for pilot trials of the second version of the vortex-free coater; and
3. experimental trials of the vortex-free coater at IPST.

SUMMARY OF RESULTS:

The air-jet version of the vortex free coater, as shown in Fig. 1, has been installed on the developmental coater at Beloit R&D. The purpose of this phase of the project has been to make a quick evaluation of the concept, and to decide whether the effect is significant enough for implementation on the pilot coater. The trials with the developmental coater have been completed. The appearance of the coated film on the backing roll provides qualitative information about the performance of the coating head.

The results, although qualitative, show positive effects of the air jet on the coating film applied to the backing roll. High speed images of the film with and without the air jet show a marked difference in some cases. These results will be presented at the project review meeting.

The net effect of the air jet seems to be in producing a more uniform coated film at lower coating jet flow rates and velocity. Based on these results, one can expect an increase in the maximum coating speed with a fixed flow rate. Also, it appears that the air jet will allow application of the coatings with higher solids ration. Both of these effects point toward higher coating speed, less drying requirement, and consequently, increased productivity.

The focus at IPST is on computational analysis of the liquid-air jet coating system to provide information for design of the coating head for pilot trials. There are two basic difficulties with the computational analysis of this system. The first is the deformation of the free surface and the interfacial boundary between liquid and air. The convergence of this problem depends greatly on how well the interfacial conditions can be satisfied. The second difficulty is the significant difference between the density of air and liquid. This difference in fluid properties makes numerical scaling problems and convergence difficulties. A stepwise continuation of the relevant parameters is used to trace the solution from a linear Stokes flow to the flow parameters realized in the actual high-speed coating operation.

The computational are done with a standard code based on Galerkin finite element method (Fidap). The current coating geometry and the computational domain are outlined in Figures 1a and 1b, respectively. The computational case is the exact duplicate of the system currently operational on Beloit's developmental coater where the coating liquid is applied on a backing roll.

The problem definition is provided in Table 1. The computational mesh structure with 540 elements in the liquid region and 820 elements in the air region is shown in Fig. 2.

Table 1. Physical properties of fluids and initial and boundary conditions

Physical properties	The density of liquid (ρ_{liq})	1500 kg.m^{-3}
	The density of air(ρ_{air})	1.1614 kg.m^{-3}
	The dynamic viscosity of liquid (μ_{liq})	1.0 Pa.s
	The dynamic viscosity of air (μ_{air})	1.846.10^{-5} Pa.s
	Surface tension (γ)	0.0478 N.m^{-1}
Boundary conditions	Roll speed (U_{web})	20 m.s^{-1}
	Inlet liquid velocity (non-dimensionalized)	$u(x)=c1-c2\,x^2$ $\overline{U} = \frac{1}{2h}\int_{-h}^{h} u(x)dx$ where h=0.029 c1=1.36 c2=1582.52 $\overline{U}$ =0.91
	The velocity of walls (including the top, V-shape, and the first part of the bottom surface along the inlet liquid flow)	No Slip.
	The roll speed (non-dimensionalized)	U_t =1.0 ; U_n =0.0 (Dirichlet)
	The outlets of air and liquid	σ_t = 0.0 ; σ_n = 0.0 (Neumann)
Initial condition		
	Velocity field	Stokes Flow
	The contact angles at the free surface	right = 0.0, left=127
	The contact angles at the air-liquid interface.	Right = 151.5

The equations governing the flow in the coater are the mass and momentum conservation equations with a Newtonian constitutive model for both liquid and air. There is continuity in velocity, normal and tangential forces at the interface.

The shear rate in the jet flow is not as large as the shear rate in blade coating, therefore, for now a Newtonian fluid is considered. The equations are non-dimensionalized by using the velocity of the web, the width of the inlet liquid channel and the density of liquid as the velocity, length and density scales, respectively. The values for these scales are shown in Table 2.

Table 2. Characteristic scales

Characteristic Velocity	Roll velocity	20 $m.s^{-1}$
Characteristic Length	Width of the inlet liquid channel	0.00149 m
Density	liquid density	1500 $kg.m^{-3}$

Solution Procedure and Preliminary Results

The governing equations, constitutive relation, and boundary conditions completely define the given problem. These equations are solved using a Galerkin finite element approach with 4-node, isoparametric, quadrilateral elements. The velocity is approximated over the element using bilinear basis functions and the pressure is based on the discontinuous basis function. The free surface boundary is determined by satisfying the steady-state kinematics and dynamic conditions in a fully coupled manner. The nonlinearity of the governing equations require an iterative approach to converge to the actual solution.

The solution procedure, based on a parametric continuation approach, is as follows:

Step 1: obtain a complete flow flied solution with free-slip condition at the free surfaces and uniform fluid properties using Newton-Raphson iteration procedure;

step 2: restart the solver from solution obtained in from step 1 as an initial condition, release one free surface from the free-slip condition and solve the complete solution using segregated iterative method;

step 3, restart the solution from step 2, release another free surface and solve by using segregated iterative method;

step 4, restart the solution from step 3, change the density and viscosity ratios of both fluids gradually in a stepwise manner until target properties are reached. Parameter continuation methods are used to assist in the variation of parameters to reach the desired solution for given boundary conditions. Typically, convergence is achieved when the norm of the difference in solution from one iterative step to the next is less than 10^{-3} and that of free surfaces is less than 10^{-2}.

Figure 3 shows the velocity field of air and liquid with the average inlet velocity of air at 0.5 and that of liquid at 0.91. Flow separations in the air boundary layer occurs at the upper right turning corner. The coating liquid gradually expands when first in contact with air because of the low air pressure in the separated region. Two small vortices develop in the air layer, as seen in streamlines presented in Figure 4. The dynamic contact line is pinned, and thus, the adjacent elements distort due to upward momentum force. The severe distortion of the elements near the singular contact point is a problem under investigation (compared to Figures 2 and 5).

In general, to solve a problem with irregular geometry which generates a sharp interface curvature with significant impact on interface stability; free surface flows with interfacial motion

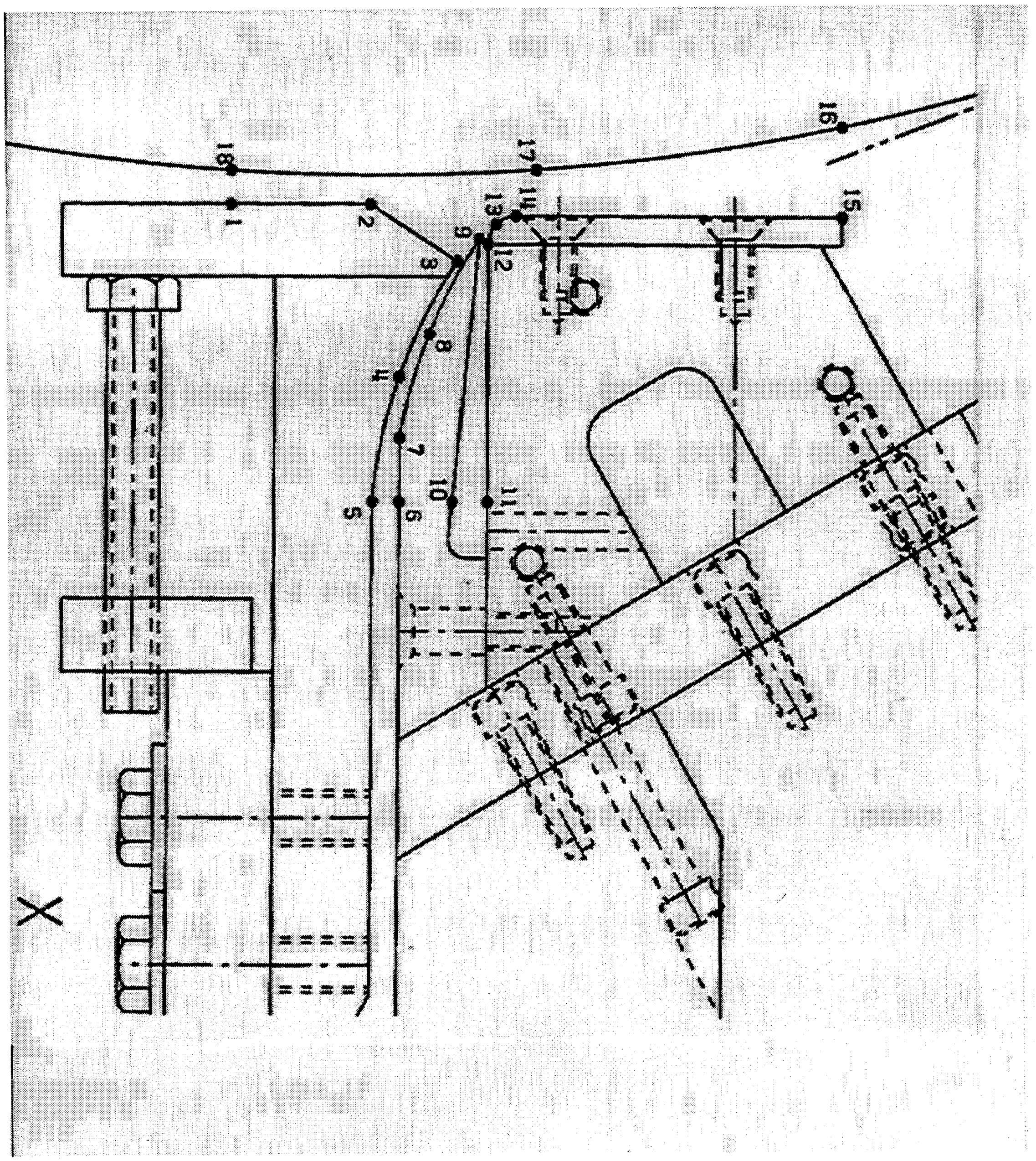

Figure 1a. The drawing of the coater head with the air jet channel (10, 11, 12, and 9) on the development coater.

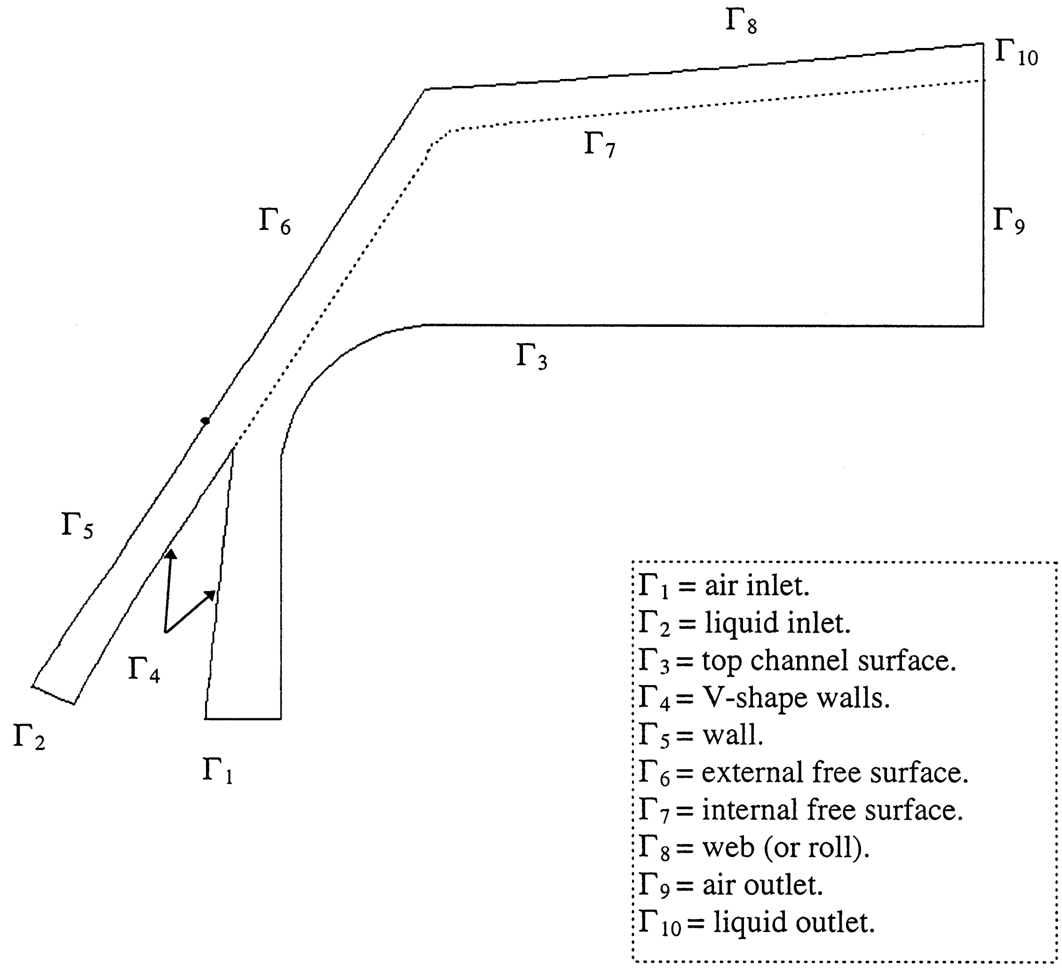

Figure 1-b. Outline of geometry and boundary of the computational domain

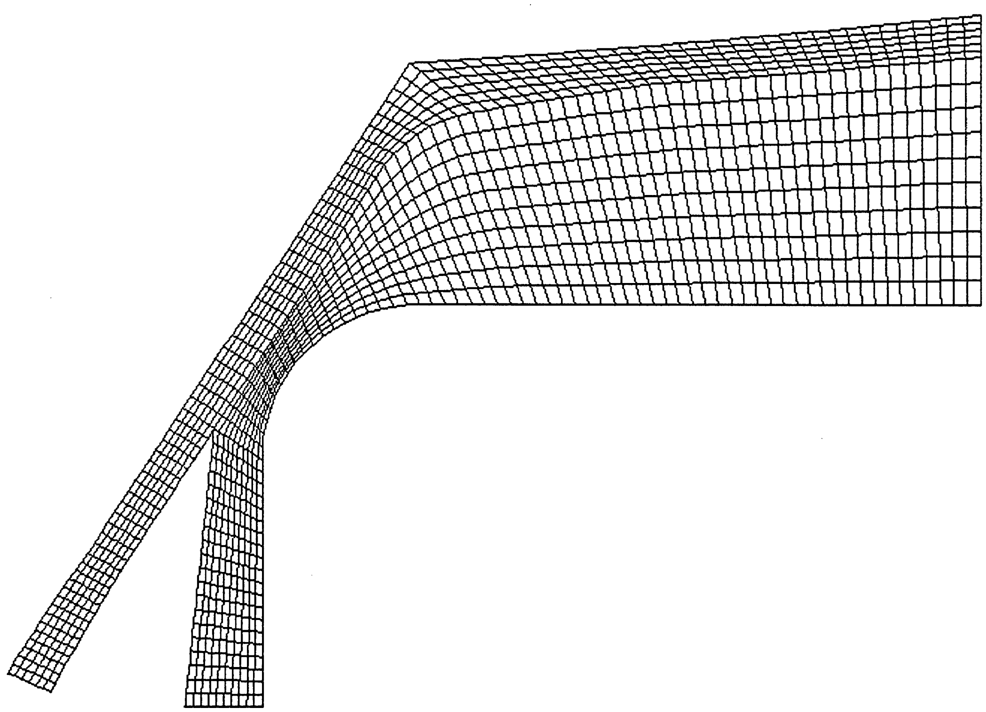

Figure 2. Initial computational grid structure for the coating liquid and air jets.

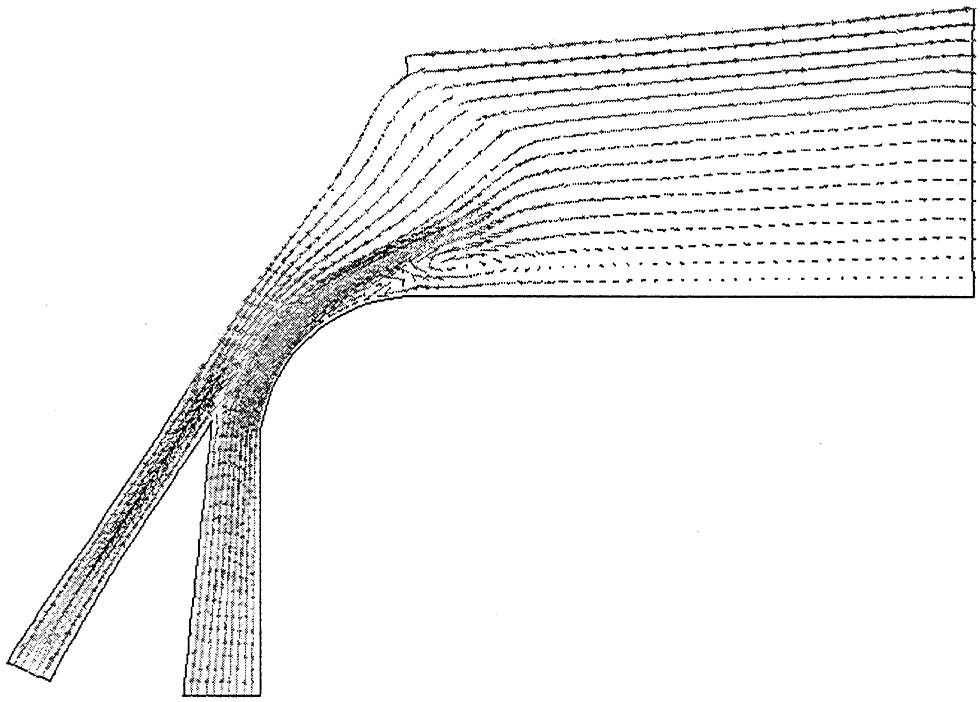

Figure 3. Velocity vector plot of the air and liquid coating jet.

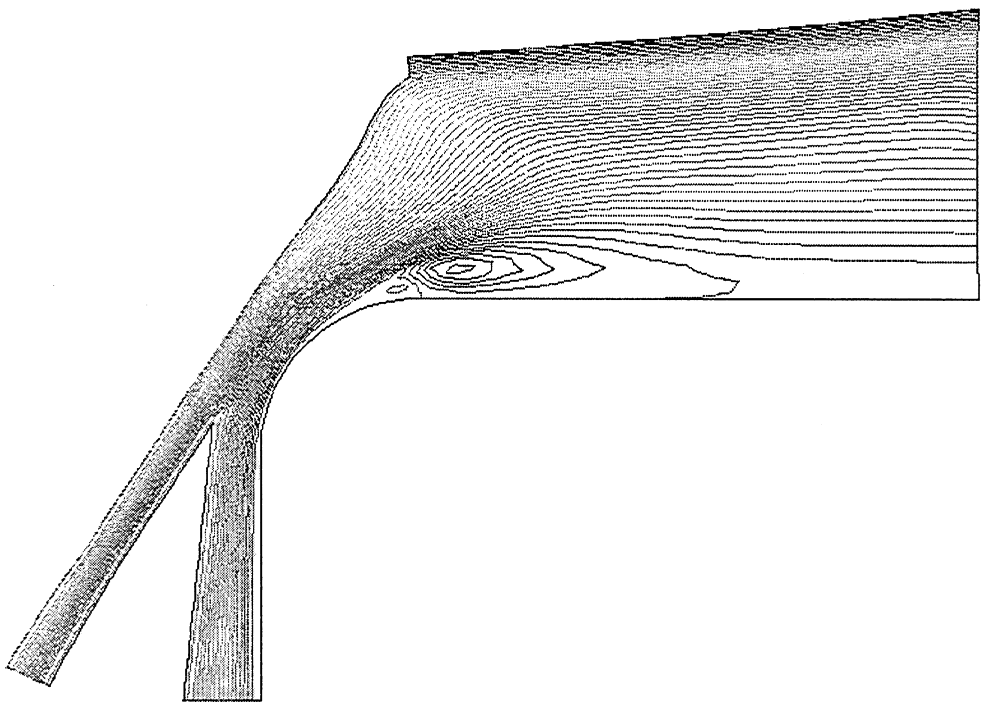

Figure 4. Stream lines of the air and liquid coating jet.

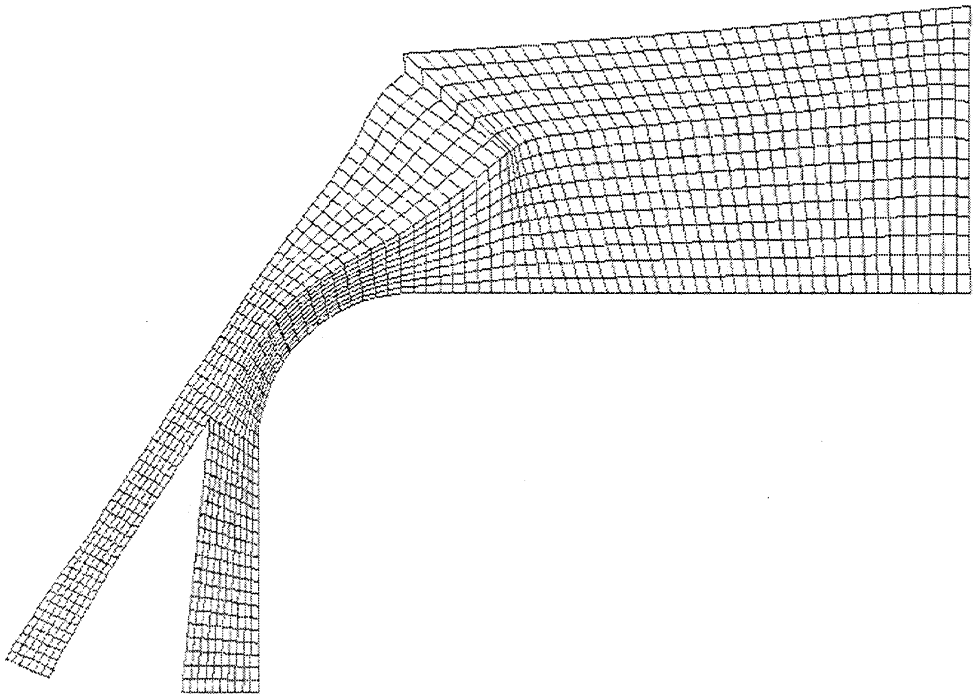

Figure 5. Converged solution showing the deformation of the free surface and the air-liquid interface. (note the irregular grid deformation due to numerical problems near the pinned contact point.)

introduces numerical instability and tracking problems. Moving boundary problems with dynamic contact line generate singular regions with high stress values reducing the radius and rate of convergence. Some references on computational analysis of free surface problems and difficulties with dynamic contact lines are provided below. The addition of a second phase, that is the air jet layer, makes our problem somewhat more difficult that the problems considered in the referenced studies.

The current results show that the design of the development version of the coater is not optimized. The region with maximum pressure on the liquid surface is considerably away from the contact line. The next design will optimize the air jet location and angle to most effectively prevent jet deflection and air entrainment from the upstream side of the jet.

References

K.N. Christodoulou and L. E. Scriven, "Discretization of free surface flows and other moving boundary problems," *J. Comp. Phys.* 99, **39** (1992).

P.R. Schunk and L.E. Scriven, "Constitutive equation for modeling mixed extension and shear in polymer solution processing," *J. Rheology* **34**, 1085 (1990).

P.R. Schunk, J. M. de Santos and L. E. Scriven, "Flow of Newtonian liquids in opposed-nozzles configuration," *J. Rheology* **34**, 387 (1990).

P. Bach and O. Hassager, "An algorithm for the use of the Lagrangian specification in Newtonian fluid mechanics and applications to free-surface flow", *J. Fluid Mech.* **152**, 173-190, (1985).

C. Huh, and S. G. Mason, "The steady movement of a liquid meniscus in a capillary tube." *J. Fluid Mech.* **81**, 401 (1977).

L. M. Hocking "Sliding and spreading of thin two-dimensional drops." *Q. J. Mech. Appl. Maths* **34**, 37.

Nomenclature

δ_{ij}	Kronecker delta
ε_{ij}	rate of strain tensor
γ	surface tension
Γ_i	boundary
μ	dynamic viscosity
ρ	density
ρ_{ref}	reference(characteristic) density
σ_{ij}	stress tensor
σ_n	normal component of the traction vector
σ_t	tangential component of the traction vector
τ_{ij}	deviatoric stress tensor
c1, c2	coefficients

Ca	Capillary Number
f_i	component of gravitational acceleration
h	the half of the distance of inlet liquid channel
H	Gaussian mean curvature of the free surface
L_{ref}	reference(characteristic) length
n	unit normal vector
P_a	ambient pressure
s	arc length
S	interface function
t	time; unit tangent vector
$u(x)$	the velocity profile
U_t	the tangential velocity
U_n	the normal velocity
$\overline{U}$	the average velocity
U_{ref}	reference(characteristic) velocity
$\vec{V}$	fluid velocity vector
x	local coordinate

GOALS FOR FY 98-99:

- Demonstration of the commercial viability of the vortex-free coater
- Commercial implementation of the vortex-free coater

DELIVERABLES FY 98-99:

1. Results from computational analysis and optimization of the vortex-free coater
2. Demonstration of the superior performance of a new coating system through pilot trials at Beloit R&D

SCHEDULE:

The computational procedure for design optimization of the new vortex-free coater is under development. Various geometries will be analyzed for optimization of the system. This work will be in parallel to the design, fabrication and pilot trials at Beloit's R&D. The pilot coater head will be designed to provide considerable flexibility to vary the geometry and observe the effects on the coating uniformity at various air and liquid flow rates. We assume that two series of pilot trials would be required. The second design will incorporate the experience and information from the first series of pilot trials.

```
Item        Time ==>        April          July          Oct.          Jan.          April

1. Computational Optimization------------------------------------------------------------------------------|
2. Pilot Trial Demonstration
     Design & Fabrication     -------------|               ------------------------------|
     Pilot Trials                          ------------------|                            -------------------|
3. Annual Report                                                                               -----------------|
```

APPROACH FLOW SYSTEMS

STATUS REPORT

FOR

PROJECT F004

Xiaodong Wang (PI)
Frederick Bloom
Zhigang Feng

March 23-24, 1998

Institute of Paper Science and Technology
500 10th Street, N.W.
Atlanta, Georgia 30318

DUES-FUNDED PROJECT SUMMARY

Project Title:	APPROACH FLOW SYSTEMS
Project Code:	FORMING
Project Number:	F004
PAC:	Papermaking
Division:	Engineering
Project Staff	
Faculty/Senior Staff:	X. Wang
Staff:	F. Bloom, Z. Feng
FY 97-98 Budget:	$90,548.00
Allocated as Matching Funds:	$0
Time Allocation	
Faculty/Senior Staff:	0.3 man-yrs
Support:	0.5 man-yrs
Supporting Research	
M.S. Students:	None
Ph.D. Students:	None
External:	None

Research Line/Roadmap: Improve the ratio of product performance to cost for pulp and paper products 25% by developing break-through papermaking and coating processes which can produce the innovative webs with greater uniformity than that achieved by current processes.

Project Objective: To resolve problems relating to approach flow systems such as stock mixing before the fan pump and to obtain deeper fundamental understanding that can be used in future designs. Based on computational simulation, experimental data, and mill operation data, we hope to clearly define the means to achieve uniform and smooth stock delivery to the headbox and to develop specific approach system design recommendations.

Project Background: The approach flow system is composed of numerous individual components between the stock preparation section and the headbox, which include fan pumps, piping, deaeration system, attenuator, pressure screens, cleaners, control valves and white water recycling systems. The effects of each component in the approach pipe system will directly influence the performance of paper machines.

As the development of more high production rate forming devices and short distance forming units such as hydraulic headboxes and twin-wire forming, the pressure pulsation tolerance and consistency fluctuation within the stock (mixture of wood fibers, chemical additives, and water) are getting more strict. In fact, the good performance of stock approach pipe systems is essential to the smooth operation of the entire paper machines with higher and higher machine speeds.

From a design standpoint, the stock approach system is one of the most critical areas of the paper machine and is often called "plumbers' nightmare." The current design guidelines are normally used to avoid the following difficulties:

- non-uniform fiber delivery;
- unstable flow, pulsations and surges;
- stagnant zones, trapped air, rough surfaces; and
- vibration.

Although the arrangement, design, and operation of stock approach equipment will vary greatly from mill to mill and machine to machine, and the available guidelines and research information are often found to be inadequate and even confusing, there is no tool available to analyse the approach flow system as a whole under the circumstance of component changes, consistency and stock variations. Therefore, to provide engineers the general design guidelines, more feasible analysis tools for both the specific components within approach flow systems and the whole system design are imperative.

This project (F004) is based on the proposal "On the Research Area of Approach Pipe Systems" (March, 1996 PAC Report Page 277-334). It is the intention of this project to identify the fundamental research areas of approach pipe systems and to provide the state-of-art solution techniques. The research results and procedures shall be widely applicable to both paper machine suppliers and mills.

In order to establish a robust and worthwhile project in this area, the needs and interests of the IPST membership companies were investigated, and based on the available published research results, the following main research areas are identified:

- *flow-induced vibration*, including pressure pulsation and dynamic analysis of approach pipe systems; and
- *fluid flow control*, including chemical additive (such as retention aids) mixing, uniform consistency, stock and white water mixing.

In the Status Report 97 (March, 1997 PAC Report Page 27-56), a preliminary study on the consistency fluctuations within different stages of the stock preparation process and their correlation to the MD basis weight variation was presented. A specific software "Papermaking Signal Analysis Package" was developed at IPST, and we are planning to perform a demo during this PAC presentation.

Based on the suggestions from PAC members, we focused our research attention on the silo mixing units. We realize that proper designs of such silo mixing units depends on both the mixing efficiency and the mechanical integrity involving stability and dynamical behaviors.

In particular, according to the previous research plan, we have accomplished the following tasks:

- Task 1: Summarize the available relevant literature on pipe mixing issues; (Done)
- Task 2: Formulate the mass and momentum balances of the fiber stock before the fan pump; (Done)
- Task 3: Perform a 2D transverse mixing computational simulation; (Done)
- Task 4: Design a feasible experimental apparatus for pipe flow mixing measurements; (Done)
- Task 5: Compare 2D simulation results with analytical solutions to verify the simulation procedures (turbulent flow with mass transfer); (Done)
- Task 6: Perform a literature search on pressure pulsation induced by flow within and around the pipe; (Done)
- Task 7: Formulate a model for the fluid oscillation behavior of a single pipe conveying fluid; (Done)
- Task 8: Formulate a model for the fluid oscillation behavior of two concentric pipes conveying fluids; (Done)
- Task 9: Determine the protruded pipe oscillation frequency induced by flow within and around the pipe; (Done)
- Task 10: Perform a 3D transverse mixing computational simulation; (Done)
- Task 11: Compare 3D simulation results with available experimental results in chemical engineering areas. (Done)

Summary of Results: For the past two years (1996, 1997), we have reviewed most of the papers on pipe mixing issues. We realize that, while prompt mixing is necessary in chemical reactions, in the paper industry, for a fixed setting of the coaxial mixer and fan pump, the efficient and stable mixing within a broad range of operation conditions is more desirable. A summary of the research results on the jet trajectory including a brief literature survey and the formulation of mass and momentum balances before the fan pump is presented in the paper "Single Jet Mixing at Arbitrary Angle in Turbulent Tube Flow" (ASME FEDSM-98).

We also finish the design of the experiment setup. The experimental apparatus consists of one holding tank and one water supply line which are attached to two concentric tubes as illustrated in Fig. 1. The tank in Fig. 1 contains the tracer and is attached to the coaxial jet. The jet nozzle will be located at a distance of four pipe diameters from the turning elbows where the flow is considered straight. The tank volumes, pipe and nozzle diameters along with proper flow control provide fully developed turbulent flow from the nozzle for a period of several minutes with a nozzle Reynolds number $Re > 10^4$. Measurements of concentration standard deviation will

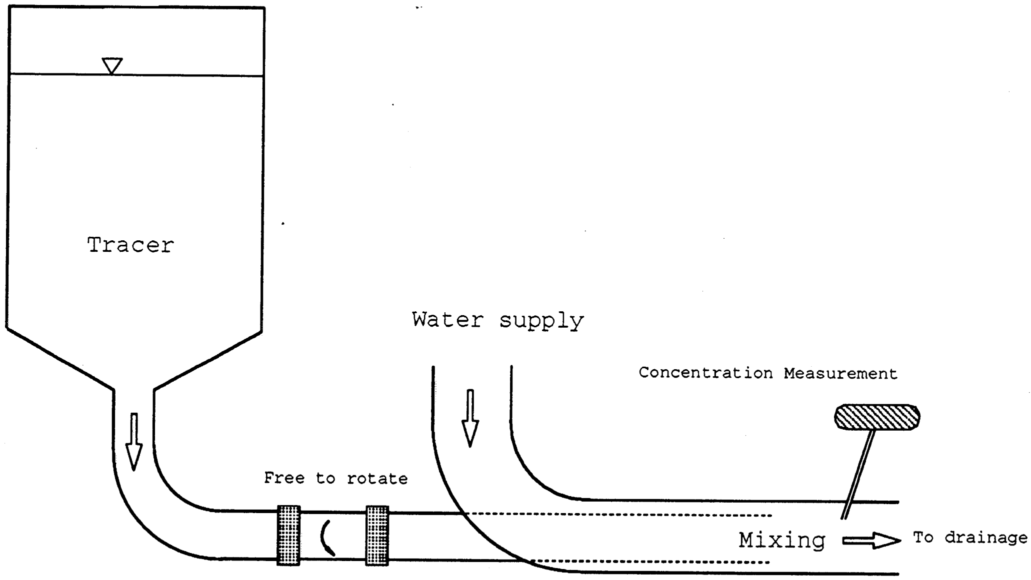

Figure 1: Experiment setup.

be obtained across the mixing pipe at several axial locations downstream from the nozzle. In particular, a Perkin Elmer fiberoptic immersion probe (Lamba 10) which is sensitive to the optical density of the tracer (e.g., uranine dye) and has a small sensing volume of diameter ~ 1 mm for proper spatial resolution will be used.

In the paper "Flow Induced Oscillations of Submerged and Inclined Concentric Pipes with Different Lengths", we present a general survey in the area of flow-induced pipe vibrations and formulate a mathematical model to study the dynamics and stability of submerged and inclined concentric pipes having different lengths. The governing equations for the inner tubular beam are derived under small deformation assumptions and with the consideration of gravitational forces, the turbulent boundary layer thickness of the external flow, fluid frictional forces, and inertial effects. We obtain the discretized dynamical equations using spatial finite difference schemes and calculate the frequency range of a particular pipe system design. In addition, by varying the operating conditions, we are able to identify a few critical parameters pertaining to the proper design of such pipe systems. For a specific silo pipe system design, we find that the first three natural frequencies of the inner tubular pipe are very small and should be eliminated if possible in the silo pipe system design. In addition, by varying different design parameters, we conclude:
(1) By decreasing the inner or outer pipe lengths, we can increase the natural frequencies; however, changing the inner pipe length is more effective.
(2) The inclination angle, the depth of the submerged pipe system, and gravity are not important design parameters as far as the pipe stability concerned.
(3) For a piping system with fixed volume flow rates, there exists an optimal inner

pipe radius.
(4) In general the larger the outer pipe radius, the more stable the suspended pipe system will be. Nevertheless, as the outer pipe radius increases, the inner pipe vibration model approaches that of the case of a singular flexible pipe immersed in an unconfined fluid.

In the paper "Computational Simulation of Turbulent Mixing with Mass Transfer", we present a series of computational simulations of three-dimensional turbulent mixing with mass transfer for various pipe mixing arrangements. The simulations are carried out with the ADINA software, in which general-purpose finite element and finite volume formulations along with the k-ϵ turbulent model are used for incompressible Navier-Stokes flows with mass transfer. Based on the predicted pressure and velocity profiles and the standard deviation of tracer (or fiber) spatial distributions at certain distances downstream from the injection point, we compare the mixing performances of various transverse, concentric, and multijet mixers as well as four silo mixing units. In addition, we deduce certain design information pertaining to different mixing configurations.

Goals for FY98-99: The objective of FY98 is to improve the silo water pipe mixing units and to suggest certain modifications such as the fan pump location, the velocity and diameter ratios of the associated concentric and transverse pipe mixers. We have already demonstrated the computation capabilities we have at IPST to simulate fluid-fluid turbulent mixing with mass transfer during our fall PAC meeting. For the period from October 1997 to March 1998, a realistic research plan for project F004 is summarized as:

- 1. Write-up the mathematical models and assumptions we made in our computer simulations which include the transverse jet mixing, concentric jet mixing, multi-jet mixing, and full-fledged silo mixing. This task will in fact, to my best judgment, take a large portion of the remaining time before the March PAC meeting. Notice that the PAC reports are due to PAC members in early February. **target date Mar., 1998**

- 2. In the turbulent computational model we employ, we have constants such as mass diffusivities, turbulent mass diffusivities, and constants for $k-\epsilon$ model to adjust based on experimental measurements. In addition, we assume the model of liquid-liquid mixing, instead of multi-phase flow. Before we proceed with massive computations to check various flow ratios, geometries, and other operation conditions, we need especially in our case, i.e., turbulent mixing with fiber stock flow, to calibrate the constants we used in our simulation. In addition, it would be prudent to compare our simulation results with FLUENT, another important CFD code. We have already started to prepare for the simulations leading to a better guideline in approach flow systems, nevertheless, the final computation efforts will be made after we obtain or confirm those constants. Since this task involves experimental design and setup, we do not have an affirmative completion date at this moment, however, we estimate that the whole experimental setup can be ready for debugging in February, and we might have a first set of data to show in March PAC meeting 1998. Notice that we do not have time to include the experimental results in this March's PAC report, but the experimental design will be included. We need to emphasize that the experimental measurements will take two different stages. First, we need to measure the turbulent mixing of inert tracer; second, we need to measure the turbulent mixing of fiber stock. **target date Dec., 1998**

- 3. Once we have validated our simulation model with experimental results (for fiber stock mixing), and other CFD code solutions (for one or two typical cases only), we will input various operation conditions, and come up with new guidelines for the silo pipe mixing units within approach flow systems. The crucial step is to confirm to our best knowledge that the model we have is as close to reality as we can get, prior to investing large amounts of time into generating a multitude of numerical simulations. **target date Mar., 1999**

- 4. After we achieve the goals set in item 1 through 3, we can then implement certain recommendations in the previously identified mill and validate the research findings in actual mill operations.

- 5. After we complete the research relating to the silo unit, we can then move on to the other key components of stock approach flow systems, such as the pressure pulsation attenuator and the surge tank.

Deliverables: The final deliverables for FY98 can be summarized into the following tasks:

- 1. Run specific test cases (using estimated constants) to demonstrate trends predicted by the transverse mixer simulation model;

- 2. Run specific test cases (using estimated constants) to demonstrate trends predicted by the concentric mixer simulation model;

- 3. Run specific test cases (using estimated constants) to demonstrate trends predicted by the multi-jet mixer simulation model;

- 4. Run specific test cases (using estimated constants) to demonstrate trends predicted by the full-fledged silo simulation model;

- 5. Write up models and sample trend results for: transverse jet mixing, concentric jet mixing, multi-jet mixing , full-fledged silo mixing;

- 6. Work with both the paper companies and the paper machine suppliers in order to identify one mill to implement some of the future recommendations on the silo mixing unit;

- 7. Prepare Spring PAC report;
- 8. Construct experimental flow loop, debug apparatus and test methods;
- 9. Develop techniques and measure; mass diffusivity, turbulent mass diffusivities, and constants for $k - \epsilon$ model for liquid-liquid mixing and validate CFD model;
- 10. Input measured liquid-liquid constants and various operating conditions into CFD model to develop a preliminary guideline for silo mixing areas;
- 11. Prepare Fall PAC presentation;
- 12. Develop experimental techniques to measure constants for fiber stock-liquid mixing (to be used in liquid-liquid simulation model);
- 13. Measure mass diffusivity, turbulent mass diffusivities, and constants for $k - \epsilon$ model for fiber stock-liquid mixing and validate CFD model;
- 14. Input measured fiber stock-liquid constants and various operating conditions into CFD model to validate and improve the silo mixing guideline;
- 15. Prepare Spring PAC report.
- 16. Start to implement some of the research findings in the previously identified mill.

Schedule(Attach Timeline):

Discussion(Attach Three Reports):

Task	Month																
	Nov. (97)	Dec. (97)	Jan. (98)	Feb. (98)	Mar. (98)	Apr. (98)	May (98)	Jun. (98)	Jul. (98)	Aug. (98)	Sept. (98)	Oct. (98)	Nov. (98)	Dec. (98)	Jan. (99)	Feb. (99)	Mar. (99)
1	0–	–x															
2	0–	–x															
3	0–	–x															
4	0–	–x															
5	0–	–x															
6		0—	—	–x													
7			0–	–x													
8		0–	—	–x													
9				0–	—	—	–x										
10							0–	—	—	–x							
11										0–	–x						
12								0–	—	—	—	–x					
13													0–	–x			
14														0–	—	–x	
15																0–	–x
16																	0–

Table 1: Timetable for approach flow systems project (F004).

Computational Simulation of Turbulent Mixing with Mass Transfer

by

Xiaodong Wang, Zhigang Feng, Larry J. Forney

1 Introduction

Turbulent mixing of various fluid streams has many industrial applications in areas such as sewer discharge, chemical reactions, heat transfer operations, and mixing and combustion processes [5] [12]. In the paper industry, fiber water mixture needs to be diluted and delivered smoothly and uniformly to the headbox forming section. One of the key components is the so-called silo mixing unit depicted in Fig. 1, which consists of various pipe mixing arrangements. In this work, we consider the following mathematical models related, but not limited to current silo designs: (i) transverse mixers at different injection angles; (ii) concentric mixers with different nozzle shapes; and (iii) multijet mixers. Full-fledged simulations for four silo mixing units with complex three-dimensional geometries are also investigated. Considering the fact that the rheology of low consistency fiber water mixture is very similar to that of water, we employ the mixing model of two turbulent miscible fluids with the same density and viscosity, however, different inert tracer concentrations.

In the general area of turbulent mixing, many research efforts have been directed to experimental investigations. More recently, some numerical studies have been performed on two- or three-dimensional turbulent mixing with mass or heat transfer for simple geometries [10]. However, very few studies are available in dealing with complex three-dimensional turbulent simulation with mass transfer. Some of the recent advances in applying CFD techniques to the chemical process industry are documented in Ref. [11]. In this paper, we present a systematic study on various fundamental pipe mixers and silo mixing units using the ADINA software, which consists of the program on heat transfer in solids ADINA-T, the program on displacements and stresses ADINA, the program on fluid flows and heat transfer ADINA-F, the pre-processor ADINA-IN, and the post-processor ADINA-PLOT. A detailed description of the recent development of the ADINA-F program is available in Ref. [1].

In the following section, we will summarize the governing equations and the criteria taken in measuring mixing uniformity. We discuss in Section 3 the transverse jet mixers with different angles. In Section 4, we focus on the concentric mixers with various nozzle shapes. The relatively new multijet mixing arrangements will be considered in Section 5, and the full-fledged silo mixing unit simulations will be presented in Section 6. Design information deduced from the computational simulation results is presented in Sections 3 to 6 as well as in the concluding section.

2 Research Approaches

We consider here the turbulent flow of a homogeneous, viscous, incompressible fluid with constant properties. By representing the fluctuating parts in the eddy viscosity ν_t, turbulent kinetic energy k, and turbulent dissipation rate ϵ, we obtain the following governing equations from the mass and momentum conservation equations [7] [14]:

$$\begin{aligned} \frac{\partial v_i}{\partial x_i} &= 0 \\ \frac{\partial v_i}{\partial t} + v_j \frac{\partial v_i}{\partial x_j} &= \frac{1}{\rho}\frac{\partial p}{\partial x_i} + \frac{\partial}{\partial x_j}((\nu + \nu_t)\frac{\partial v_i}{\partial x_j}) \end{aligned} \qquad (1)$$

where ρ, ν, ν_t, v_i, and p stand for fluid mass density, kinematic viscosity, eddy viscosity, time-average fluid flow velocity in direction x_i, and time-average pressure, respectively. Furthermore, for the standard k-ϵ turbulent model, we have two additional equations:

$$\begin{aligned} \frac{\partial k}{\partial t} + v_j \frac{\partial k}{\partial x_j} &= \frac{\partial}{\partial x_j}((\nu + \frac{\nu_t}{\sigma_k})\frac{\partial k}{\partial x_j}) + \nu_t \Phi - \frac{k}{T} \\ \frac{\partial \epsilon}{\partial t} + v_j \frac{\partial \epsilon}{\partial x_j} &= \frac{\partial}{\partial x_j}((\nu + \frac{\nu_t}{\sigma_\epsilon})\frac{\partial \epsilon}{\partial x_j}) + c_1 \frac{1}{T}\nu_t \Phi - c_2 \frac{\epsilon}{T} \end{aligned} \tag{2}$$

where c_1, c_2, σ_k, and σ_ϵ are designated constants; Φ denotes the inner product of the velocity strain tensor $2e_{ij}e_{ij}$ with $e_{ij} = (\frac{\partial v_i}{\partial x_j} + \frac{\partial v_j}{\partial x_i})/2$; and the turbulent time scale T and viscosity ν_t are expressed as:

$$T = \frac{k}{\epsilon} + \sqrt{\frac{\nu}{\epsilon}} \tag{3}$$

$$\nu_t = c_\mu k T \tag{4}$$

with a constant c_μ.

In addition to the mass and momentum conservation equations with the k-ϵ turbulent model, we employ the following tracer conservation equation to model the mass transfer phenomena in the turbulent flow,

$$\frac{\partial c}{\partial t} + v_j \frac{\partial c}{\partial x_j} = \frac{\partial}{\partial x_j}((\nu/Sc + \nu_t/\sigma_c)\frac{\partial c}{\partial x_j}) \tag{5}$$

where c, Sc, and σ_c are the time-average concentration of tracer (or fiber), Schmidt number, and a selected constant. We note that a similar equation can be directly obtained for the temperature distribution in the case of heat transfer.

The governing equations (1), (2), and (5) are implemented in the ADINA-F program. Moreover, the turbulent diffusivity $\nu/Sc + \nu_t/\sigma_c$ as a function of spatial locations is incorporated in the user-supplied subroutine provided by the ADINA software. In this work, we select $c_1 = 1.44$, $c_2 = 1.92$, $\sigma_k = 1.0$, $\sigma_\epsilon = 1.3$, $c_\mu = 0.09$, $Sc = 1.64 \times 10^6$, and $\sigma_c = 0.9$.

The mixing uniformity is measured in terms of two relative standard deviations σ_c and σ_{cu} of concentration c about the arithmetic mean $\bar{c}$ at a given pipe cross section downstream from the nozzle, defined as follows,

$$\bar{c} = \int_A c dA \Big/ \int_A dA \quad (6)$$

$$\sigma_c^2 = \int_A (\frac{c-\bar{c}}{\bar{c}})^2 dA \Big/ \int_A dA \quad (7)$$

$$\sigma_{cu}^2 = \int_A (\frac{c-\bar{c}}{\bar{c}})^2 u dA \Big/ \int_A u dA \quad (8)$$

We recognize that the integrals $\int_A udA$ and $\int_A cudA$ relate directly to the volume flow rates and tracer concentration through mass balances. Denoting q and Q as the flow rates of the streams with tracer concentrations c_1 and c_2, respectively, from the mass conservation laws, we obtain

$$\int_A udA = q + Q \quad (9)$$

$$\int_A cudA = c_1 q + c_2 Q \quad (10)$$

which will be used to validate the computational results.

3 Mixers

3.1 Transverse Mixers

The most widely used pipe mixer is the transverse mixer shown in Fig. 2, in which a jet with diameter d_1 issues fluid containing tracer into a tube of diameter d_2. The ambient fluid velocity of the tube is v_2, and the initial tracer jet velocity is v_1.

We compare, in this work, the transverse mixers with the following physical parameters: $d_1 = 0.1092$ m; $d_2 = 0.3048$ m; $v_1 = 3.0$ m/s; $v_2 = 1.0$ m/s; $c_1 = 0.03$; $c_2 = 0$; and consequently $q = \frac{\pi}{4} d_1^2 v_1 = 0.2810 \times 10^{-1}$ m^3/s; $Q = \frac{\pi}{4} d_2^2 v_2 = 0.7297 \times 10^{-1}$ m^3/s. Figure 3 shows the solid models of transverse mixers with various jet injection angles created with the ProENGINEER software. In order to compare the mixing efficiency of various transverse mixers, we present in Fig. 4 the quantitive measures based on the computation results at the corresponding cut planes. Figures 5 and 6 depict the mass-ratio contours and pressure distribution of transverse mixers with different injection angles. As can be seen, mixing efficiency of the pipe mixer with a 90^o injection angle is better than that of the mixers with acute angles, and by pointing the injection jet upstream, i.e., $\theta > 90^o$, only slight improvement can be achieved. This conclusion correlates with the experimental finding discussed in Ref. [9]. However, in the paper industry, in addition to the mixing efficiency, we also have to consider the large-scale vortices where fiber flocks or bundles may form. As is clearly visible in Fig. 6, significant vortices do exist near the injection point in transverse pipe mixers with right or obtuse injection angles. Furthermore, to avoid having the jet impact on the wall and consequently create the pressure pulsation and flow disturbance in the approach flow system, we may have to consider the jet trajectory. It is shown from the absolute velocity band plots in Fig. 7 that the jet trajectories of the transverse mixers with acute injection angles are less likely to impact the opposite wall. More detailed information on the jet trajectory is available in Refs. [3] and [6].

3.2 Concentric Mixers

In the paper industry, concentric mixers are also used extensively. An early computational study on this subject is presented in Ref. [4]. In the concentric mixers

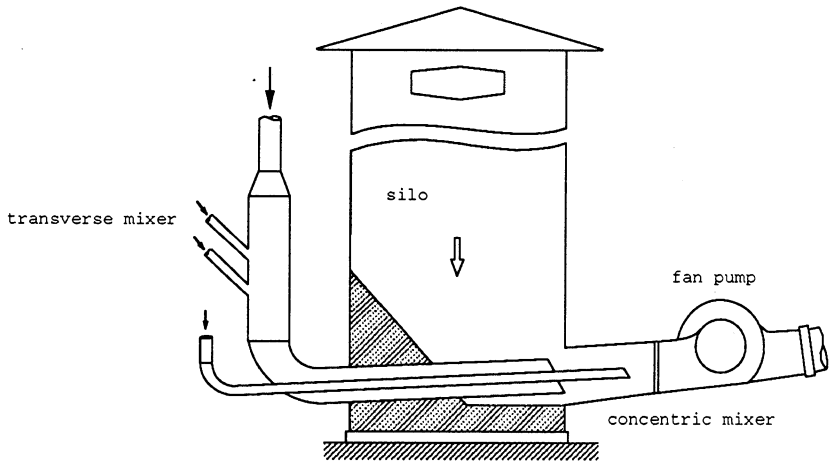

Figure 1: A typical silo pipe mixing system.

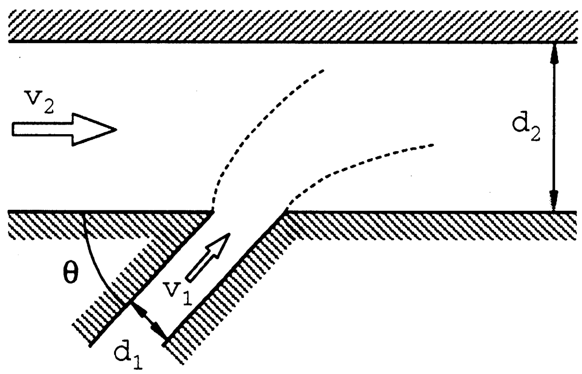

Figure 2: A typical transverse pipe mixing model.

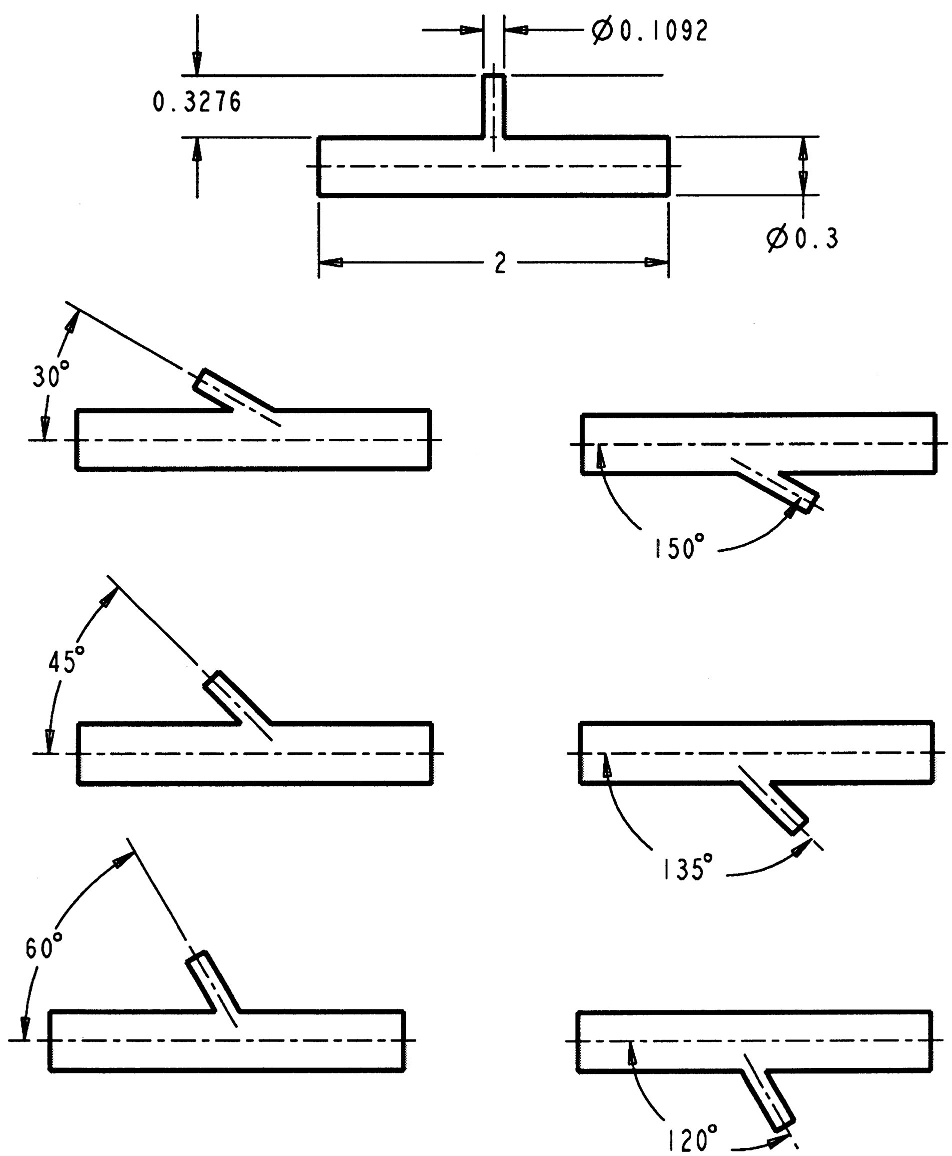

Figure 3: Solid models of transverse mixers with various jet injetion angles. (Generated with the ProENGINEER software.)

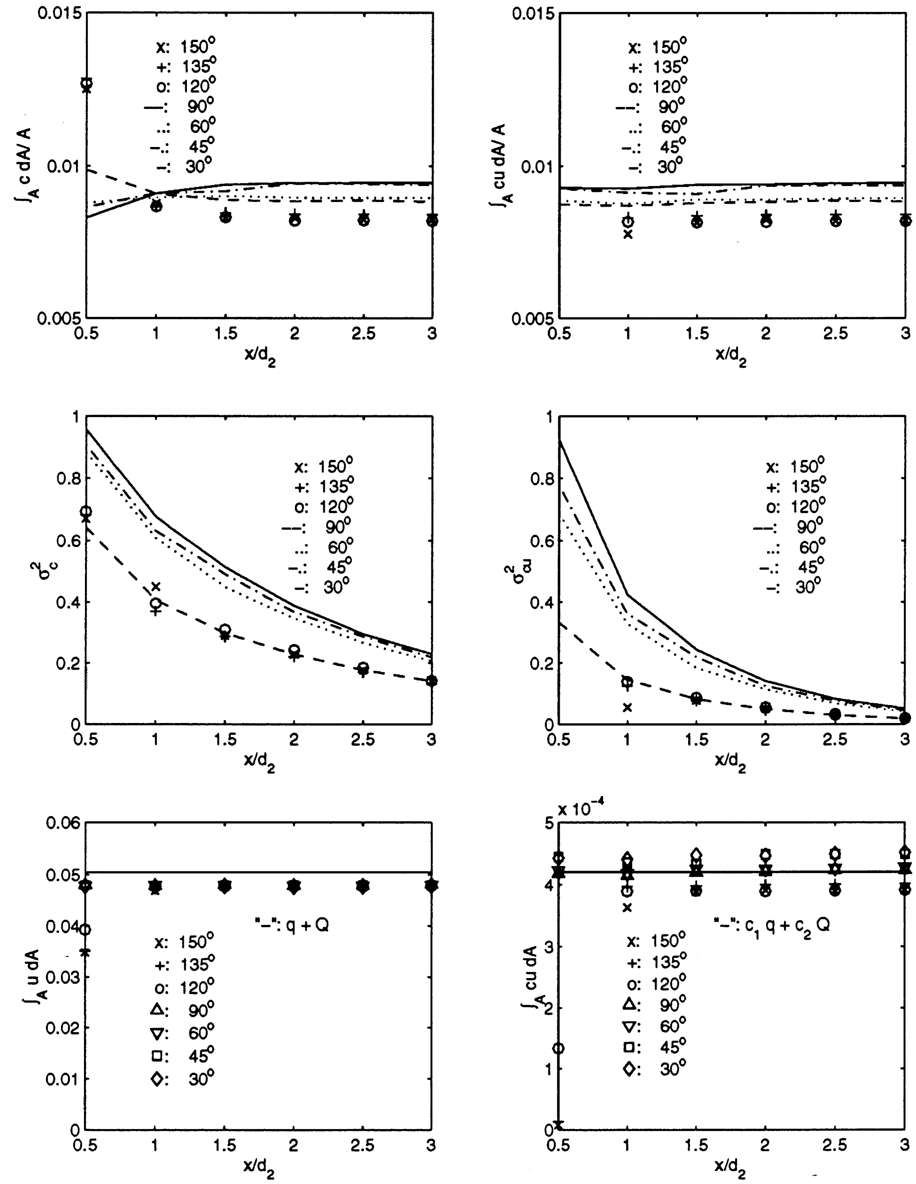

Figure 4: Mixing uniformity measures of various transverse pipe mixers.

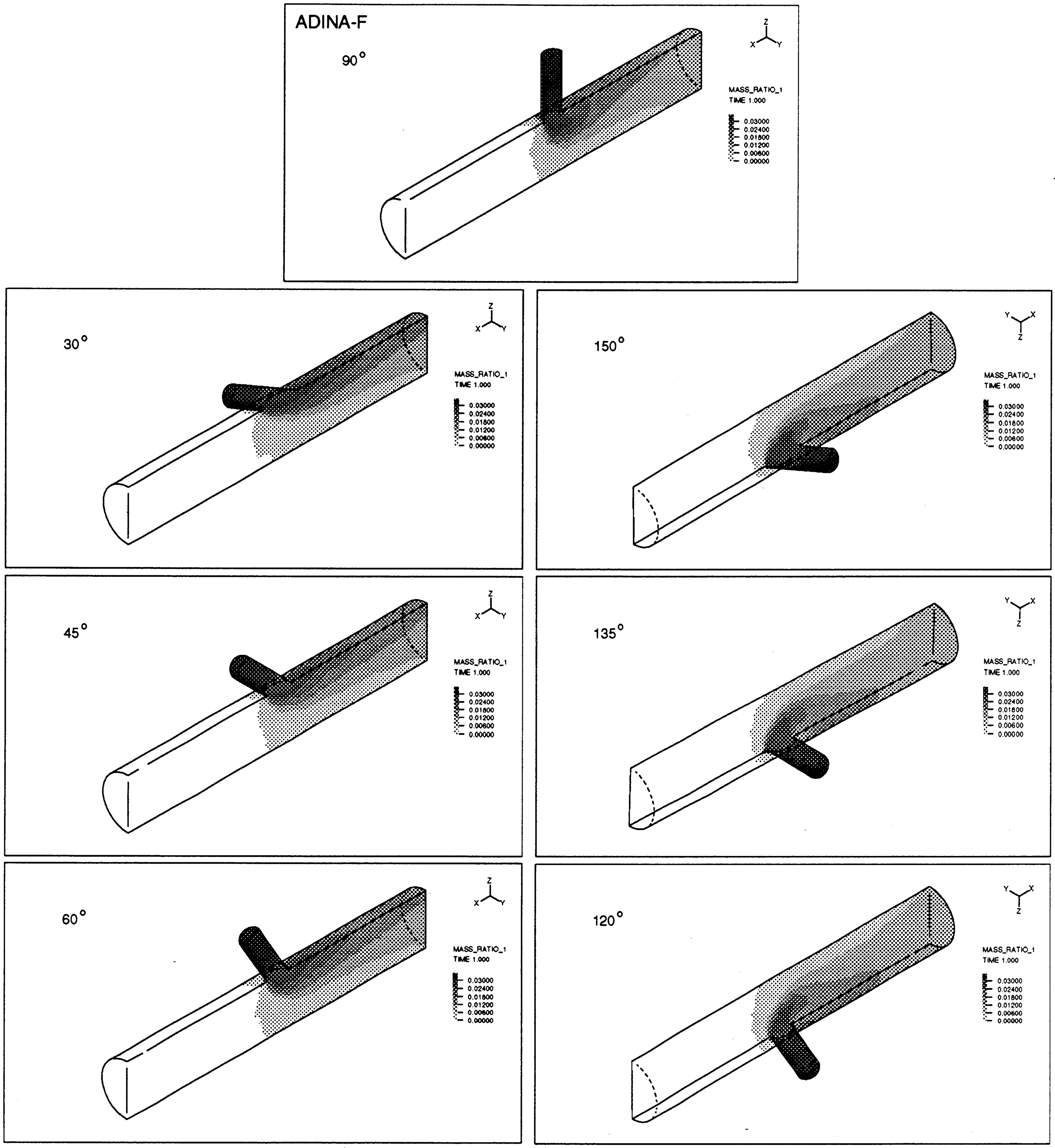

Figure 5: Tracer distribution (mass-ratio) of transverse pipe mixers with various injection angles.

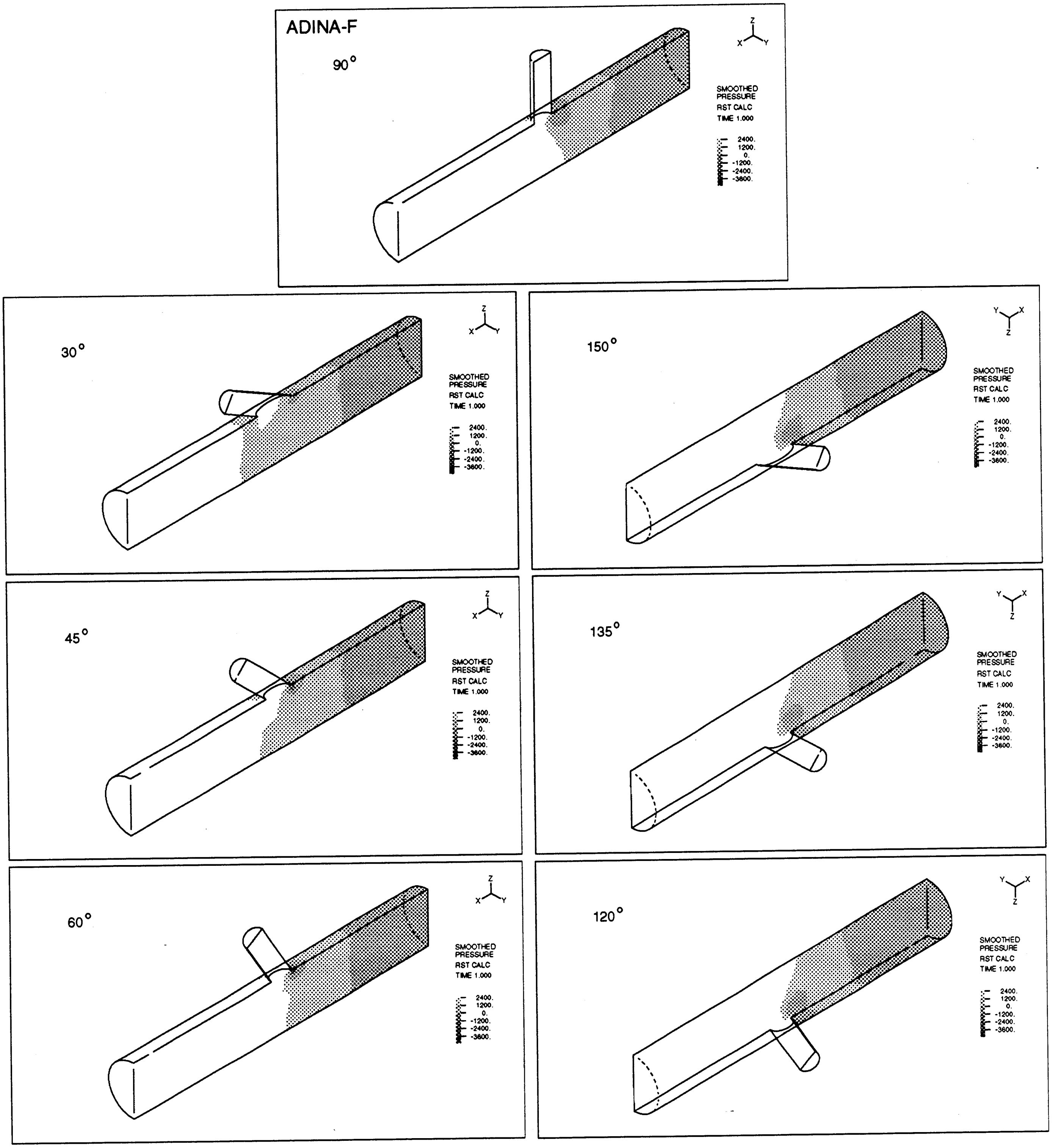

Figure 6: Pressure band plots of transverse pipe mixers with various injection angles.

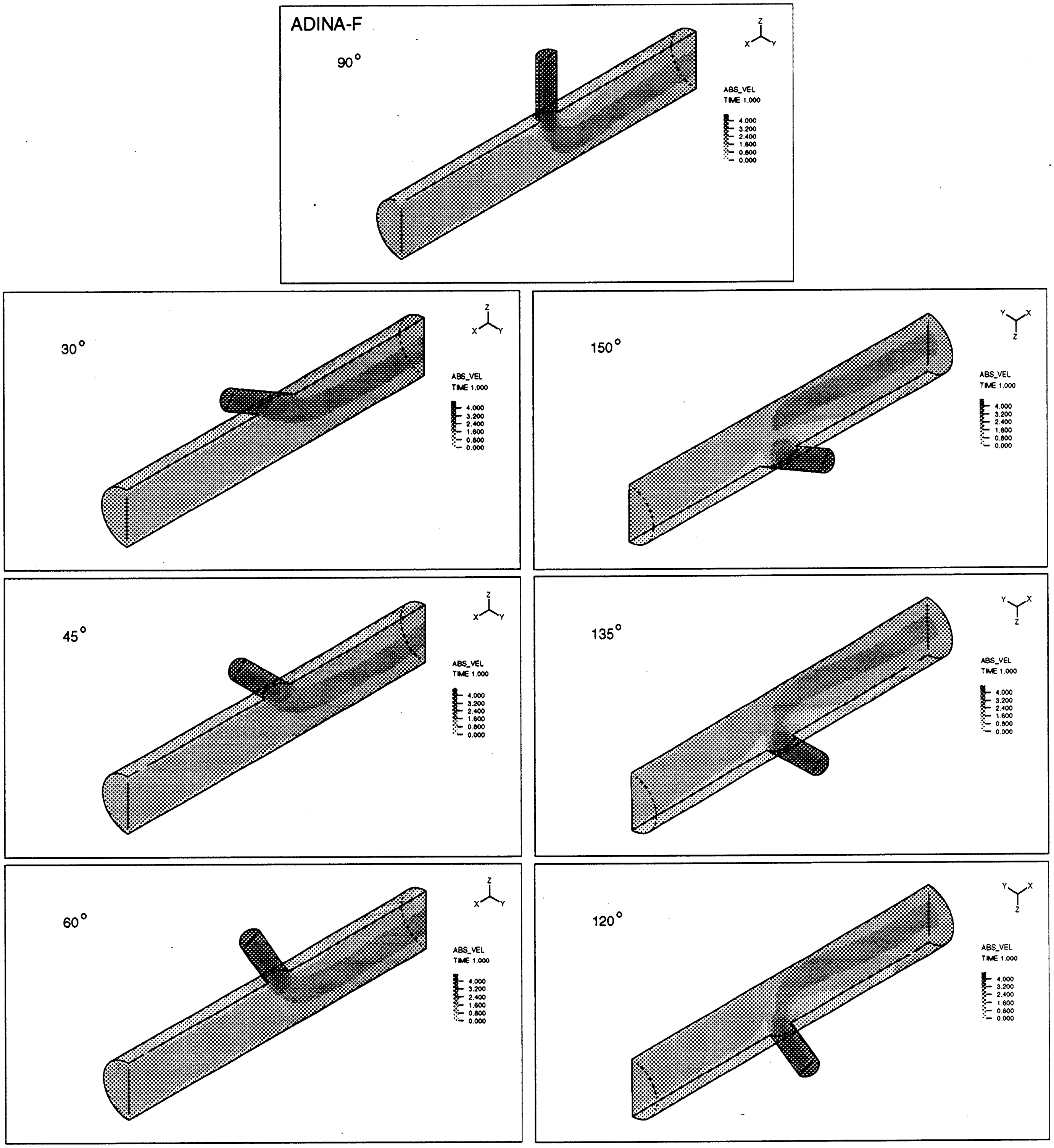

Figure 7: Velocity contour of transverse pipe mixers with various injection angles.

depicted in Fig. 8, two pipes are installed coaxially with the smaller one contained in the large pipe, and fiber stock within the small pipe is injected into the large pipe, which normally contains low consistent fiber stock or white water with lower velocity. The possible variations of concentric mixers are the nozzle cut angle θ and nozzle shape.

We compare the concentric mixers with the following physical parameters: $d_{1i} = 0.1092$ m; $d_{1o} = 0.1244$ m; $d_2 = 0.3048$ m; $v_1 = 3.0$ m/s; $v_2 = 1.2$ m/s; $c_1 = 0.03$; $c_2 = 0$; and consequently, $q = \frac{\pi}{4} d_{1i}^2 v_1 = 0.2810 \times 10^{-1}$ m^3/s; $Q = \frac{\pi}{4}(d_2^2 - d_{1o}^2) v_2 = 0.7297 \times 10^{-1}$ m^3/s. Figure 9 shows the solid models of four concentric mixers with various jet nozzles created with the ProENGINEER software. The quantitive measures at the corresponding cut planes are presented in Fig. 10. Figure 11 depicts the mass-ratio contours of four concentric mixers. It is interesting to note that in this set of configurations commonly used by the paper industry, the concentric pipe mixer is more effective than the transverse pipe mixer, and the nozzle shapes do not affect the mixing very much. This conclusion is counterintuitive concerning the existing knowledge in chemical engineering areas that the tangential mixing efficiency is only one sixth of the normal mixing efficiency [6]. Nevertheless, we notice that the ratio of the injection jet radius and the main pipe radius in chemical engineering areas is often small, i.e., the jet is in effect issued into an infinite body of fluid, which is not the case in the paper industry. Of course, further work must be done to optimize these geometries, that is, for a fixed flow ratio q/Q and distance-to-mixing ratio x/d_2, the optimum diameter ratio must be determined to minimize the variation coefficients σ_c and σ_{cu}.

To further the investigation of nozzle shape effects, we compute another set of geometry and velocity ratio. As can be seen from Figs. 12 and 13 the mixing

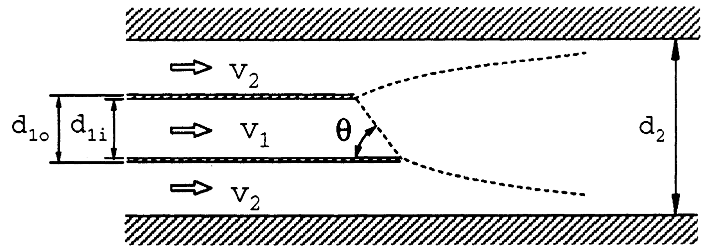

Figure 8: A typical concentric pipe mixing model.

efficiency of the contracting nozzle is much better than that of flat nozzles with various cut angles.

3.3 Multijet Mixers

As a relatively new mixing idea, multiple jets are often used to impinge on each other to create a more efficient mixing zone. Early experimental and computational studies are reported in Refs. [2] and [8]. It is conceivable that in the near future multijet mixers will be introduced in the paper industry along with the current coaxial and transverse mixers.

In this work, we compare three multijet mixers (2, 3, and 4 jets) with the corresponding transverse mixer with a 90^o injection angle. Different multijet mixers are indicated with the jet number n. The physical parameters are listed as follows: $d_1 = 0.7722 \times 10^{-1}$ m; $d_2 = 0.3048$ m; $c_1 = 0.03$; $c_2 = 0$; and consequently $q = n\frac{\pi}{4}d_1^2v_1 = 0.2810 \times 10^{-1}$ m^3/s; $Q = \frac{\pi}{4}d_2^2v_2 = 0.7297 \times 10^{-1}$ m^3/s. Figure 15 shows the solid models of three multijet mixers created with the ProENGINEER software. The quantitive measures at the corresponding cut planes are shown in Fig. 16. Figures 17 and 18 depict the mass-ratio contours and pressure distributions of multijet mixers along with the corresponding transverse mixer with a 90^o injection angle. Compared with the single transverse jet mixer, the mixing efficiency of

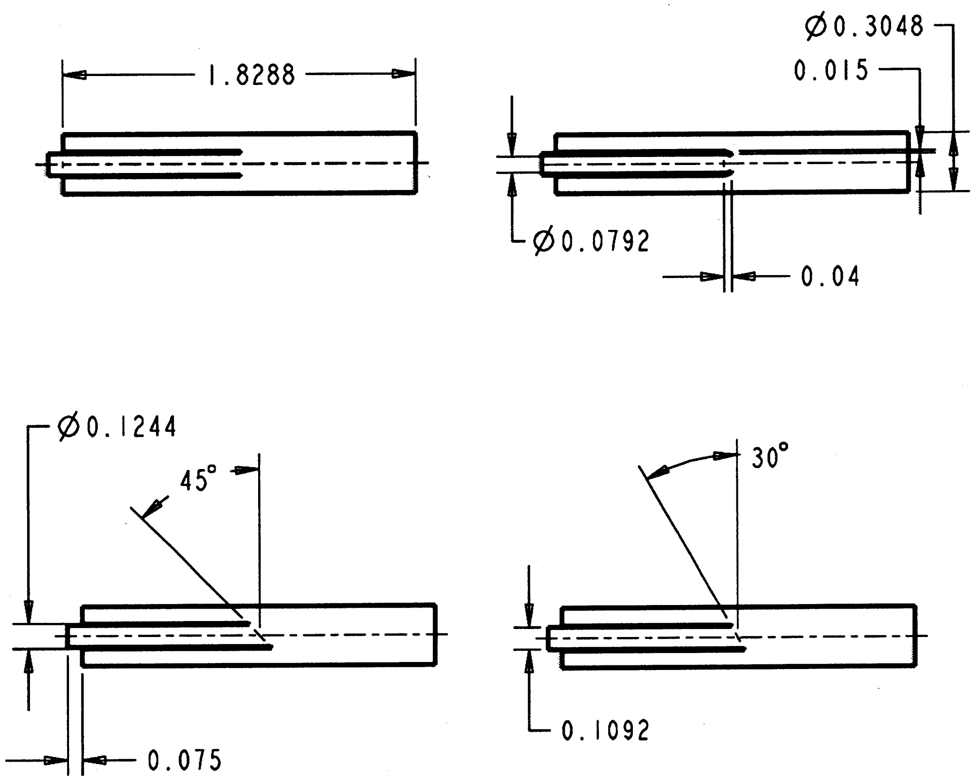

Figure 9: Solid models of concentric pipe mixers with various nozzle designs. (Generated with the ProENGINEER software.)

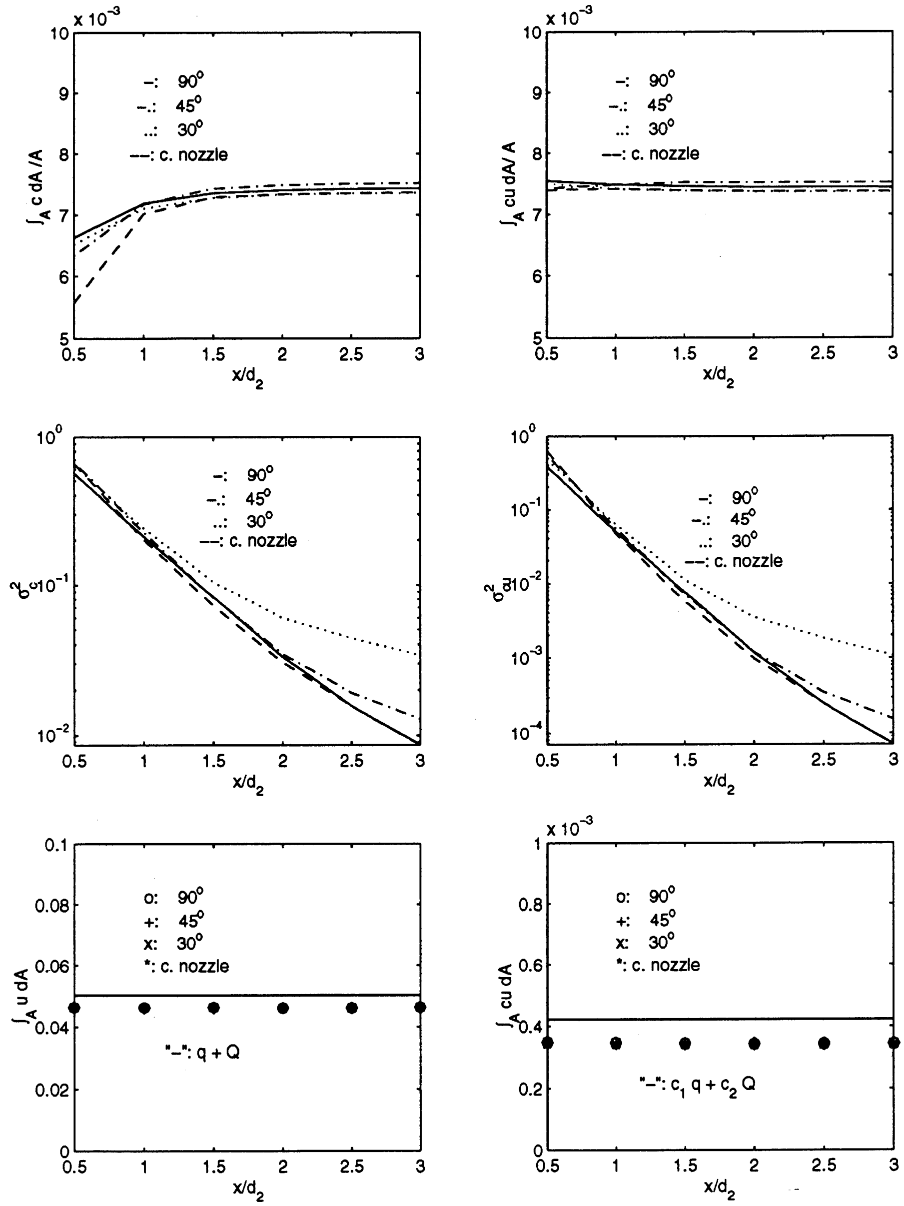

Figure 10: Measures of mixing uniformity of various concentric pipe mixers.

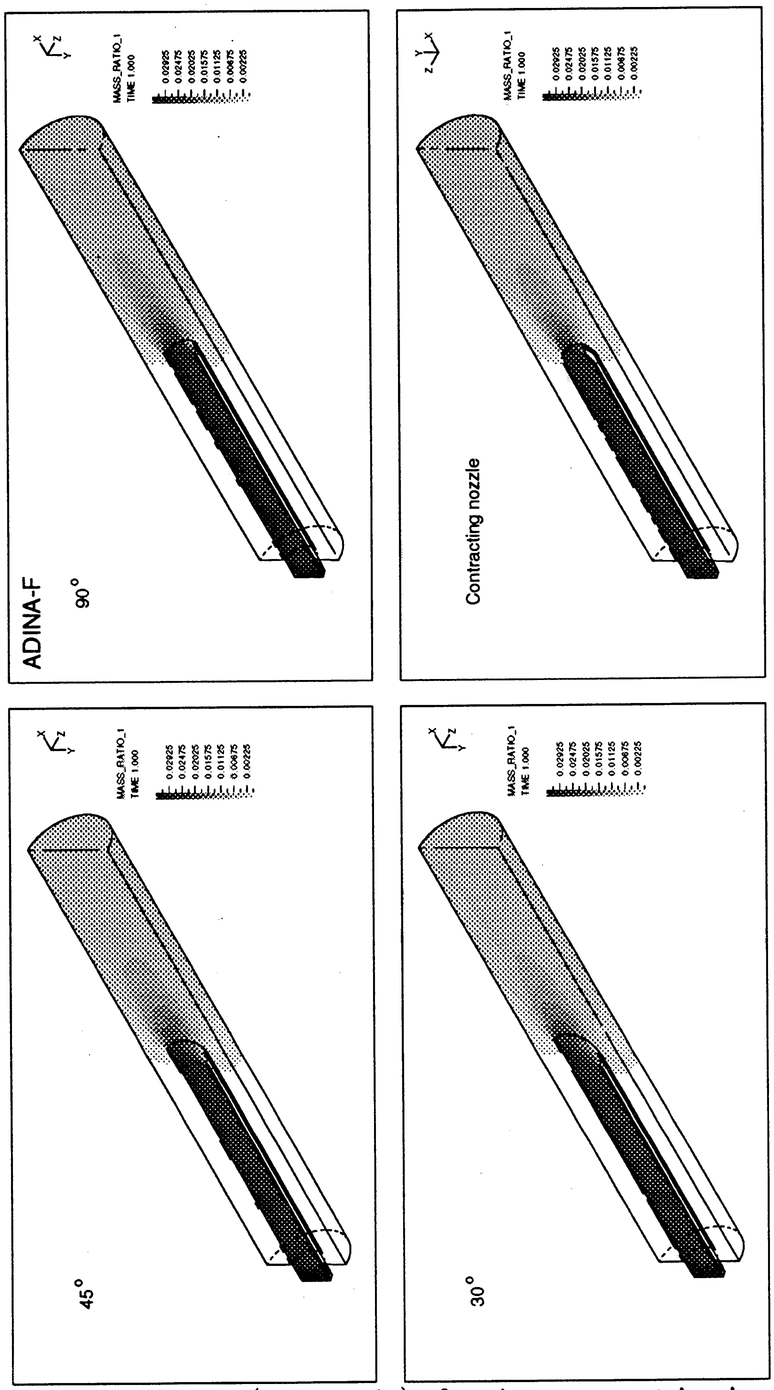

Figure 11: Tracer distribution (mass-ratio) of various concentric pipe mixers.

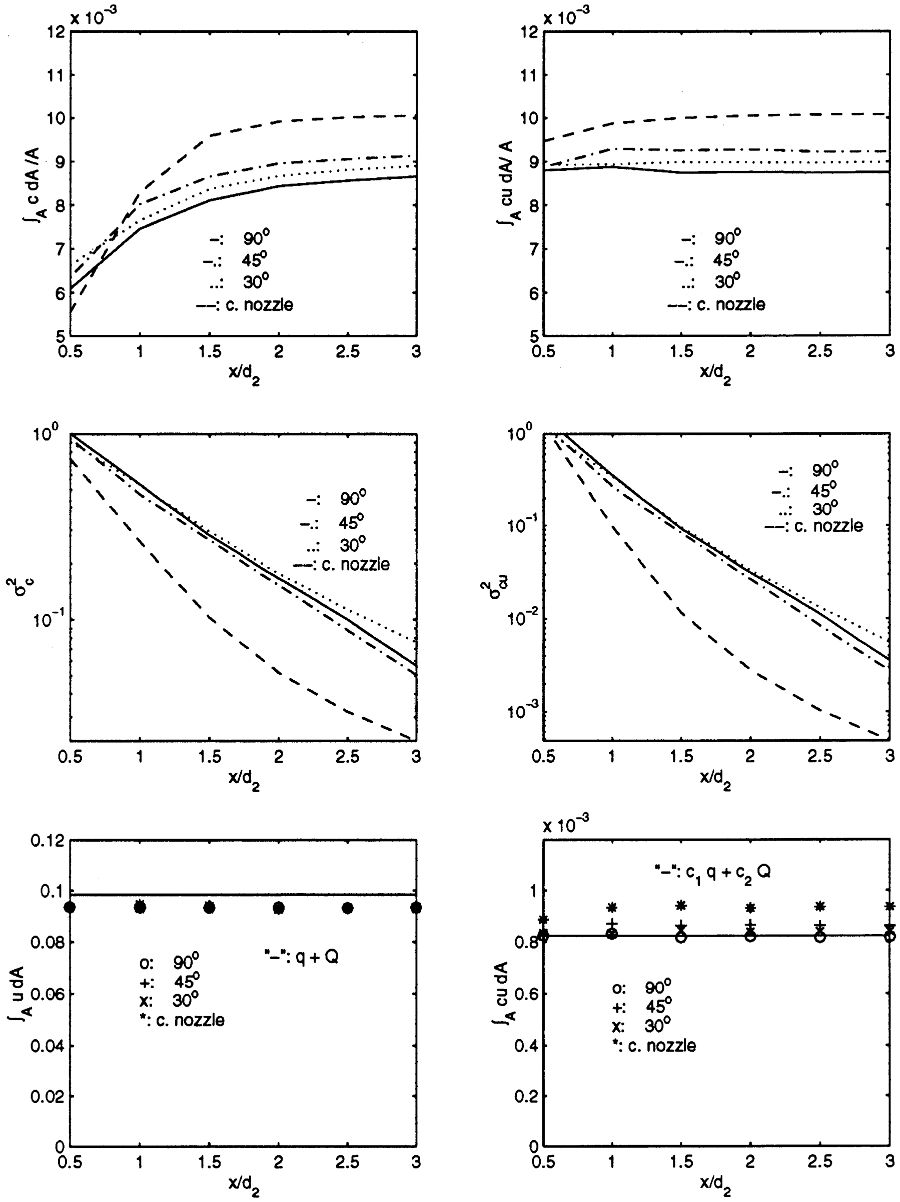

Figure 12: Measures of mixing uniformity of various concentric pipe mixers. (d_{1i} = 0.1526 m; d_{1o} = 0.1676 m; d_2 = 0.4572 m; v_1 = 3.0 m/s; v_2 = 1.0 m/s.)

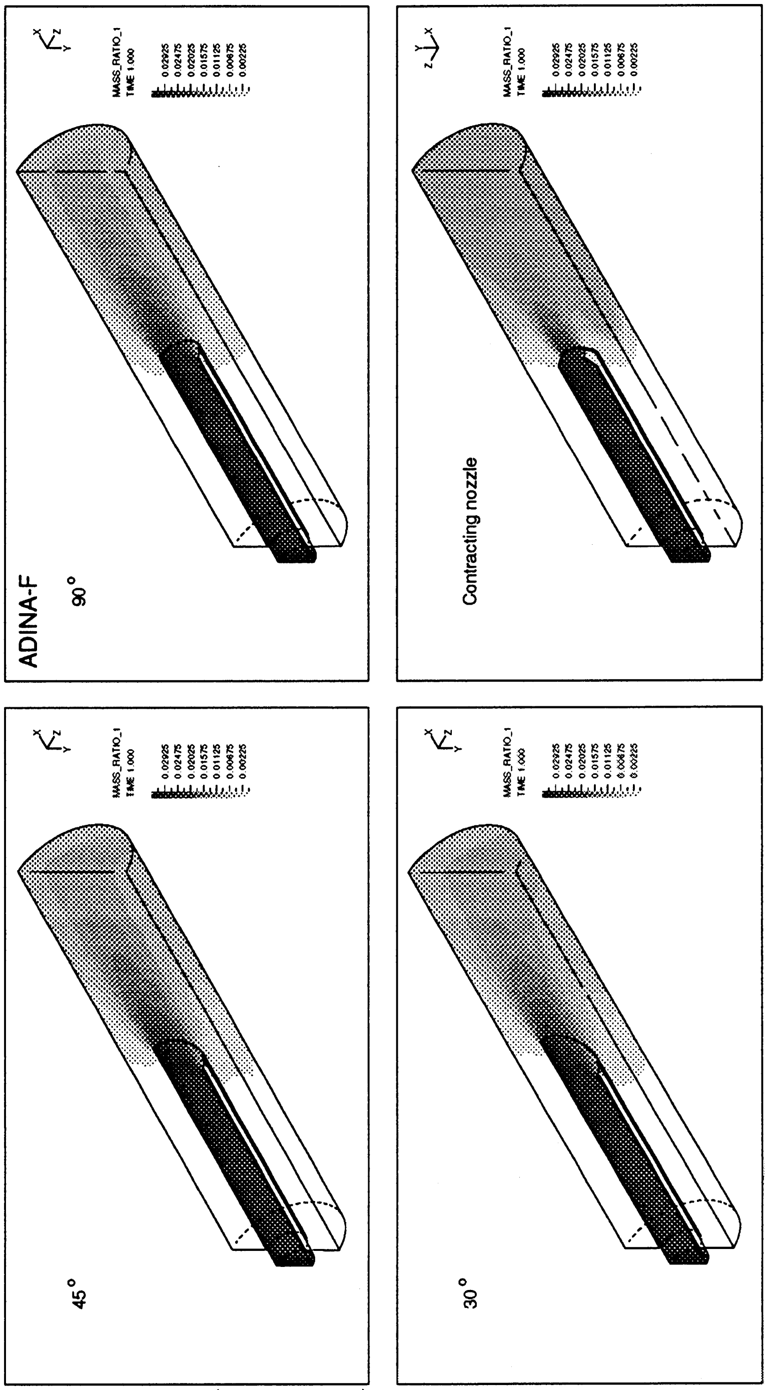

Figure 13: Tracer distribution (mass-ratio) of various concentric pipe mixers with different ratio of inner and outer pipe radii. (d_{1i} = 0.1526 m; d_{1o} = 0.1676 m; d_2 = 0.4572 m; v_1 = 3.0 m/s; v_2 = 1.0 m/s.)

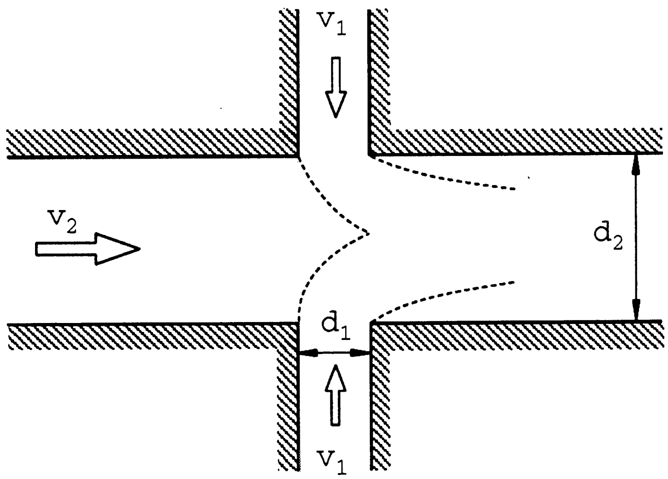

Figure 14: A typical multijet pipe mixing model.

multijets is much better, and in addition, the size of the vortices near the injection point is reduced. It is also interesting to note that multijets with an even number of jets perform better than those with an odd number of jets. For example, although more jets within the multijet mixer imply better mixing, a two-jet mixer is better than a three-jet mixer for $x/d_2 > 1.5$.

3.4 Silo Unit

As illustrated in the mathematical model depicted in Fig. 19, the silo is a cylindrical water storage tank with a constant water level. The inner pipe protruding into the fan pump inlet zone contains a higher consistency fiber stock (e.g., 3%), and the concentric outer pipe collects the recirculation diluted stock (e.g., 2%). In this paper, we assume that the concentric pipes are rigid. The issue of dynamic instability of these suspended pipes is addressed in Ref. [13].

Industry research suggests that the fan pump location can directly affect the paper sheet formation. Although many practical aspects, including the suspended pipe

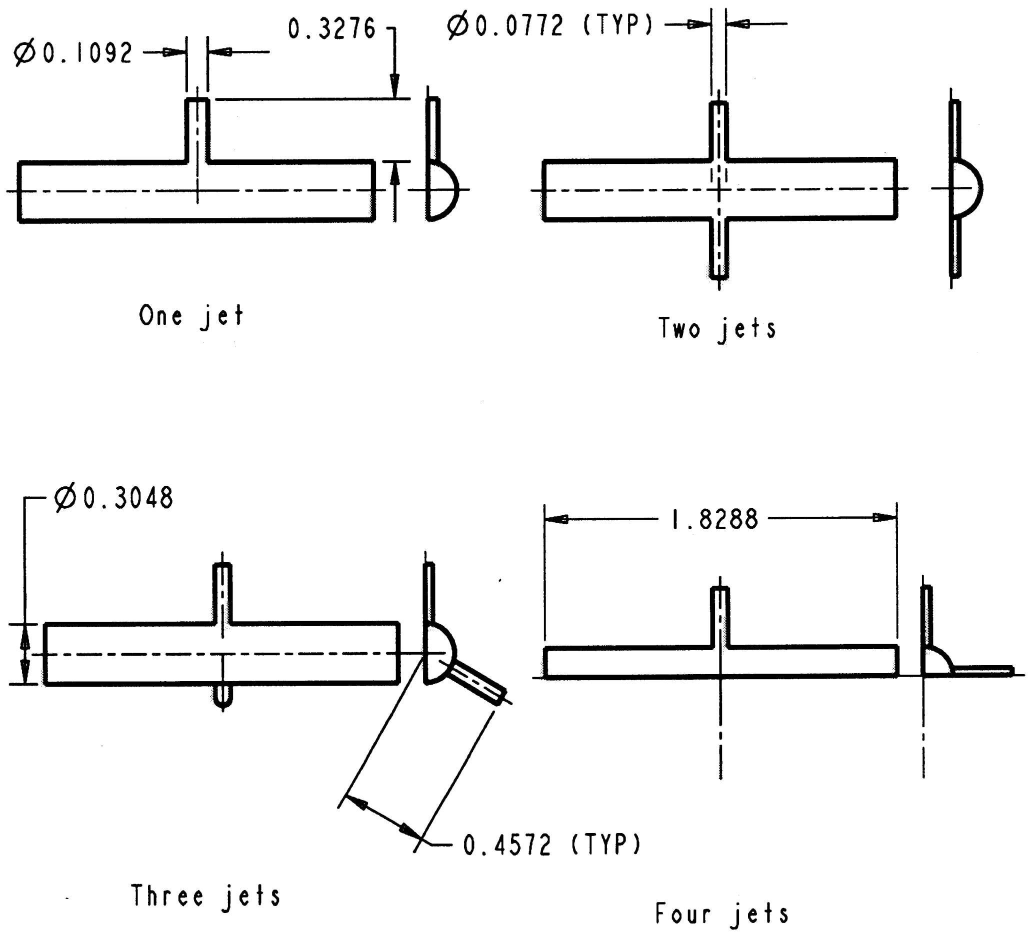

Figure 15: Solid models of various designs of multijet pipe mixers. (Generated with the ProENGINEER software.)

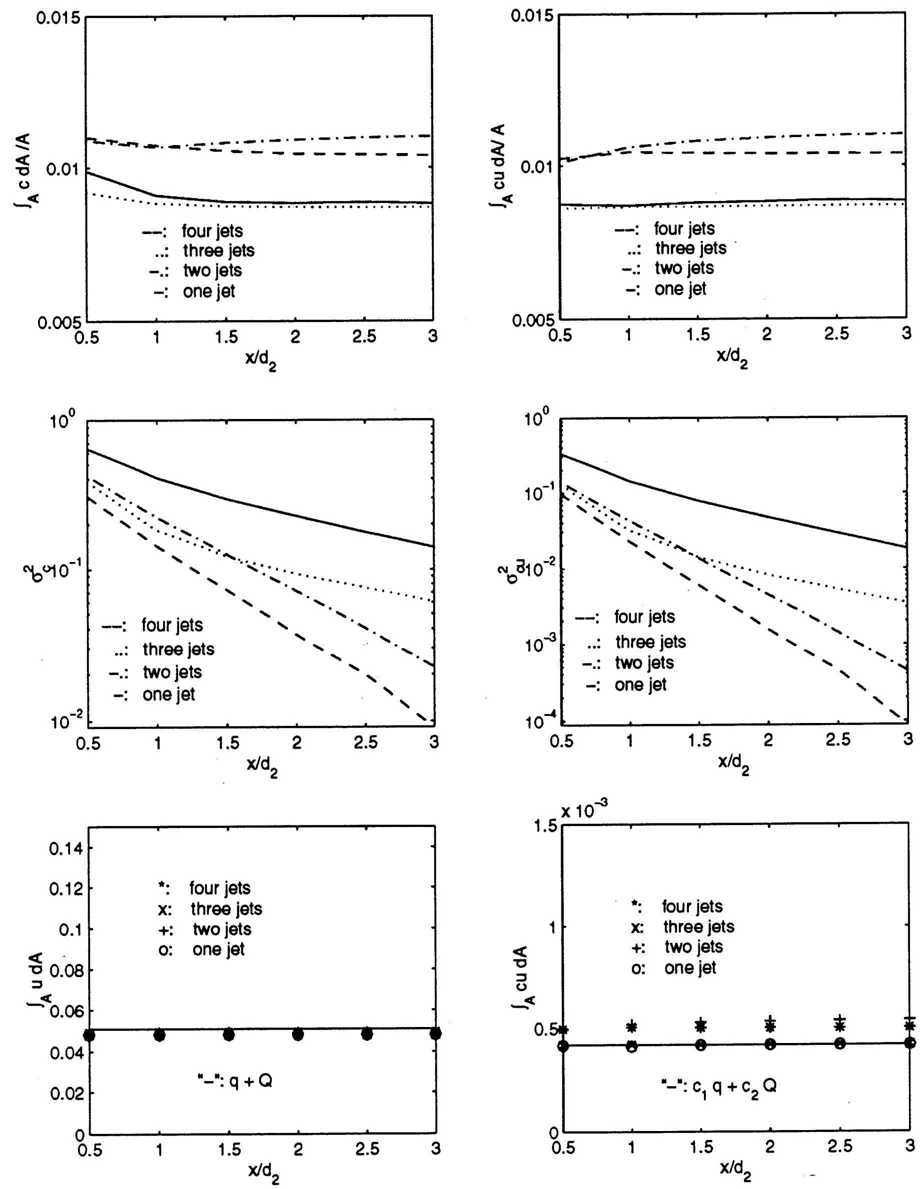

Figure 16: Measures of mixing uniformity of various multijet pipe mixers.

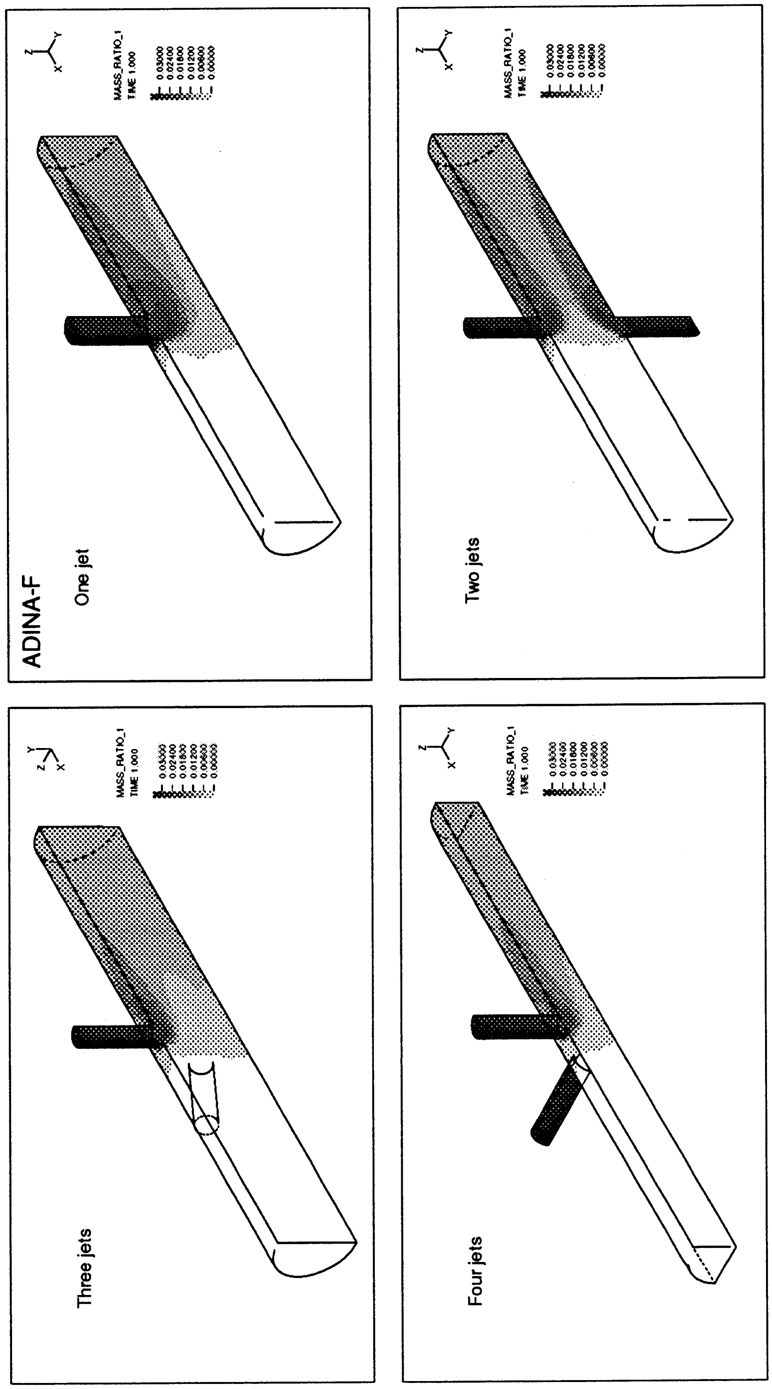

Figure 17: Tracer distribution (mass-ratio) of various multijet pipe mixers.

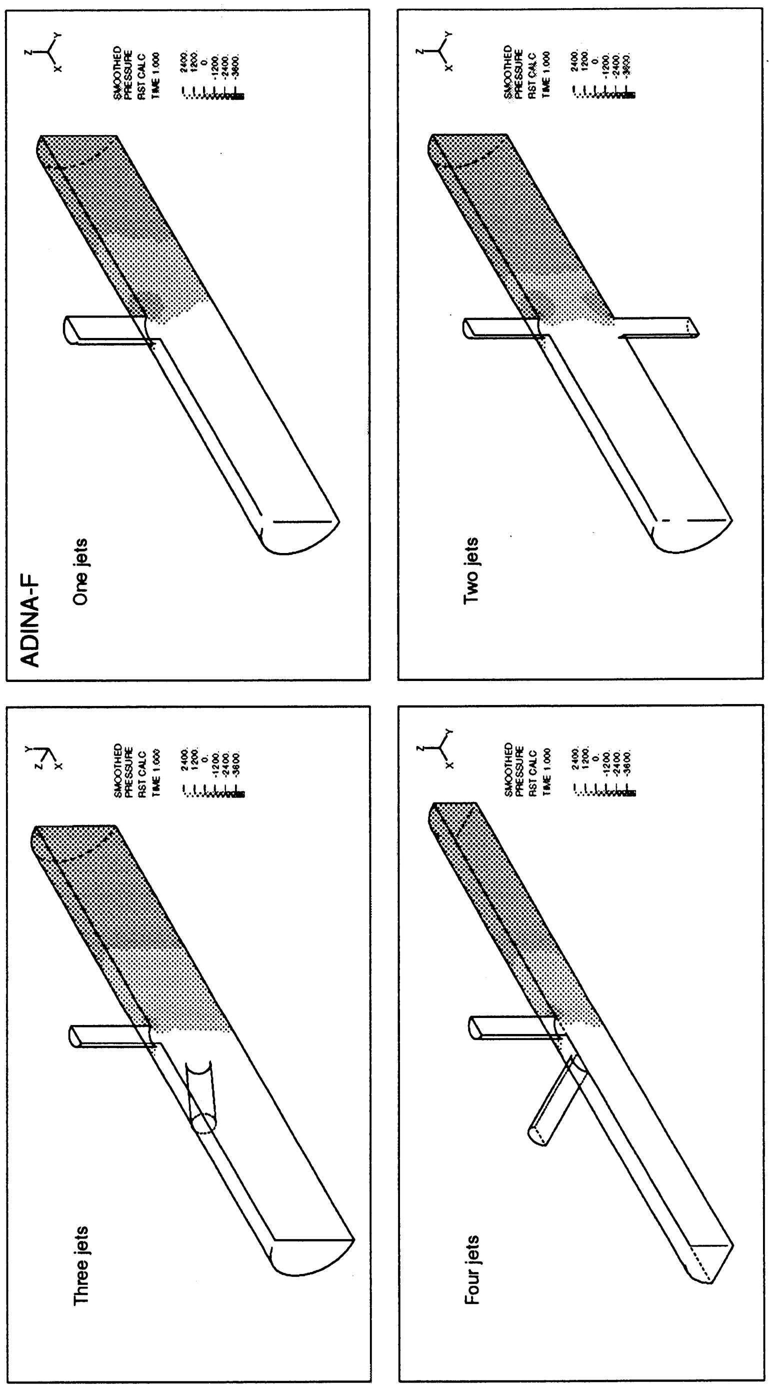

Figure 18: Pressure band plots of various multijet pipe mixers.

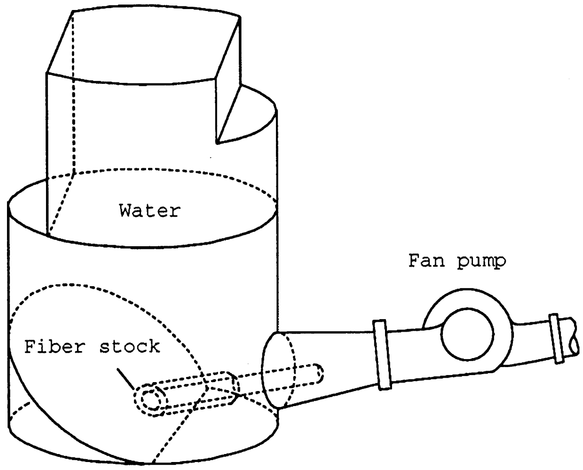

Figure 19: A typical silo pipe mixing unit model.

vibration, may contribute to the smooth pump operation or even the sheet property variations, in this work, we focus on the issue of fan pump location. Therefore, the basic consideration is the same as those for transverse, concentric, or multijet mixers, where the mixing uniformity is measured at a certain distance down stream from the injection point.

We consider four silo units illustrated in Fig. 20. Case A represents the initial design configuration. Case B includes the modification with a corner cut. Case C has a longer outlet pipe. Case D combines two modifications in Cases B and C together. Figure 20 shows the solid models of four silo units created with the ProENGINEER software. The quantitive measures at the corresponding cut planes for each case are presented in Fig. 21. Figure 22 presents the mass-ratio contours at six different axial locations of the outlet pipe in four silo units. It is evident by comparing Cases B, C, and D with Case A that mixing efficiency can be significantly improved by the elongation of the outlet pipe; and the corner cut is not a dominant factor.

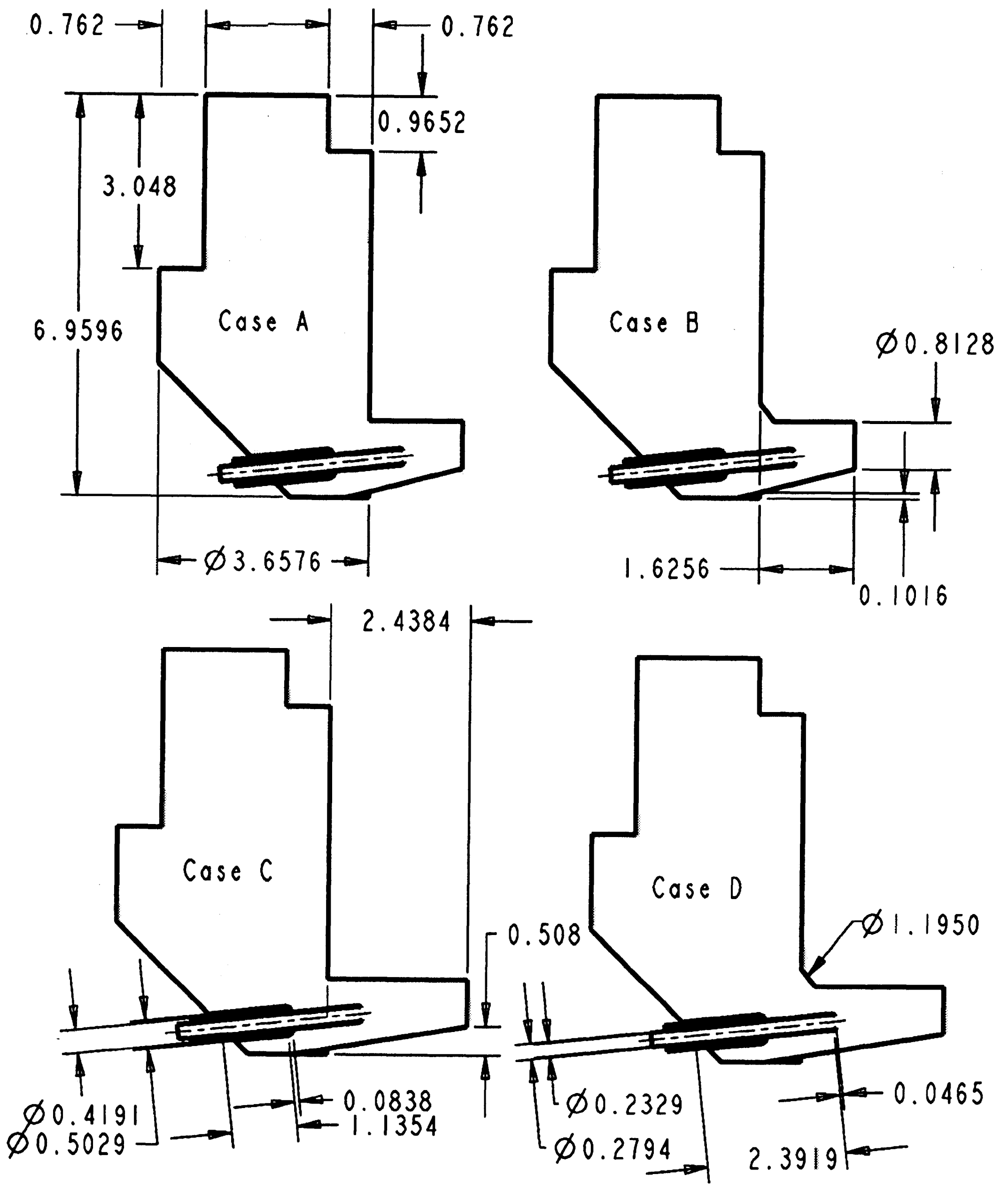

Figure 20: Solid models of various modifications of silo pipe mixing models. (Generated with the ProENGINEER software.)

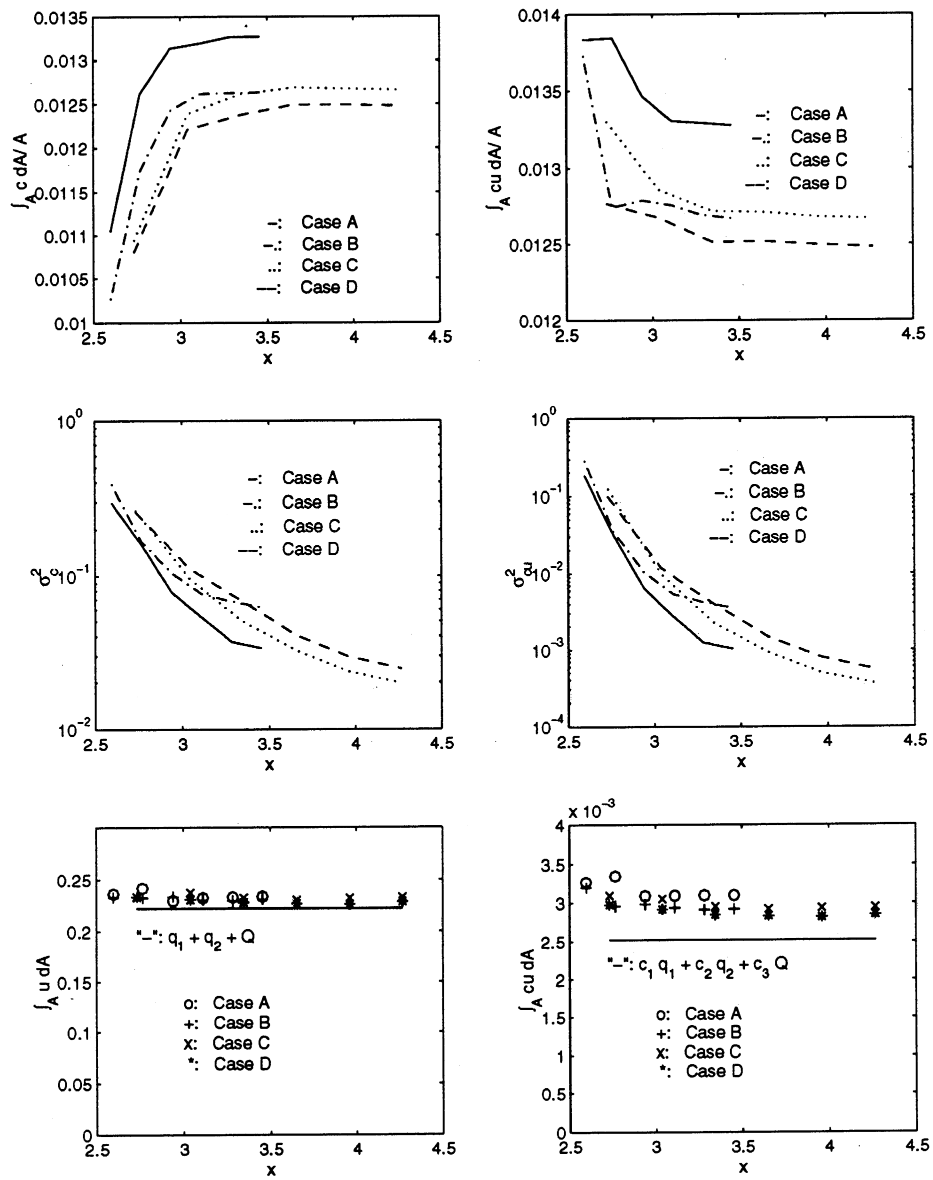

Figure 21: Measures of mixing uniformity of various silo pipe mixing arrangements. (q_1 and q_2 are the flow rates of the inner and outer concentric pipes, and Q is the flow rate of the silo. c_i is the corresponding fiber consistency.)

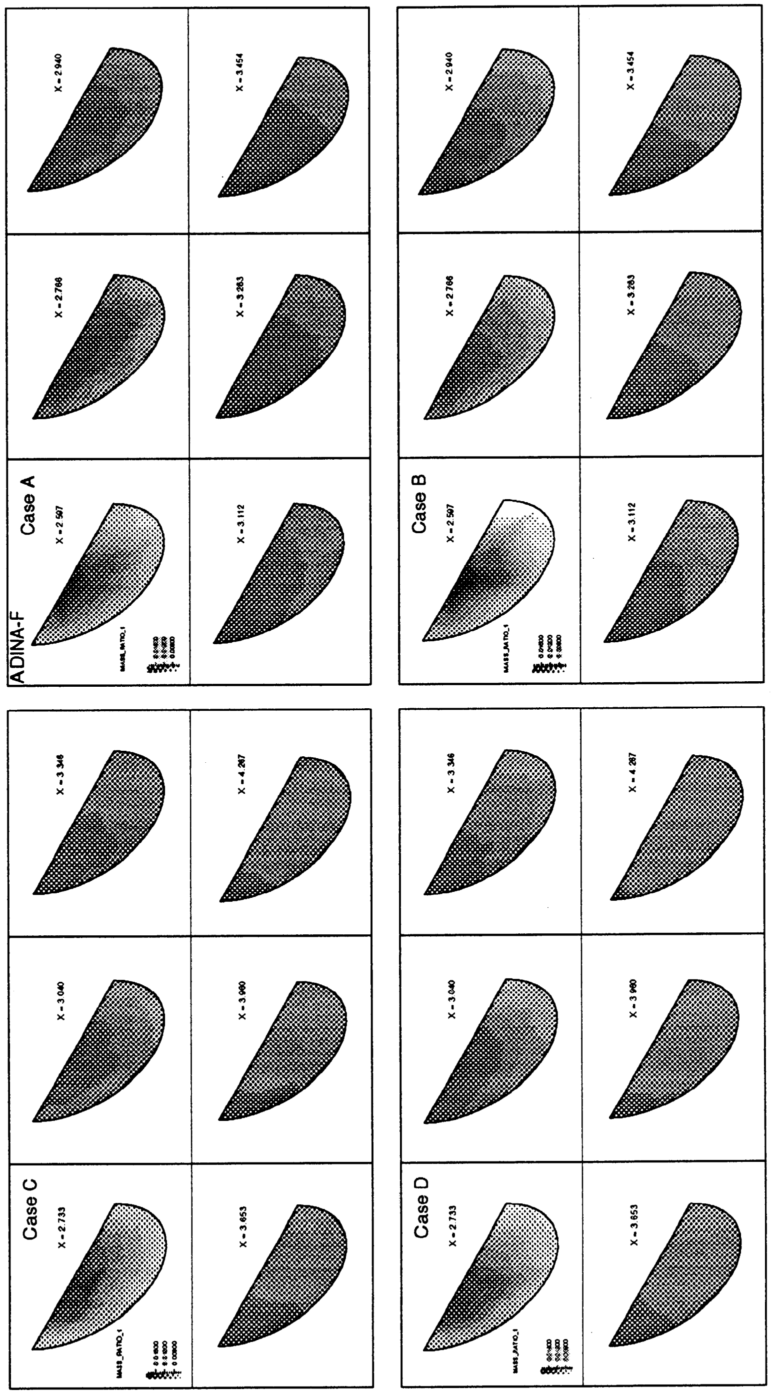

Figure 22: Tracer distribution (mass-ratio) at various cut planes of four silo units.

4 Conclusions

In this paper, a systematic numerical study of various pipe mixers and silo mixing units has been conducted with the ADINA software. In summary, we obtain the following information pertaining to the design of the considered mixing arrangements:

(1) Although transverse mixers with an injection angle of $\theta \geq 90^o$ are more efficient in mixing, they tend to produce large-scale vortices near the injection point, and the jet is more susceptible to impacting the opposite wall. Therefore, in the paper industry, an acute injection angle may be considered, and in practice, a longer distance downstream away from the injection point is recommended to be reserved to compensate for the loss of mixing efficiency.

(2) In concentric mixers, with the same input flow rates, for the geometries used in this work (typical geometries in the paper industry), the mixing efficiency is much higher than those of the corresponding transverse and multijet mixers. In addition, from the further investigation with different relative injection jet size, we find that mixing efficiency can be greatly improved in the case of the contracting nozzle. This indicates that in the case of mixing chemical additives, contracting nozzle is recommended. In general, a flat nozzle with various cut angles θ does not affect mixing significantly.

(3) Multijet mixing is, in general, better than single jet mixing, and an even number of jets is recommended.

(4) In the silo mixing unit design, increasing the outlet pipe length has a much greater effect on the mixing efficiency than the corner cut.

References

[1] K.J. Bathe, H. Zhang, and X. Zhang. Some advances in the analysis of fluid flows. *Computers & Structures*, 64(5/6):909–930, 1997.

[2] Y.R. Chang and K.S. Chen. Prediction of opposing turbulent line jets discharged laterally into a confined crossflow. *International Journal of Heat Mass Transfer*, 38(9):1693–1703, 1995.

[3] Z. Feng, X. Wang, and L.J. Forney. Single jet mixing at arbitrary angle in turbulent tube flow. *ASME Fluids Engineering Division*, 1998. Submitted.

[4] P. Givi and J.I. Ramos. On the calculation of heat, mass and momentum transport in coaxial jets and mixing layers. *Int. Comm. Heat Mass Transfer*, 12:323–336, 1985.

[5] J.B. Gray. Turbulent radial mixing in pipes. In V.W. Uhl and J.B. Gray, editors, *Mixing: Theory and Practice Vol. III*, pages 63–130. Academic Press, 1986.

[6] D.P. Hoult, J.A. Fay, and L.J. Forney. A theory of plume rise compared with field observations. *Journal of the Air Pollution Control Association*, 19(8):585–590, 1969.

[7] B.E. Launder and D.B. Spalding. The numerical computation of turbulent flows. *Computer Methods in Applied Mechanics and Engineering*, 3:269–289, 1974.

[8] T. Maruyama, T. Mizushina, and S. Hayashiguchi. Optimum conditions for jet mixing in turbulent pipe flow. *International Chemical Engineering*, 23(4):707–716, 1983.

[9] T. Maruyama, T. Mizushina, and F. Watanabe. Turbulent mixing of two fluid streams at an oblique branch. *International Chemical Engineering*, 22(2):287–294, 1982.

[10] L.A. Monclova and L.J. Forney. Numerical simulation of a pipeline tee mixer. *Industrial Engineering Chemistry Research*, 34:1488–1493, 1995.

[11] A. Shanley. Pushing the limits of CFD. *Chemical Engineering*, pages 66–67, December 1996.

[12] L.M. Sroka and L.J. Forney. Fluid mixing with a pipeline tee: Theory and experiment. *AIChE Journal*, 35(3):406–414, 1989.

[13] X. Wang and F. Bloom. Flow induced oscillations of submerged and inclined concentric pipes with different lengths. *Journal of Fluids and Structures*, 1998. Submitted.

[14] D.C. Wilcox. *Turbulence Modeling for CFD*. DCW Industries, Inc., second edition, 1994.

Flow Induced Oscillations of Submerged and Inclined Concentric Pipes with Different Lengths

by

Xiaodong Wang and Frederick Bloom

1 Introduction

In the paper industry, approach flow systems are used to dilute fiber stock with water, and, in general, consist of many pumps, screens, deareation, and piping components. One of the key components is the so-called silo water mixing unit depicted in Fig. 1. It has been discovered that the turbulent mixing of jets coming out of the concentric pipes before the fan pump contributes significantly to the smooth operation of impellers, stock consistency, and pressure variations [23]. In this paper, we consider dynamical stability issues of the suspended concentric pipes that relate directly to the design of the silo mixing unit. Because the turbulent jets coming out of the concentric pipes might introduce strong oscillations of the suspended pipes, which, in turn, can influence the jet mixing before the silo fan pump, vibration problems associated with such pipes must be understood and resolved.

The basic goal of this work is to determine the protruded inner tubular pipe oscillation frequency induced by both the internal and external fluid flows. Considering the fact that the inner pipe carries thick fiber stock and has a much smaller diameter, we will focus exclusively on the inner pipe vibration and address the following issues: (i) what is the frequency range for a given pipe system design; (ii) what is the effect of the angle of inclination; (iii) what is the optimal choice of pipe flow velocities and radii that yield prescribed volume flow rates; (iv) what are the critical lengths of the pipes protruding into the fan pump inlet zone; and (v) how important is the depth of the submerged pipe system.

The problem analyzed in this paper belongs to a major subject area within the general realm of fluid-structure interaction problems. The subject of flow-induced vibrations and stability of single pipes (or flexible cylinders) and concentric piping arrangements has a long history beginning with the work of Benjamin [2] [3] and Paidoussis [14] [15]. It was shown by Gregory and Paidoussis [6] that when the flow velocity in a tube, fixed at the upstream end and free at the other, is increased beyond a certain critical value, the system becomes unstable, and small random perturbations grow into lateral oscillations of large amplitude. The dynamics and stability of flexible pipes conveying fluid where the flow velocity may be either constant or has a small superimposed harmonic component were also studied by Paidoussis and Issid [18] and Chen [4].

The active control of flutter, occurring in a cantilever tube conveying fluid, through the use of piezoelectric actuators, has been discussed in a recent paper by Lin and Chu [10], while the stability of flow-induced motions of tubular beams conveying fluid, which possess an inclined terminal nozzle, has been analyzed by Lundgren, Sethna, and Bajaj [11]. In Laithier and Paidoussis [9], the equations of motion of an initially stressed Timoshenko tubular beam subjected to a tensile follower load, and conveying fluid, are derived by using Hamilton's principle instead of the Newtonian force-balance approach. Recent work on the stability of curved flexible pipes conveying fluid include that of Aithal and Gipson [1]; Misra, Paidoussis, and Van [12]; and Dupuis and Rousselet [5]. In a subsequent work [17], Paidoussis presented a general theory for the dynamics of slender cylindrical beams immersed in purely axial, uniform, steady flow; in this case, the cylinders may be considered either isolated or as parts of a cluster of identical cylinders.

In Hannoyer and Paidoussis [7], the authors examine the dynamics and stability of cylindrical tubular beams conveying fluid, which are simultaneously subjected to both internal and external axial flows; the analysis takes into account the boundary-layer thickness of the external flow, internal dissipation, and gravity effects, but the external flow is not a confined flow. The dynamical behavior of flexible cylinders (not conveying fluid), which are placed centrally within a narrow cylindrical flow channel and are subjected to an external axial flow, was considered by Paidoussis and Pettigrew [20]; the effect of various parameters, such as the size of the annular confinement, on the stability characteristics of the pipe was analyzed, and experimental observations were compared with the predictions of the theoretical model. In Ref. [8], Hannoyer and Paidoussis developed a general theory for the dynamics of slender, nonuniform axisymmetric beams subjected to either the internal or external flow, or to both simultaneously; solutions of the relevant equations of motion were presented for cantilevered conical beams in external flow and for beams with a conical internal flow passage.

In summary, significant research efforts have been directed toward studying the dynamics and stability of the following types of pipes and piping systems: (i) flexible straight (or curved) single pipes conveying fluids, (ii) a single flexible cylindrical body immersed in an unconfined fluid flowing parallel to the body axis, (iii) a flexible cylinder in a confined axisymmetric axial flow, and (iv) coaxial cylindrical shells containing flow fluid; this latter topic, which is discussed in detail in Refs. [13] and [19], will not be of any direct interest to us in this paper as we consider only low frequency fluctuations and model the inner pipe as a tubular beam.

The main objective of this paper is to propose a mathematical model for inclined, submerged, concentric pipes with different pipe lengths. In addition, the fluid forces exerted by both the confined and unconfined external flows are considered. We start with the derivation of the governing equations in Section 2 and discuss the finite difference schemes in Section 3. Finally, we present in Section 4 numerical examples relating to a typical pipe system design along with the analysis of various critical design parameters.

2 Governing Equations of Motion

A schematic diagram of the location and general configuration of the mixing pipe arrangement within the silo is shown in Fig. 1. As depicted in Fig. 2, the mathematical model of the suspended concentric pipes includes the inner pipe with a length l and the outer pipe with a length $L < l$. We note that all the pipes are submerged in silo water, and continuous flow between the two concentric cylinders only occurs in the domain $0 \le x \le L$. Under the action of the gravitational force and fluid forces, i.e., pressure and frictional forces, the inner pipe will deform and oscillate.

Using the small displacement and small strain assumptions, the body coordinates (ξ, η, ζ) (corresponding to the deformed configuration) can be projected onto the initial coordinates (x, y, z), as shown in Fig. 3, with the following results:

$$\begin{array}{llllll} \xi_x \simeq \xi, & \xi_y \simeq \xi\dfrac{\partial y}{\partial x}, & \xi_z \simeq \xi\dfrac{\partial z}{\partial x} \\ \eta_x \simeq -\eta\dfrac{\partial y}{\partial x}, & \eta_y \simeq \eta, & \eta_z \simeq 0 \\ \zeta_x \simeq -\zeta\dfrac{\partial z}{\partial x}, & \zeta_y \simeq 0, & \zeta_z \simeq \zeta \end{array} \tag{1}$$

where the in-plane and out-of-plane displacements are denoted as $y = y(x,t)$ and $z = z(x,t)$.

In this paper, we establish the force equilibrium on the deformed configurations in order to retain certain nonlinear terms at the beginning of our derivation. Nevertheless, we will focus on the linear stability analysis and leave the nonlinear analysis for the subject of a forthcoming paper.

We express the forces exerted on the inner tubular beam from the internal and external fluid flows as $(F_\xi^i, F_\eta^i, F_\zeta^i)$ and $(F_\xi^e, F_\eta^e, F_\zeta^e)$, respectively. As a consequence of Eq. (1), we may project the internal fluid forces on the initial coordinates (x, y, z) as follows:

$$\begin{aligned}
(F_\xi^i)_x &\simeq F_\xi^i, & (F_\xi^i)_y &\simeq F_\xi^i\frac{\partial y}{\partial x}, & (F_\xi^i)_z &\simeq F_\xi^i\frac{\partial z}{\partial x} \\
(F_\eta^i)_x &\simeq -F_\eta^i\frac{\partial y}{\partial x}, & (F_\eta^i)_y &\simeq F_\eta^i, & (F_\eta^i)_z &\simeq 0 \\
(F_\zeta^i)_x &\simeq -F_\zeta^i\frac{\partial z}{\partial x}, & (F_\zeta^i)_y &\simeq 0, & (F_\zeta^i)_z &\simeq F_\zeta^i
\end{aligned} \tag{2}$$

and similar projections can be obtained with respect to the external fluid forces.

We denote by R_i the inner radius of the internal pipe; the internal fluid occupies a domain with cross-sectional area $A_i = \pi R_i^2$. We also denote R_o and R_e as the outer radius of the internal pipe and the inner radius of the external pipe. In addition, we assign U_i and U_e to be the constant averaged turbulent flow velocities for the internal and external regions.

We will initiate our derivation of the governing equations for $y(x,t)$ and $z(x,t)$ by writing down the force equilibrium for the inner tubular beam, which has flexural rigidity EI, where E is the Young's modulus, and I, expressed as $I = \pi(R_o^4 - R_i^4)/4$, is the moment of inertia of the tubular beam cross-sectional area.

As depicted in Fig. 4, a differential element dx of the beam is acted upon by forces due to gravity g with an inclination angle θ, tension T, fluid forces $(F_\xi^i, F_\eta^i, F_\zeta^i)$ and $(F_\xi^e, F_\eta^e, F_\zeta^e)$, and transverse shear forces (Q_y, Q_z). Following Hannoyer and Paidoussis [7], we will, in the present analysis, discount the influence of any moments that may be exerted by the internal and external flows. Also depicted in Fig. 4 are the bending moments M_y and M_z in accord with $y(x,t)$ and $z(x,t)$. In the standard manner, if we ignore viscoelastic damping effects and assume the beam cross-sectional area to be constant, the bending moments M_y and M_z, and the shear forces Q_y and Q_z assume the form,

$$\begin{aligned} M_y &= EI\frac{\partial^2 y}{\partial x^2}, \quad & Q_y &= -EI\frac{\partial^3 y}{\partial x^3} \\ M_z &= EI\frac{\partial^2 z}{\partial x^2}, \quad & Q_z &= -EI\frac{\partial^3 z}{\partial x^3} \end{aligned} \tag{3}$$

Therefore, the governing equations for the tubular beam may be expressed as

$$\begin{aligned} \frac{\partial T}{\partial x} + \left(F_\xi^i - F_\eta^i\frac{\partial y}{\partial x} - F_\zeta^i\frac{\partial z}{\partial x}\right) + \left(F_\xi^e - F_\eta^e\frac{\partial y}{\partial x} - F_\zeta^e\frac{\partial z}{\partial x}\right) \\ -\frac{\partial}{\partial x}\left(Q_y\frac{\partial y}{\partial x}\right) - \frac{\partial}{\partial x}\left(Q_z\frac{\partial z}{\partial x}\right) - mg\sin\theta = 0 \end{aligned} \tag{4}$$

$$\begin{aligned} \frac{\partial}{\partial x}\left(T\frac{\partial y}{\partial x}\right) + \frac{\partial Q_y}{\partial x} + \left(F_\eta^i + F_\xi^i\frac{\partial y}{\partial x}\right) + \left(F_\eta^e + F_\xi^e\frac{\partial y}{\partial x}\right) \\ = m\frac{\partial^2 y}{\partial t^2} + mg\cos\theta \end{aligned} \tag{5}$$

$$\frac{\partial}{\partial x}\left(T\frac{\partial z}{\partial x}\right) + \frac{\partial Q_z}{\partial x} + \left(F_\zeta^i + F_\xi^i\frac{\partial z}{\partial x}\right) + \left(F_\zeta^e + F_\xi^e\frac{\partial z}{\partial x}\right) = m\frac{\partial^2 z}{\partial t^2} \tag{6}$$

where m denotes the mass per unit length of the tubular beam.

Furthermore, from the force equilibrium for the internal flow (see, for example, Refs. [8] [16] [20]), we can express the internal fluid forces as follows:

$$F_\xi^i - F_\eta^i\frac{\partial y}{\partial x} - F_\zeta^i\frac{\partial z}{\partial x} = -\frac{\partial}{\partial x}(p_iA_i) - \rho_iA_ig\sin\theta \tag{7}$$

$$F_\eta^i + F_\xi^i\frac{\partial y}{\partial x} = -\frac{\partial}{\partial x}\left(p_iA_i\frac{\partial y}{\partial x}\right) - \rho_iA_ig\cos\theta - \rho_iA_i\left(\frac{\partial}{\partial t} + U_i\frac{\partial}{\partial x}\right)^2 y \tag{8}$$

$$F_\zeta^i + F_\xi^i \frac{\partial z}{\partial x} = -\frac{\partial}{\partial x}\left(p_i A_i \frac{\partial z}{\partial x}\right) - \rho_i A_i \left(\frac{\partial}{\partial t} + U_i \frac{\partial}{\partial x}\right)^2 z \tag{9}$$

Finally, we turn our attention to the contributions from the external fluid flow. We treat the external flow a little differently because of the fact that we can no longer directly replace the forces acting on the outer surface of the inner pipe with the equivalent flow pressure, inertia, and gravitational forces. We note that we have two different regions to consider, i.e., the confined region $0 \le x \le L$ and the unconfined region $L < x \le l$. However, due to the outlet opening at the location $x = L$, the hydrostatic pressure is continuous in both regions, and for the tubular beam with a uniform cross-sectional area, the components of the net forces attributable to the external hydrostatic and hydrodynamic fluid pressures are given by

$$\begin{aligned} \mathcal{F}_x^1 &= 0 \\ \mathcal{F}_y^1 &= \rho_e A_o g \cos\theta + \frac{\partial}{\partial x}((p_e + p_o) A_o \frac{\partial y}{\partial x}) \\ \mathcal{F}_z^1 &= \frac{\partial}{\partial x}((p_e + p_o) A_o \frac{\partial z}{\partial x}) \end{aligned} \tag{10}$$

where p_e and p_o stand for the hydrostatic and hydrodynamic pressures, respectively, and the cross-sectional area A_o is defined as πR_o^2. By denoting the free surface level measured from the origin $(0,0,0)$ as y_o, such that the hydrostatic pressure at the tip of the submerged beam $(x = l)$ is given by $\bar{p} = \rho_e g y_o - \rho_e g l \sin\theta$, we obtain the expression for the hydrostatic pressure of the external fluid,

$$p_e = (l - x)\rho_e g \sin\theta - y \rho_e g \cos\theta + \bar{p} \tag{11}$$

Furthermore, according to Refs. [7], [17], and [20], we have the following expression for the hydrodynamic pressure in the concentric flow region,

$$p_o A_o = \frac{1}{2}\rho_e D_o U_e^2 C_f h(x) \tag{12}$$

where

$$h(x) = \begin{cases} \dfrac{D_o}{D_e - D_o}(L - x), & 0 \leq x \leq L \\ 0, & L < x \leq l \end{cases} \tag{13}$$

and, consequently,

$$\frac{dh(x)}{dx} = \begin{cases} -\dfrac{D_o}{D_e - D_o}, & 0 \leq x \leq L \\ 0, & L < x \leq l \end{cases} \tag{14}$$

As discussed in Refs. [7], [14], and [17], the external flow exerts on the tubular beam the following viscous forces per unit length in both the normal (η,ζ) and longitudinal (ξ) directions,

$$\begin{aligned} f_\xi^e &= \frac{1}{2}\rho_e D_o U_e^2 C_f \\ f_\eta^e &= -\frac{1}{2}\rho_e D_o U_e C_f \left(\frac{\partial y}{\partial t} + U_e \frac{\partial y}{\partial x}\right) \\ f_\zeta^e &= -\frac{1}{2}\rho_e D_o U_e C_f \left(\frac{\partial z}{\partial t} + U_e \frac{\partial z}{\partial x}\right) \end{aligned} \tag{15}$$

where D_o is the outer diameter of the inner pipe, and the friction coefficient C_f has, according to Refs. [14], [21], and [22], different values in the confined and unconfined regions,

$$C_f = \begin{cases} C_f^1, & 0 \leq x \leq L \\ C_f^2, & L < x \leq l \end{cases} \tag{16}$$

Turning now to the fluid inertia forces, we take x_o to be the entrance distance associated with the turbulent boundary layer, define the functions $\sigma = 1 + 0.4(x_o/L)C_f^1$ and $\alpha = 0.4C_f^1/\sigma$ for the confined external flow region, and introduce for the components of the inertia forces

$$
\begin{aligned}
\mathcal{F}_x^2 &= 0 \\
\mathcal{F}_y^2 &= -\chi\rho_e A_o\left(\frac{\partial}{\partial t}+\tilde{U}_e\frac{\partial}{\partial x}\right)\left(\frac{\partial}{\partial t}+U_e\frac{\partial}{\partial x}\right)y \\
\mathcal{F}_z^2 &= -\chi\rho_e A_o\left(\frac{\partial}{\partial t}+\tilde{U}_e\frac{\partial}{\partial x}\right)\left(\frac{\partial}{\partial t}+U_e\frac{\partial}{\partial x}\right)z
\end{aligned}
\tag{17}
$$

where

$$
\chi = \begin{cases} \dfrac{R_e^2+R_o^2}{R_e^2-R_o^2}, & 0 \le x \le L \\ 1, & L < x \le l \end{cases}
\tag{18}
$$

and

$$
\bar{U}_e = \begin{cases} U_e(1-\alpha(x/L)^2)/\sigma, & 0 \le x \le L \\ U_e, & L < x \le l \end{cases}
\tag{19}
$$

Therefore, the overall external fluid forces are written as,

$$
F_\xi^e - F_\eta^e\frac{\partial y}{\partial x} - F_\zeta^e\frac{\partial z}{\partial x} = \mathcal{F}_x^1 + \left(f_\xi^e - f_\eta^e\frac{\partial y}{\partial x} - f_\zeta^e\frac{\partial z}{\partial x}\right) + \mathcal{F}_x^2
\tag{20}
$$

$$
F_\eta^e + F_\xi^e\frac{\partial y}{\partial x} = \mathcal{F}_y^1 + \left(f_\eta^e + f_\xi^e\frac{\partial y}{\partial x}\right) + \mathcal{F}_y^2
\tag{21}
$$

$$
F_\zeta^e + F_\xi^e\frac{\partial z}{\partial x} = \mathcal{F}_z^1 + \left(f_\zeta^e + f_\xi^e\frac{\partial z}{\partial x}\right) + \mathcal{F}_z^2
\tag{22}
$$

From this point on, we will ignore, as a consequence of the small displacement and small strain assumptions, all nonlinear terms that appear in the three sets of force balance equations. The key point in simplifying the governing equations (4) to (6) is to obtain the explicit expression for the tension T, based on the assumption $p_i|_{x=l} = \bar{p} - \frac{1}{2}\rho_e D_o^2 U_e^2 C_b/A$, and the axial force equilibrium at the tip of the tubular beam, i.e., $T|_{x=l} = -\bar{p}A + \frac{1}{2}\rho_e D_o^2 U_e^2 C_b$, where A denotes the cross-sectional area of the tubular beam, which is given by $\pi(R_o^2 - R_i^2)$, and C_b is the coefficient representing the base drag. Thus, if the tubular beam density is ρ, the mass per unit length m

can be expressed as ρA. Abbreviating $-\bar{p}A_o + \frac{1}{2}\rho_e D_o^2 U_e^2 C_b \frac{A_o}{A}$ as $\mathcal{G}_0$, $(m+\rho_i A_i) g \sin\theta$ as $\mathcal{G}_1$, and $\frac{1}{2}\rho_e D_o U_e^2$ as $\mathcal{G}_2$, we obtain from Eqs. (4), (20), and (7),

$$\frac{\partial(T - p_i A_i)}{\partial x} = \mathcal{G}_1 - \mathcal{G}_2 C_f \tag{23}$$

so that

$$\begin{aligned} T - p_i A_i &= \mathcal{G}_0 + (x-l)\mathcal{G}_1 + \mathcal{G}_2 \int_x^l C_f dx \\ &= \mathcal{G}_0 + (x-l)\mathcal{G}_1 + \mathcal{G}_2 \begin{cases} C_f^1(L-x) + C_f^2(l-L), & 0 \le x \le L \\ C_f^2(l-x), & L < x \le l \end{cases} \end{aligned} \tag{24}$$

Using, respectively, the sets of equations (5), (8), and (21) and (6), (9), and (22), it is now an easy task to derive the following governing linearized equations:

$$C_1 \frac{\partial^4 y}{\partial x^4} + C_2 \frac{\partial^2 y}{\partial x^2} + C_3 \frac{\partial^2 y}{\partial x \partial t} + C_4 \frac{\partial^2 y}{\partial t^2} + C_5 \frac{\partial y}{\partial x} + C_6 \frac{\partial y}{\partial t} + C_7 = 0 \tag{25}$$

$$D_1 \frac{\partial^4 z}{\partial x^4} + D_2 \frac{\partial^2 z}{\partial x^2} + D_3 \frac{\partial^2 z}{\partial x \partial t} + D_4 \frac{\partial^2 z}{\partial t^2} + D_5 \frac{\partial y}{\partial x} + D_6 \frac{\partial y}{\partial t} + D_7 = 0 \tag{26}$$

where the two sets of coefficients are given by

$$\begin{aligned} C_1 &= EI \\ C_2 &= \rho_i A_i U_i^2 - (T - p_i A_i + p_e A_o + \frac{1}{2}\rho_e D_o U_e^2 C_f h(x)) + \chi \rho_e A_o \bar{U}_e U_e \\ C_3 &= 2\rho_i A_i U_i + \chi \rho_e A_o (U_e + \bar{U}_e) \\ C_4 &= m + \rho_i A_i + \chi \rho_e A_o \\ C_5 &= -(m + \rho_i A_i - \rho_e A_o) g \sin\theta + \frac{1}{2}\rho_e D_o U_e^2 C_f (1 - \frac{dh(x)}{dx}) \\ C_6 &= \frac{1}{2}\rho_e D_o U_e C_f \\ C_7 &= (m + \rho_i A_i - \rho_e A_o) g \cos\theta \end{aligned} \tag{27}$$

and

$$
\begin{aligned}
D_1 &= EI \\
D_2 &= \rho_i A_i U_i^2 - (T - p_i A_i + p_e A_o + \frac{1}{2}\rho_e D_o U_e^2 C_f h(x)) + \chi \rho_e A_o \bar{U}_e U_e \\
D_3 &= 2\rho_i A_i U_i + \chi \rho_e A_o (U_e + \bar{U}_e) \\
D_4 &= m + \rho_i A_i + \chi \rho_e A_o \\
D_5 &= -(m + \rho_i A_i - \rho_e A_o) g \sin\theta + \frac{1}{2}\rho_e D_o U_e^2 C_f (1 - \frac{dh(x)}{dx}) \\
D_6 &= \frac{1}{2}\rho_e D_o U_e C_f \\
D_7 &= 0
\end{aligned}
\tag{28}
$$

Remark I: For the clamped (or built-in) boundary condition at $x = 0$, we have

$$
\begin{aligned}
y(0,t) &= 0, \quad \frac{\partial y(0,t)}{\partial x} = 0 \\
z(0,t) &= 0, \quad \frac{\partial z(0,t)}{\partial x} = 0
\end{aligned}
\tag{29}
$$

while for the free end of the tubular beam at $x = l$, we have

$$
\begin{aligned}
\frac{\partial^2 y(l,t)}{\partial x^2} &= 0, \quad EI\frac{\partial^3 y(l,t)}{\partial x^3} + (\bar{p}A - \frac{1}{2}\rho_e D_o^2 U_e^2 C_b)\frac{\partial y(l,t)}{\partial x} = 0 \\
\frac{\partial^2 z(l,t)}{\partial x^2} &= 0, \quad EI\frac{\partial^3 z(l,t)}{\partial x^3} + (\bar{p}A - \frac{1}{2}\rho_e D_o^2 U_e^2 C_b)\frac{\partial z(l,t)}{\partial x} = 0
\end{aligned}
\tag{30}
$$

Remark II: We recognize that the coefficients C_2 to C_6 and D_2 to D_6 are variables depending on the position x. To circumvent the discontinuity at the location $x = L$, where the confined and unconfined domains are separated, we prescribe a nodal point at that location.

Remark III: By neglecting nonlinear terms, the governing equations for $y(x,t)$ and $z(x,t)$ turn out to be decoupled. In addition, we notice that the only difference between Eqs. (25) and (26) occurs in the inhomogeneous terms C_7 and D_7. However, such a difference will not affect the linear stability analysis based on the characteristic equations. Therefore, from here on, we will deal exclusively with Eq. (25).

Remark IV: With the small displacement and small strain assumptions, by ignoring the contribution of the term involving y, we may rewrite the expression for the hydrostatic pressure of the external fluid Eq. (11) as

$$p_e \simeq (l - x)\rho_e g \sin\theta + \bar{p} \tag{31}$$

3 Numerical Analysis

We employ the method of finite differences to replace the partial differential equation (25) with a set of ordinary differential equations with respect to time. Equivalent difference schemes are also used for the boundary conditions in Eqs. (29) and (30). We define the solution variable $y(x,t)$ at the spatial grid (or nodal) point i as $Y^i(t)$ (depicted in Fig. 5), and its corresponding time derivative as $\dot{Y}^i(t)$. Using an equal spacing h between finite difference stations, we obtain the following finite difference approximation for various differentiations:

$$\begin{aligned}
\left.\frac{\partial y}{\partial x}\right|_i &= \frac{Y^{i+1} - Y^{i-1}}{2h} \\
\left.\frac{\partial^2 y}{\partial x^2}\right|_i &= \frac{Y^{i+1} - 2Y^i + Y^{i-1}}{h^2} \\
\left.\frac{\partial^4 y}{\partial x^4}\right|_i &= \frac{Y^{i+2} - 4Y^{i+1} + 6Y^i - 4Y^{i-1} + Y^{i-2}}{h^4}
\end{aligned} \tag{32}$$

In addition, by employing the same finite difference procedure, we obtain from the boundary conditions in Eqs. (29) and (30)

$$\begin{aligned}
Y^0 &= 0 \\
Y^{-1} &= Y^1 \\
Y^{N+1} &= 2Y^N - Y^{N-1} \\
Y^{N+2} &= (4 - \frac{(2\bar{p}A - \rho_e D_o^2 U_e^2 C_b)h^2}{EI})(Y^N - Y^{N-1}) + Y^{N-2}
\end{aligned} \tag{33}$$

Therefore, the discretized characteristic equation based on the equilibrium equation (25) can be written as follows:

node i $(1 \leq i \leq N)$:

$$C_4^i \ddot{Y}^i + \frac{C_3^i}{2h}\dot{Y}^{i+1} + C_6^i \dot{Y}^i - \frac{C_3^i}{2h}\dot{Y}^{i-1} + \frac{C_1^i}{h^4}Y^{i+2} + (\frac{C_2^i}{h^2} - \frac{4C_1^i}{h^4} + \frac{C_5^i}{2h})Y^{i+1} + \\ (\frac{6C_1^i}{h^4} - \frac{2C_2^i}{h^2})Y^i + (\frac{C_2^i}{h^2} - \frac{4C_1^i}{h^4} - \frac{C_5^i}{2h})Y^{i-1} + \frac{C_1^i}{h^4}Y^{i-2} = 0 \tag{34}$$

Note that the variable coefficients C_1 to C_6 in Eq. (27) are functions of x and are denoted as C_1^i to C_6^i at the nodal point i. Moreover, substituting Eq. (33) in Eq. (34) gives,

$$\mathbf{M}\ddot{\mathbf{Y}} + \mathbf{C}\dot{\mathbf{Y}} + \mathbf{K}\mathbf{Y} = \mathbf{0} \tag{35}$$

where $\mathbf{Y}$ is the solution vector, and $\mathbf{M}$, $\mathbf{C}$, and $\mathbf{K}$ stand for the mass, damping (including gyroscopic terms), and stiffness algebraic coefficient matrices, respectively.

Having the set of second-order ordinary differential equations in Eq. (35), we can then assume a characteristic solution $\mathbf{Y} = e^{iwt}\widehat{\mathbf{Y}}$, where $\widehat{\mathbf{Y}}$ is the modeshape corresponding to the natural frequency $\omega = 2\pi f$, and employ standard eigenvalue solution techniques.

4 Results

To find the frequency range of a particular pipe system design, we use the following physical parameters: $\rho_i = \rho_e = 1000$ kg/m^3; $\rho = 7800$ kg/m^3; $l = 2.392$ m; $L = 1.135$ m; $x_o = 2.4$ m; $y_o = 6.155$ m; $R_i = 0.1165$ m; $R_o = 0.1397$ m; $R_e = 0.2096$ m; $g = 9.8$ m/s^2; $C_f^1 = 0.004\pi$; $C_f^2 = 0.5\pi R_i/l$; $C_b = 0.0125\pi$; $E = 200$ GPa; $U_i = 2$ m/s; and $U_e = 1$ m/s. In order to evaluate the friction coefficients, we need to calculate the Reynolds number defined as $Re = \frac{ua}{\nu}$, where a is a characteristic length, such as one of the pipe diameters in this case; u is a characteristic flow velocity, such as U_i and U_e; and ν stands for the kinematic viscosity; in this work, we use $\nu = 1.13226 \times 10^{-6}$ m^2/s.

For the particular configuration described above, we find that

$$f_1 = 0.5280 \text{ Hz}, \qquad f_2 = 2.696 \text{ Hz}, \qquad f_3 = 7.603 \text{ Hz}$$

Because the first three natural frequencies of the inner tubular pipe are very small, they should be eliminated if possible in the silo pipe system design. We conjecture that such low frequency variations will show up as consistency or pressure fluctuations in the stock delivered to the paper forming area.

To come up with critical design criteria concerning the tubular dynamical instability, we need to vary the pipe lengths, inclination angle, free surface level, flow velocities, and pipe radii. We will hold in this paper, as it is done in practice, the volume flow rates constant, i.e., 8.5277×10^{-2} m^3/s for the internal flow, and 7.6705×10^{-2} m^3/s for the external flow. In other words, if we reduce the inner pipe radius, the inner fluid flow velocity will increase accordingly, and vice versa. The same is true for the outer pipe. In addition, with a constant free surface level, the external hydrostatic pressure p_e will vary in accordance with the inner pipe length and the inclination angle. Finally, we vary y_o which governs the depth of the immersed pipe system. However, we recognize that such a design parameter y_o is often related to the fan pump pressure drop and, in practice, cannot be modified easily.

Figure 6 shows the first two frequencies f_1 and f_2 for various outer pipe lengths. As can be seen, the longer the outer pipe, the more susceptible the inner pipe is to buckling or flutter. In Fig. 7, we observe that varying the inner pipe length has a similar, however, much stronger effect on the natural frequencies. Figures 6 and 7 also show that the natural frequencies for the given design configuration with different pipe lengths are between the lower and upper bounds calculated for the two cases in which the inner and outer pipes have the same lengths of l and L, respectively.

Figures 8 and 9 demonstrate that the inclination angle and the depth of the submerged pipe system do not significantly influence the characteristic behavior of the tubular beam. Concerning the inner pipe radius, Figure 10 shows that for the constant volume flow rates that have been assumed, there exists an optimal radius (around 0.16 m in this case). It is also clearly indicated in Fig. 11 that the larger the outer pipe diameter for the constant volume flow rates, the less susceptible the inner pipe is to buckling or flutter.

In addition, to further assist in the design of a pipe system, Figures 12 and 13 present the first two frequencies f_1 and f_2 as functions of the relative difference of outer and inner pipe length $(l - L)/l$ and radius $(R_e - R_o)/R_e$ at various outer pipe lengths l and radii R_e, respectively.

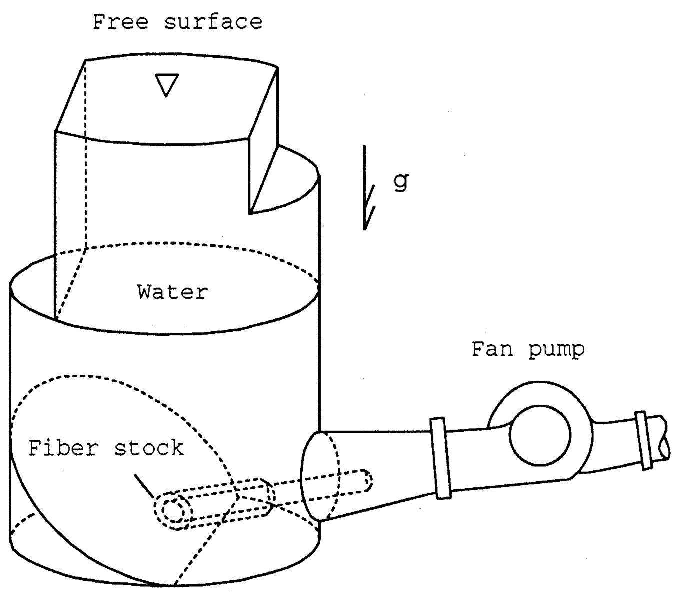

Figure 1: Location of the mixing pipe in the silo unit.

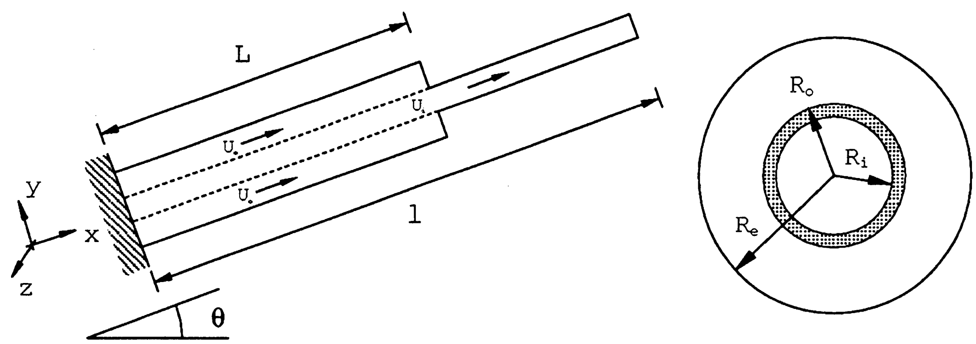

Figure 2: The concentric piping equilibrium configuration.

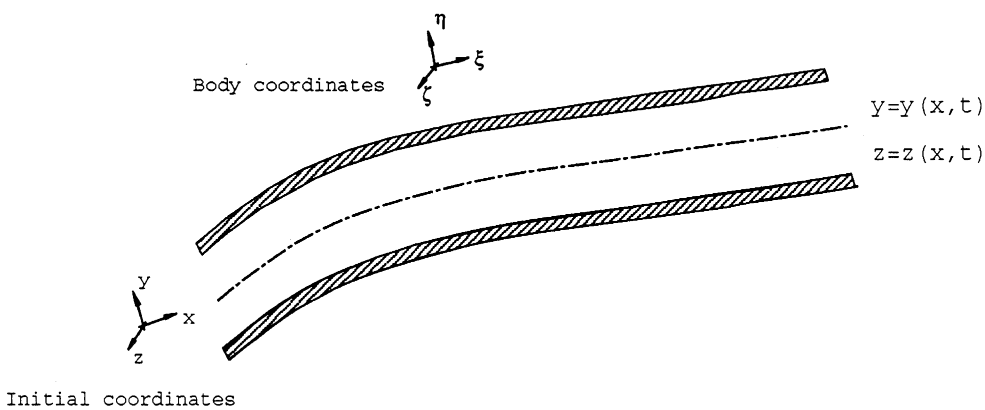

Figure 3: Deformed element of the inner tubular beam.

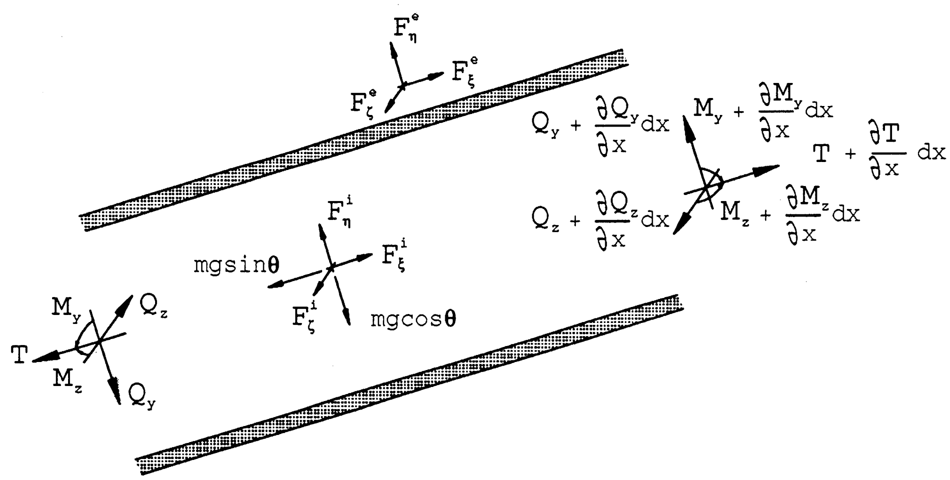

Figure 4: Forces acting on an differential element of the inner tubular beam.

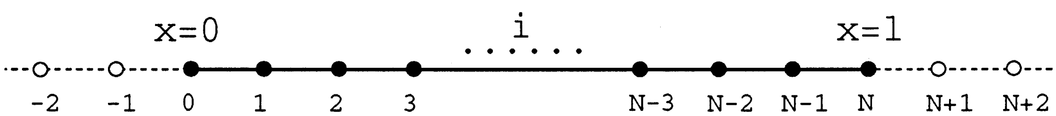

Figure 5: Finite difference stations on the tubular beam.

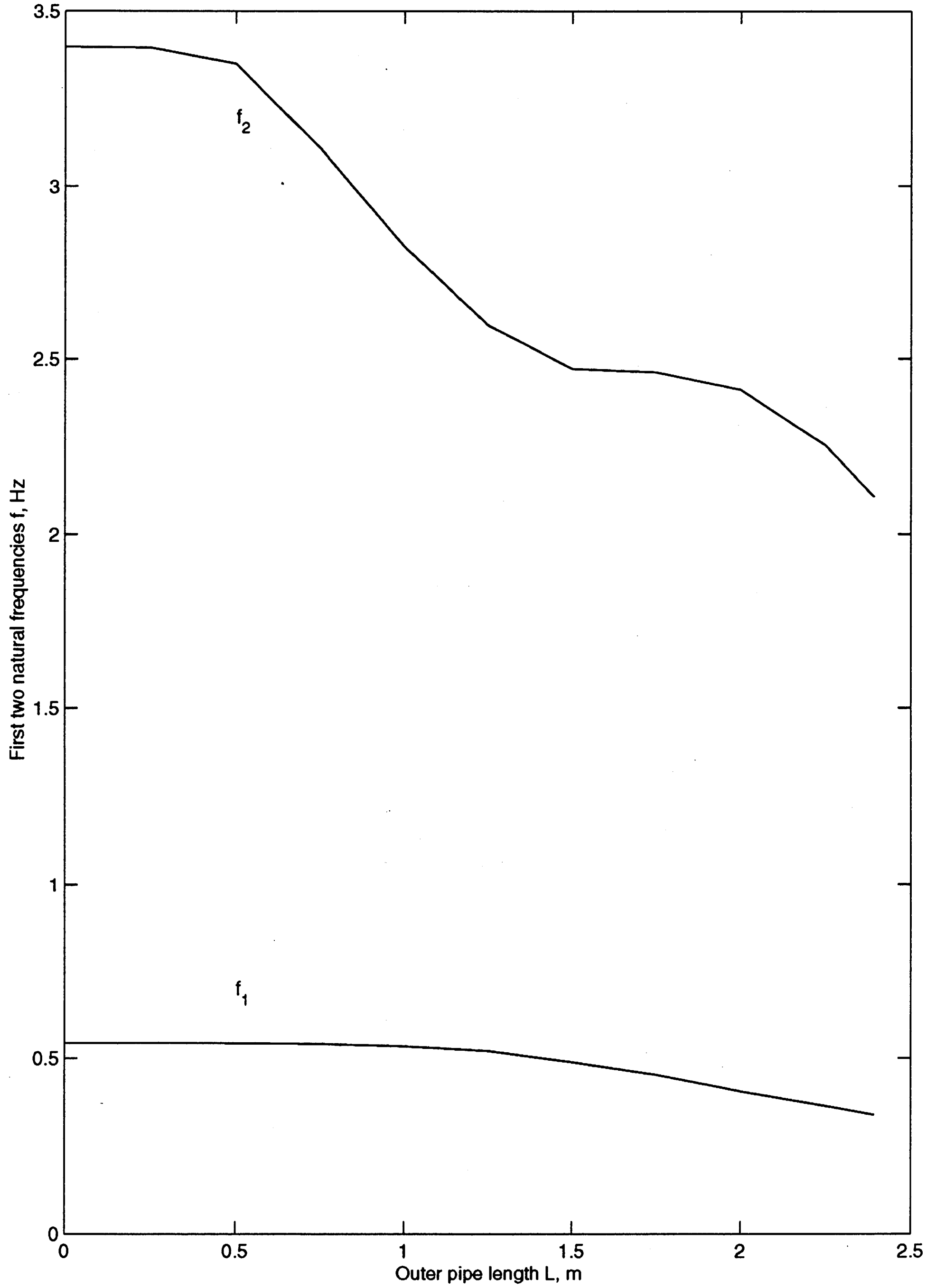

Figure 6: First two natural frequencies *vs.* the outer pipe length L. (Forty-two grid points.)

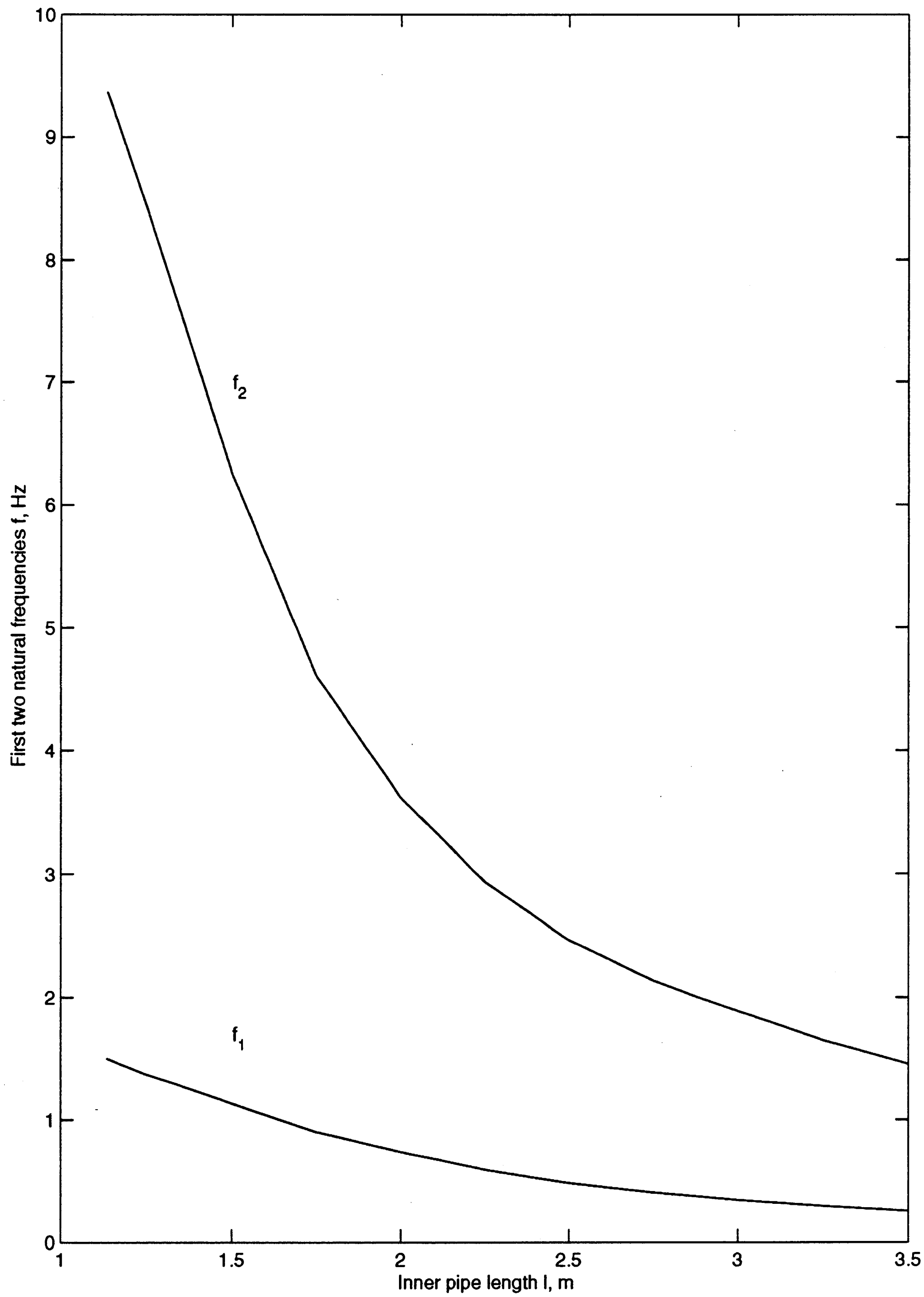

Figure 7: First two natural frequencies *vs.* the inner pipe length l. (Forty-two grid points.)

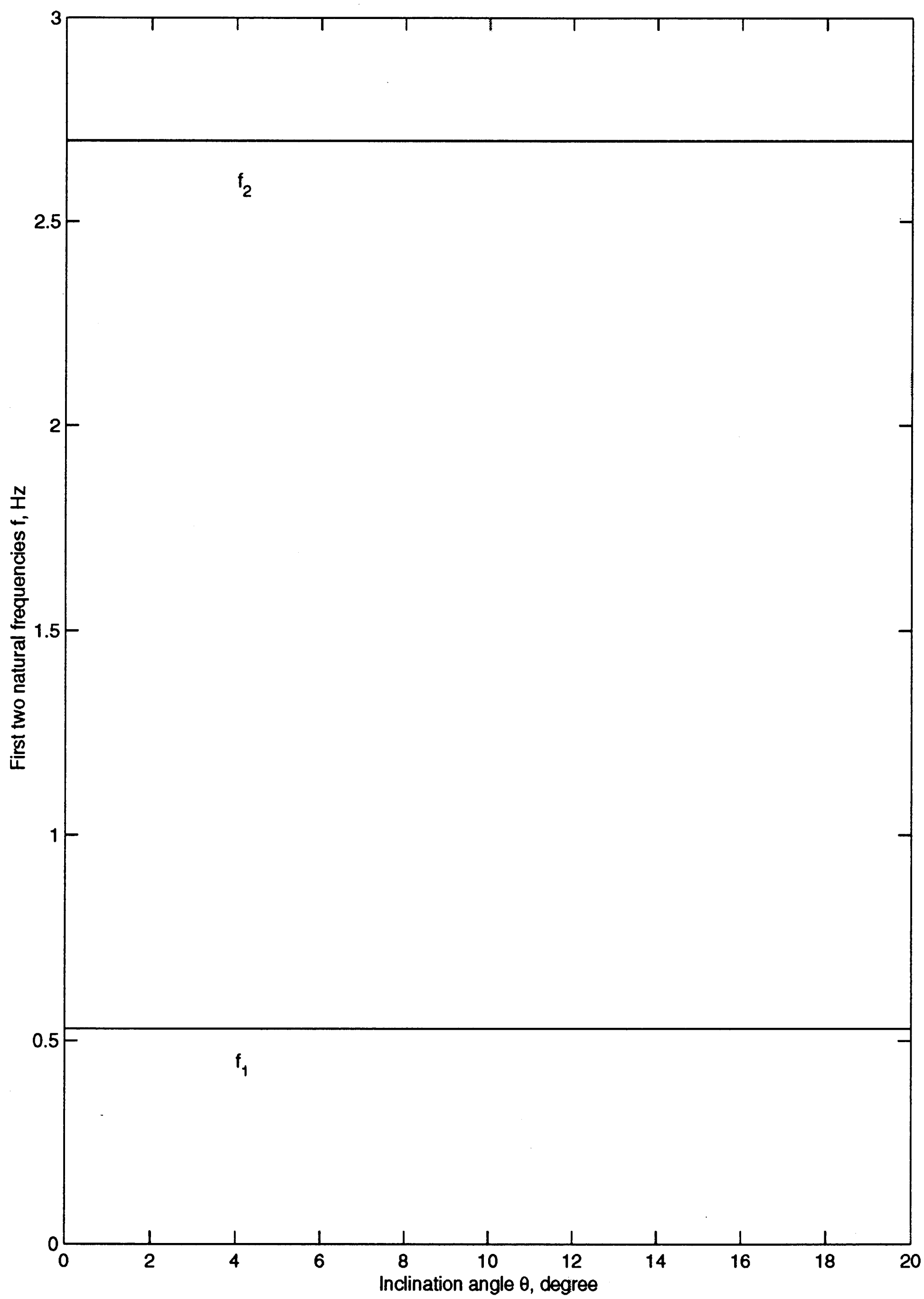

Figure 8: First two natural frequencies *vs.* the inclination angle θ. (Forty-two grid points.)

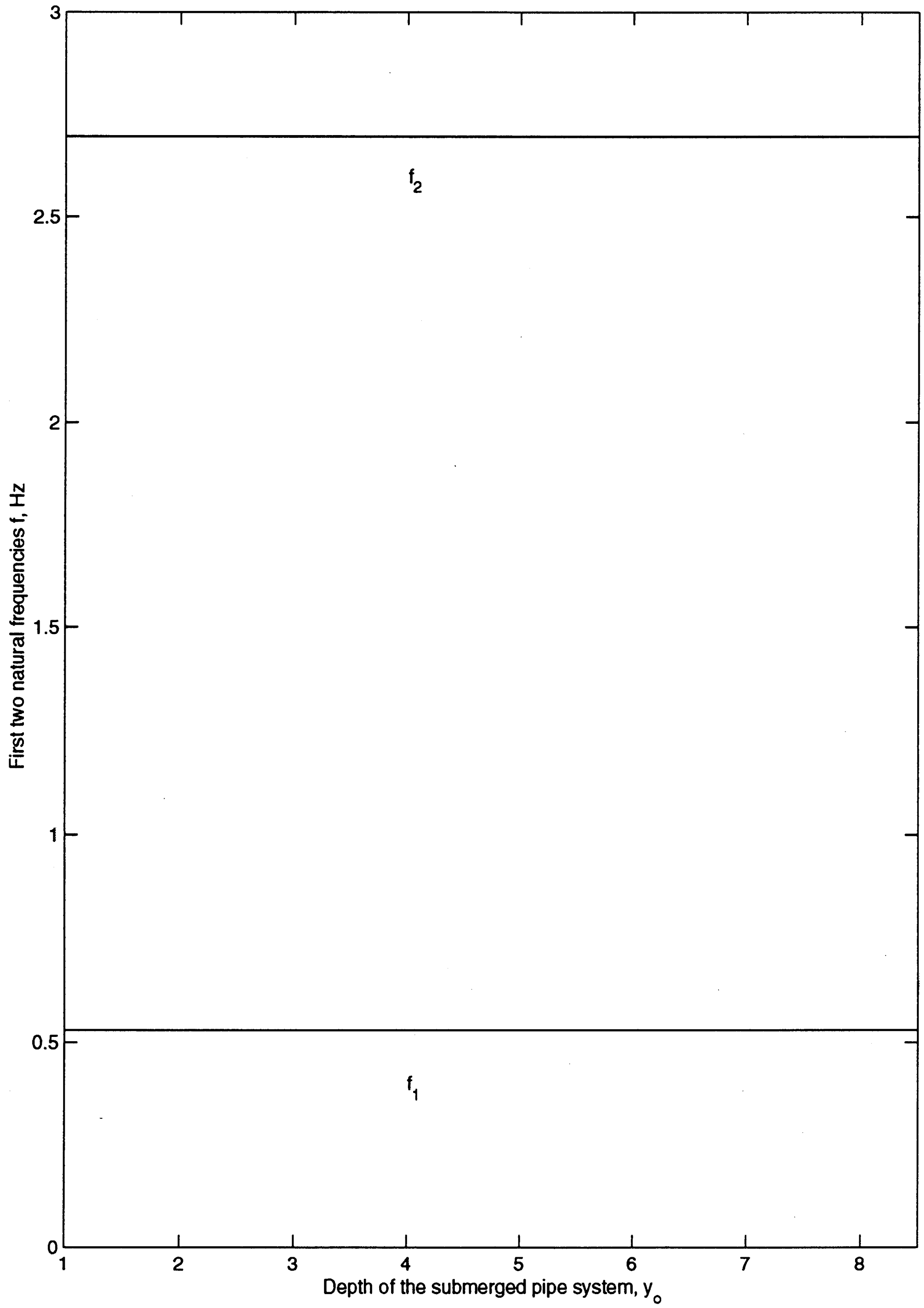

Figure 9: First two natural frequencies *vs.* the depth of the submerged pipe system y_o. (Forty-two grid points.)

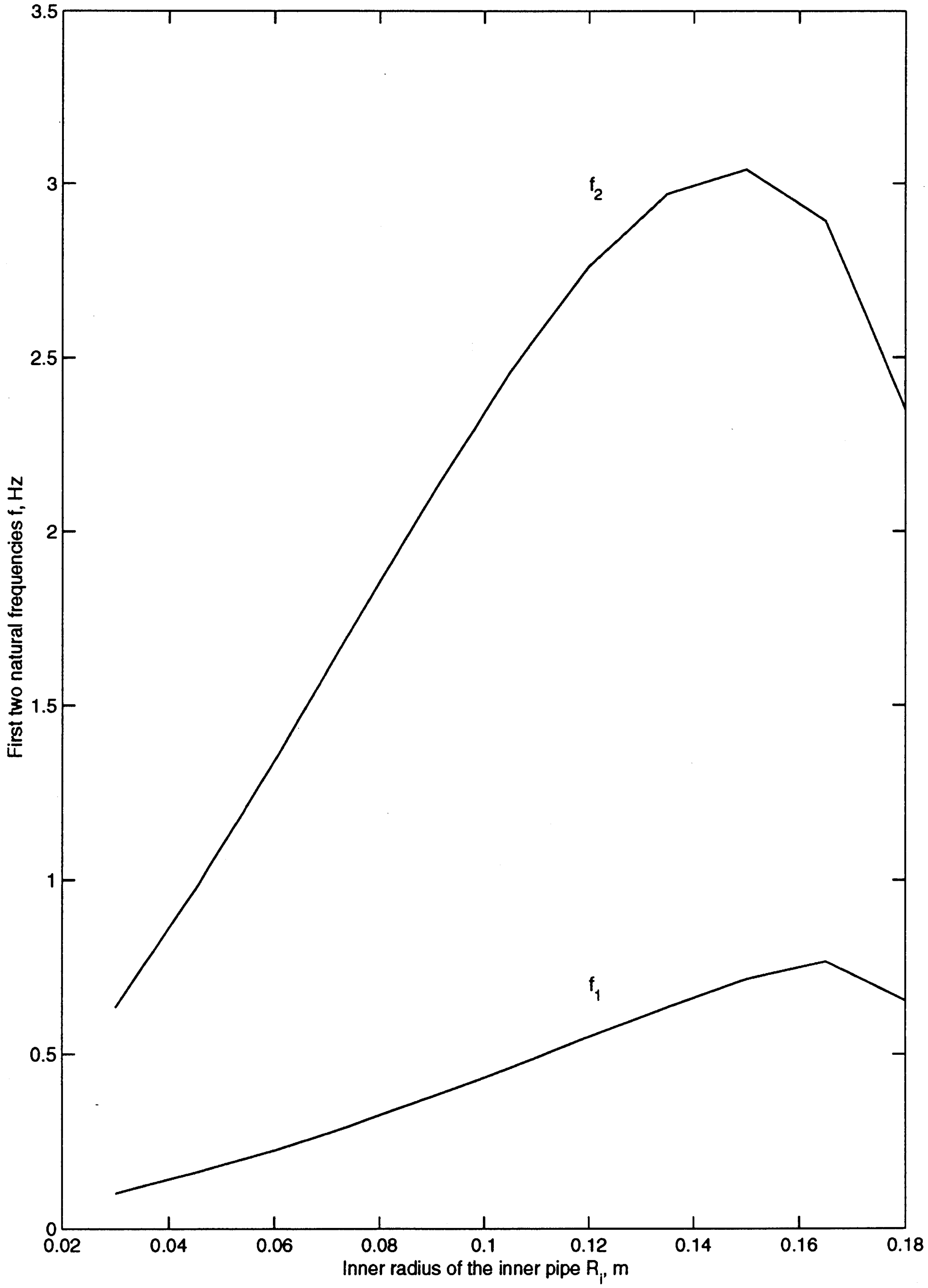

Figure 10: First two natural frequencies *vs.* the inner radius of the inner pipe R_i. (Forty-two grid points.)

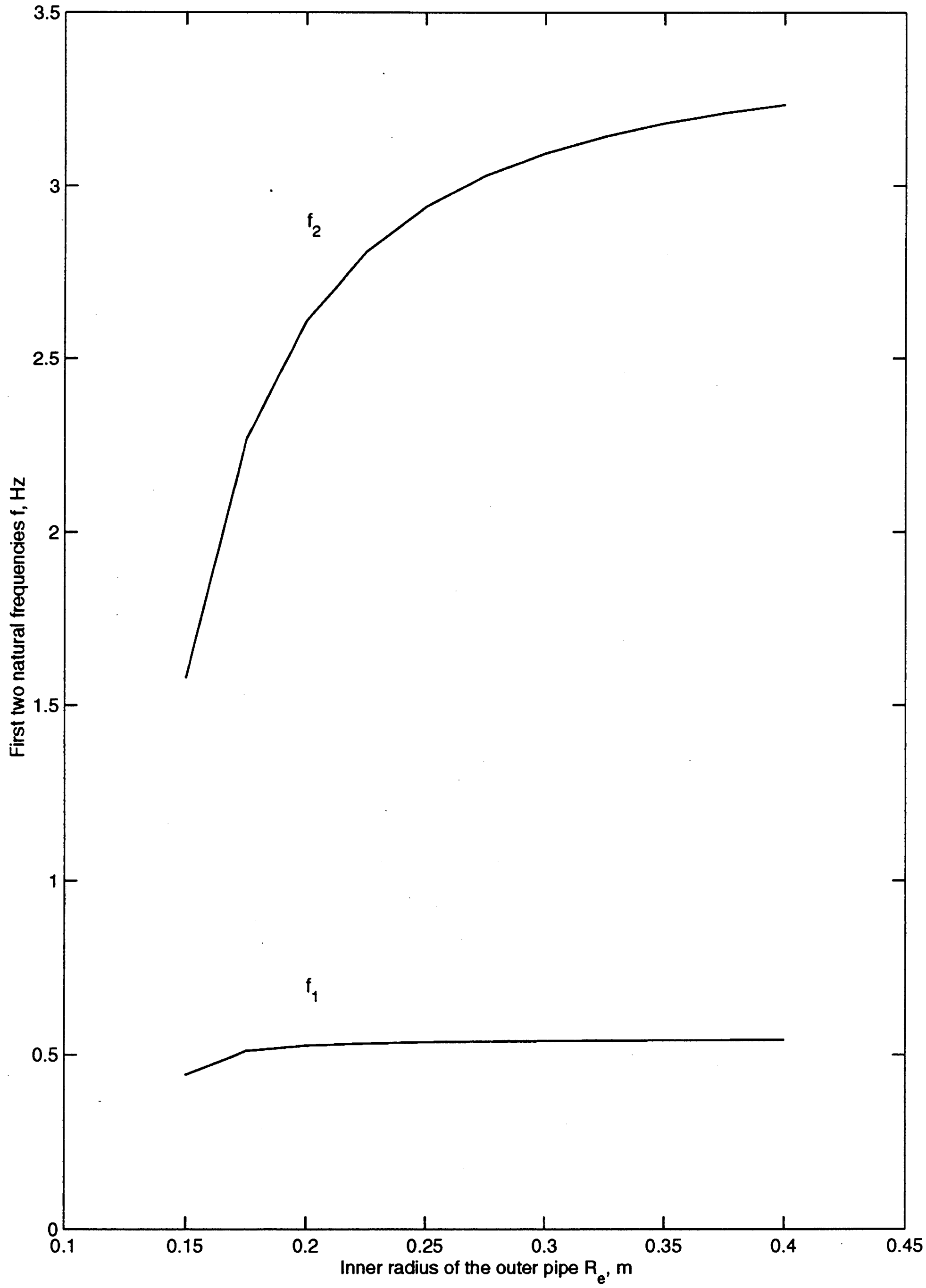

Figure 11: First two natural frequencies *vs.* the inner radius of the outer pipe R_e. (Forty-two grid points.)

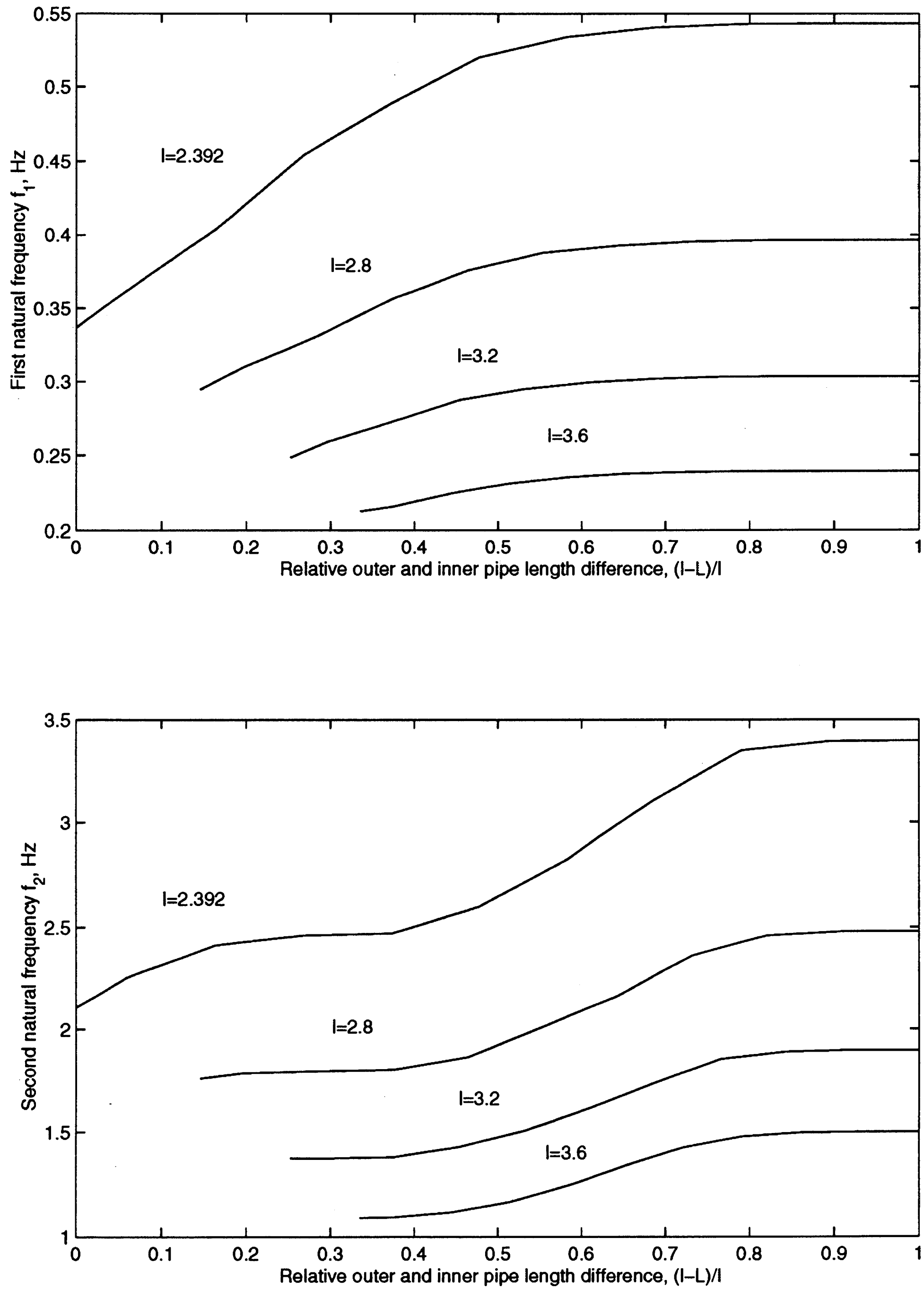

Figure 12: First two natural frequencies vs. relative outer and inner pipe length difference $(l - L)/l$.

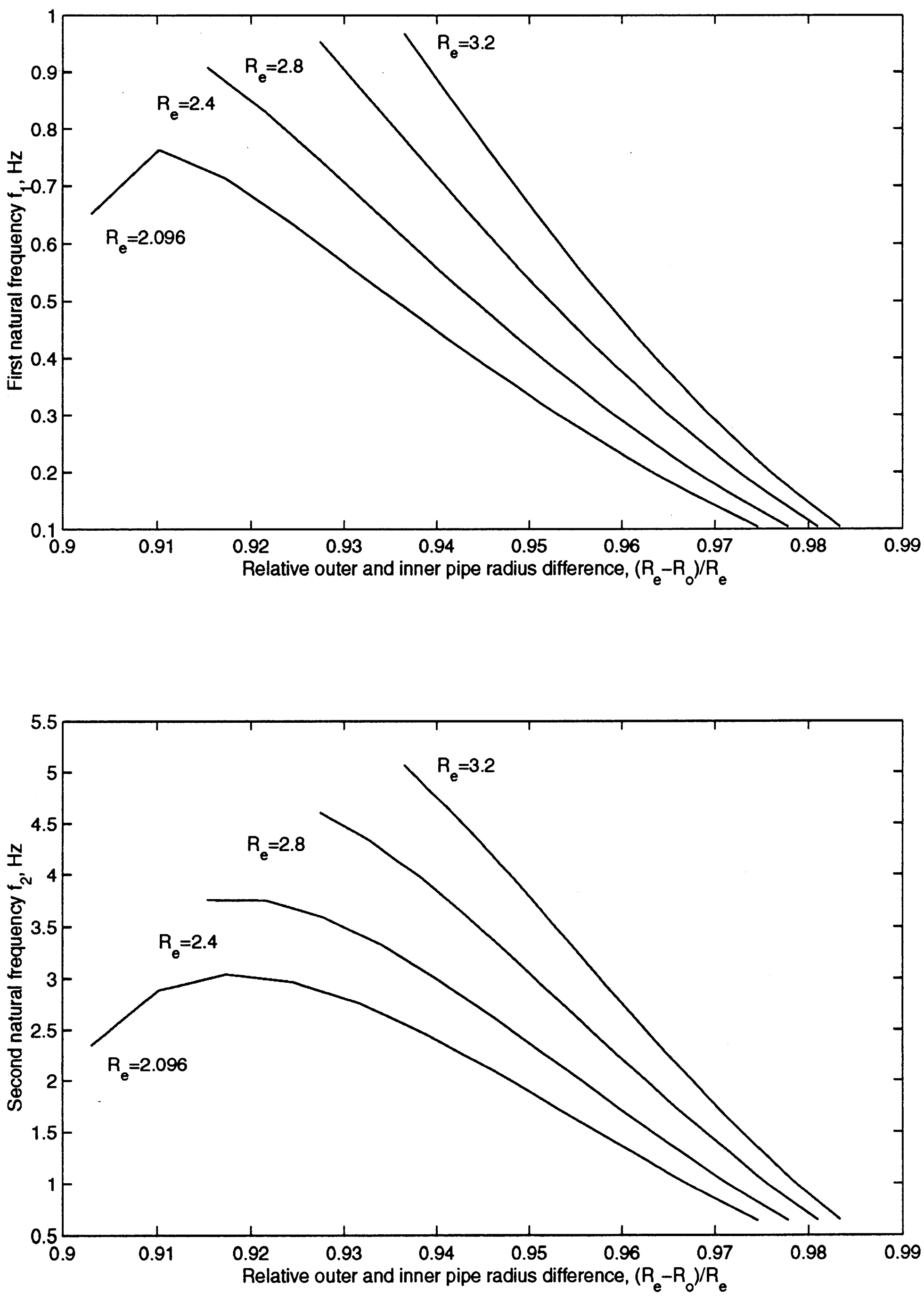

Figure 13: First two natural frequencies vs. relative outer and inner pipe radius difference $(R_e - R_o)/R_e$.

5 Conclusion

The main contribution of this paper is the formulation of a mathematical model for a submerged concentric pipe system with both unconfined and confined external flows. With the implemented finite difference scheme, we have calculated the natural frequency range for a given pipe system configuration, and have shown that such a configuration produces low frequency oscillations around 1 Hz. Although, in practice, due to the existence of a pressure pulsation attenuator and other low pass filters, high frequency variations can be effectively reduced, the predicted natural frequencies of the inner tubular pipe carrying thick stock are dangerously low and need to be avoided in the silo pipe system design. Three conceivable measures are recommended, i.e., reducing the pipe mass per unit length, increasing the pipe flexural rigidity EI, and introducing various supports.

In addition, by varying different design parameters, we conclude:

(1) By decreasing the inner or outer pipe lengths, we can increase the natural frequencies; however, changing the inner pipe length is more effective.

(2) The inclination angle, the depth of the submerged pipe system, and gravity are not important design parameters as far as the pipe stability is concerned.

(3) For a piping system with fixed volume flow rates, there exists an optimal inner pipe radius.

(4) In general, the larger the outer pipe radius, the more stable the suspended pipe system will be. Nevertheless, as the outer pipe radius increases, the inner pipe vibration model approaches that of the case of a singular flexible pipe immersed in an unconfined fluid.

The mathematical model presented in this paper clearly shows much promise in achieving a proper design for a silo piping system.

References

[1] R. Aithal and G.S. Gipson. Instability of internally damped curved pipes. *Journal Eng. Mechanics*, 116:77–90, 1990.

[2] T.B. Benjamin. Dynamics of a system of articulated pipes conveying fluid I. Theory. *Proceedings of the Royal Society, Series A*, 261:457–486, 1961.

[3] T.B. Benjamin. Dynamics of a system of articulated pipes conveying fluid II. Experiments. *Proceedings of the Royal Society, Series A*, 261:487–499, 1961.

[4] S.S. Chen. Vibrations of flow-induced structural vibrations. In *IUTAM-IAHR Symposium Proceedings*, pages 663–675. Springer-Verlag, N.Y., 1974.

[5] C. Dupuis and J. Rousselet. The equations of motion of curved pipes conveying fluid. *Journal of Sound and Vibration*, 153(3):473–489, 1992.

[6] R.W. Gregory and M.P. Paidoussis. Unstable oscillation of tubular cantilevers conveying fluid I. theory. *Proceedings of the Royal Society, Series A*, 293:512–527, 1966.

[7] M.J. Hannoyer and M.P. Paidoussis. Instabilities of tubular beams simultaneously subjected to internal and external axial flows. *ASME Journal of Mechanical Design*, 100:328–336, 1978.

[8] M.J. Hannoyer and M.P. Paidoussis. Dynamics of slender tapered beams with internal or external axial flow. Part I: Theory. *Journal of Applied Mechanics*, 46:45–51, 1979.

[9] B.E. Laithier and M.P. Paidoussis. The equations of motion of initially stressed timoshenko tubular beams conveying fluid. *Journal of Sound and Vibration*, 79(2):175–195, 1981.

[10] Y.-H. Lin and C.-L. Chu. Active flutter control of a cantilever tube conveying fluid using piezoelectric actuators. *Journal of Sound and Vibration*, 196(1):97–105, 1996.

[11] T.S. Lundgren, R.R. Sethna, and A.K. Bajaj. Stability boundaries for flow induced motions of tubes with an inclined terminal nozzle. *Journal of Sound and Vibration*, 64:553–571, 1979.

[12] A.K. Misra, M.P. Paidoussis, and K.S. Van. On the dynamics of curved pipes transporting fluid. Part I: Inextensible theory. *Journal of Fluids and Structures*, 2:221–244, 1988.

[13] V.B. Nguyen, M.P. Paidoussis, and A.K. Misra. An experimental study of the stability of cantilevered coaxial cylindrical shells conveying fluid. *Journal of Fluids and Structures*, 7:913–930, 1993.

[14] M.P. Paidoussis. Dynamics of flexible slender cylinders in axial flow. Part 1. Theory. *Journal of Fluid Mechanics*, 26:717–736, 1966.

[15] M.P. Paidoussis. Dynamics of flexible slender cylinders in axial flow. Part 2. Experiments. *Journal of Fluid Mechanics*, 26:737–751, 1966.

[16] M.P. Paidoussis. Dynamics of tubular cantilevers conveying fluid. *Journal of Mechanical Engineering Science*, 12(2):85–103, 1970.

[17] M.P. Paidoussis. Dynamics of cylindrical structures subjected to axial flow. *Journal of Sound and Vibration*, 29(3):365–385, 1973.

[18] M.P. Paidoussis and N.T. Issid. Dynamic stability of pipes conveying fluid. *Journal of Sound and Vibration*, 33(3):267–294, 1974.

[19] M.P. Paidoussis, A.K. Misra, and V.B. Nguyen. Internal and annular-flow-induced instabilities of a clamped-clamped or cantilevered cylindrical shell in a coaxial conduit: The effects of system parameters. *Journal of Sound and Vibration*, 159(2):193–205, 1992.

[20] M.P. Paidoussis and M.J. Pettigrew. Dynamics of flexible cylinders in axisymetrically confined axial flow. *Journal of Applied Mechanics*, 46:37–44, 1979.

[21] H. Schlichting. *Boundary-Layer Theory.* McGraw-Hill, seventh edition, 1987.

[22] G. Taylor. Analysis of the swimming of long and narrow animals. *Proceedings of the Royal Society, Series A*, 214:158–183, 1952.

[23] X. Wang. On the research area of approach pipe systems. *IPST PAC Report*, pages 277–334, 1996.

Single Jet Mixing at Arbitrary Angle in Turbulent Tube Flow

by

Zhigang Feng, Xiaodong Wang, Larry J. Forney

1 Introduction

The problem of mixing two fluid streams by turbulent jet injection into the pipeline has various applications in areas such as chemical reactions, heat transfer operations, and mixing and combustion processes in industry. As a simple but effective method to mix two fluids, pipeline mixers have been studied extensively. The first systematic study was conducted by Chilton and Genereaux [1], in which smoke visualization techniques were used to determine optimum mixing condition at a glass tee. Forney and Kwon [3] proposed a similarity law, which was derived from approximate solutions to the equations of motion for the case of a single, fully developed turbulent jet issuing normally to the flow. Forney and Lee [4] further established the importance of the diameter and velocity ratio for geometrically similar flows. Maruyama et al. [8] [9] studied the jet injection of fluid into the pipeline over several pipe diameters from the injection point, and they proposed the standard deviation as a mixing quality indicator. Ger and Holley [5] and Fitzgerald and Holley [2] conducted some experiments and compared standard deviations of measured tracer concentrations far downstream from the side tee. Sroka and Forney [10] derived a scaling law for the second moment of the tracer concentration within the pipeline when the turbulent jet injection is normal to the pipeline.

However, most of the research has been conducted for a configuration in which the jet is normal to the pipeline. In the present study, we consider a more general case in which the turbulence jet injects fluid at an angle θ_o ($0^o < \theta_o < 180^o$), and we derive asymptotic solutions for both jet trajectory and tracer concentration profiles in the near region of the jet injection point. The proposed analytical solutions will be compared with the existing experimental results for turbulent mixing of two fluid streams at an oblique branch [8] [9] and the analytical solutions for T-junctions [3].

Although in chemical engineering it is desirable to have the side-issued jet contact the opposite wall in order to enhance rapid mixing, in the paper industry, the tracer jet is often issued at an angle θ_o ($45^o \leq \theta_o \leq 60^o$) to avoid contact with the opposite wall and, in this way, to minimize flow disturbance and pressure pulsation. The presented analytical solution of the tracer jet trajectory will provide valuable information on the conditions under which the tracer jet will contact the opposite wall.

2 Jet Injection at an Arbitrary Angle

2.1 Theory

The configuration of a general pipeline mixer with an angle θ_o is shown in Fig. 1, in which a jet with diameter d (or radius $b_o = d/2$) issues fluid containing tracer into a tube of diameter D. The ambient fluid velocity of the tube is v, and the initial tracer jet velocity is u_o. The phenomenon of jet mixing of a tracer in turbulent tube flow involves two phases. In the initial stage, the mixing process is dominated by self-induced jet turbulence. After a distance, the jet evolves into a geometrically centered jet, and the mixing of the tracer is dominated by turbulence in the main stream. Forney and Kwon [3] proposed a characteristic length l_m, which represents the distance over which the jet travels before it bends over in the cross flow. This

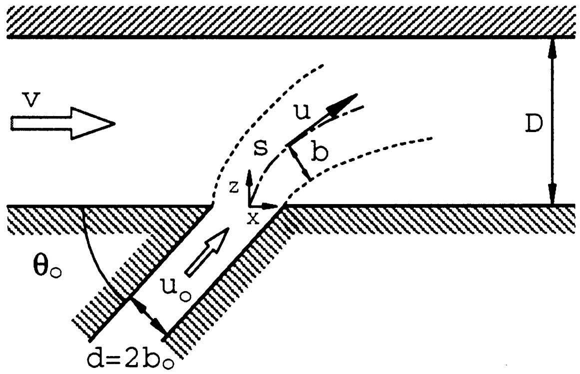

Figure 1: Two fluid streams mixing at an oblique branch.

momentum length is defined as follows:

$$l_m = \frac{du_o \sin\theta_o}{v} \quad (1)$$

For convenience, we also introduce the following dimensionless length:

$$R = \frac{l_m/\sin\theta_o}{d} = \frac{u_o}{v} \quad (2)$$

2.2 Field Equations

Our goal is to derive an asymptotic expression for the jet trajectory at the first stage, i.e., close to the jet orifice. The governing equations for the present problem include the conservation of mass and momentum. The well-known entrainment model first developed by Hoult, Fay, and Forney [6] is employed in this paper. The model assumes that there are two additive entrainment mechanisms, one is due to the tangential difference between the local jet velocity u and ambient fluid velocity component parallel to the jet, and the other to the ambient fluid velocity normal to the jet. For the configuration in Fig. 1, we can write the conservation of mass as follows:

$$\frac{1}{2b}\frac{d}{ds}(b^2u) = \alpha(u - v\cos\theta) + \beta v\sin\theta \tag{3}$$

where s, θ, u, b, α, and β stand for the mixing jet's arc length, tangential angle, jet velocity, equivalent cross-sectional radius, and the tangential and normal entrainment parameters, respectively.

The conservation of tangential momentum can be written as:

$$\frac{d}{ds}(b^2u^2) = v\cos\theta\frac{d}{ds}(b^2u) \tag{4}$$

and similarly for the normal momentum, we have

$$b^2u^2\frac{d\theta}{ds} = -v\sin\theta\frac{d}{ds}(b^2u) \tag{5}$$

The conservation of tracer concentration c gives

$$\frac{d}{ds}(cb^2u) = 0 \tag{6}$$

The boundary conditions at the jet orifice are specified as:

$$s = 0, \quad \theta = \theta_o, \quad u = u_o, \quad b = b_o, \quad c = c_o$$

2.3 Asymptotic Solutions

Because we are interested in an asymptotic expression for the jet trajectory close to the orifice, we assume that the departure of θ from θ_o is small; furthermore, the Reynolds number of the orifice is restricted to large values to ensure jet turbulence, and the effect of buoyancy is neglected. Under these assumptions, from Eq. (3), we have

$$\frac{b^2 u}{b_o^2 u_o} \simeq 1 + 4\Omega \frac{s}{d} \tag{7}$$

in which Ω is a constant given by

$$\Omega = \alpha(1 - \frac{\cos\theta_o}{R}) + \beta\frac{\sin\theta_o}{R} \tag{8}$$

and from Eqs. (4) and (5), we obtain

$$\frac{b^2 u^2}{b_o^2 u_o^2} = \frac{\sin\theta_o}{\sin\theta} \tag{9}$$

Furthermore, Eqs. (5) and (9) give us

$$R\frac{d\theta}{ds} = -\frac{\sin^2\theta}{\sin\theta_o}\frac{d}{ds}(\frac{ub^2}{u_o b_o^2}) \tag{10}$$

By integrating Eq. (10), we have, within the first-order approximation,

$$\theta \simeq \theta_o - 4\Omega\sin^2\theta_o\frac{s}{l_m} \tag{11}$$

and consequently, by nature of Eq. (6), we obtain

$$\frac{c}{c_o} = \frac{1}{1 + 4\Omega s/d} \tag{12}$$

To convert the above expression into cartesian coordinate (x, z), we introduce the following relations:

$$dz = ds\sin\theta = ds\sin(\theta_o + \delta\theta) \simeq ds(\sin\theta_o + \cos\theta_o\delta\theta) \tag{13}$$

$$dx = ds\cos\theta = ds\cos(\theta_o + \delta\theta) \simeq ds(\cos\theta_o - \sin\theta_o\delta\theta) \tag{14}$$

For the region near the orifice, we have

$$\delta\theta = \theta - \theta_o \simeq -4\Omega \sin^2\theta_o \frac{s}{l_m} \tag{15}$$

Integrating Eqs. (13) and (14), we obtain the following two key parametric equations for the asymptotic jet trajectory:

$$z = s\sin\theta_o - \Omega\sin\theta_o\sin 2\theta_o s^2/l_m \tag{16}$$

$$x = s\cos\theta_o + 2\Omega\sin^3\theta_o s^2/l_m \tag{17}$$

Furthermore, the trace trajectory is given implicitly by the following relation:

$$x^2\cos^2\theta_o + xz\sin 2\theta_o + z^2\sin^2\theta_o - \frac{l_m}{2\Omega\sin^2\theta_o}(x\sin\theta_o - z\cos\theta_o) = 0 \tag{18}$$

while the tracer concentration profile, in cartesian coordinates, becomes

$$\frac{c}{c_o} = \frac{1}{1 + R(\sqrt{\cos^2\theta_o + 8\Omega\sin^3\theta_o x/l_m} - \cos\theta_o)/\sin^2\theta_o} \tag{19}$$

In particular, for the case of normal jet injection, in which $\theta_o = 90^o$, Eq. (18) reduces to

$$\frac{z^2}{l_m^2} - \frac{x}{2\Omega l_m} = 0 \tag{20}$$

or

$$\frac{z}{l_m} = \sqrt{\frac{x}{2l_m\alpha + 2l_m\beta/R}} \tag{21}$$

which is exactly the same result as given by Forney and Kwon [3]. As pointed out by Forney and Kwon [3], although Eq. (21) is restricted to the condition $x/l_m \ll 1$, i.e., valid for the region close to the orifice, a numerical solution obtained by Hoult and Weil [7], indicates that the range of validity of Eq. (21) can be extended away from the orifice, and there are no significant deviations between the approximate result and the numerical result until $x \gg l_m$. For the general case of the present problem, further numerical computation will be needed to confirm the claim that Eq. (18) can be extended away from the near field region where $x/l_m \ll 1$.

2.4 Impact on the Opposite Wall

In chemical engineering, it is assumed that optimal mixing and reaction take place when the issued jet impacts the opposite wall, while in the paper industry, in order to minimize the pressure pulsation and flow disturbance in the approach flow system, it is desirable to avoid having the jet impact on the wall. Therefore, the following estimate of those conditions under which the jet trajectory will intercept the wall, i.e., the conditions under which there exists a solution of Eq. (16) yielding an x for $z = D$, plays an important role in the design of pipeline mixers.

From Eq. (16), by substituting $z = D$, we obtain the arc length s from the start point to the first intercept point with the opposite wall,

$$s = \frac{\sin\theta_o - \sqrt{\sin^2\theta_o - 4D\Omega\sin\theta_o\sin 2\theta_o/l_m}}{2\Omega\sin\theta_o\sin 2\theta_o/l_m} \tag{22}$$

The corresponding intercept coordinate x_i is then calculated using Eq. (17). Of course, the existence of such a solution requires that

$$R\frac{d}{D}\sin^2\theta_o \geq 8\cos\theta_o\Omega \tag{23}$$

where the equal sign yields the critical jet injection angle at which the impact on the opposite wall will happen.

From Eqs. (16) and (17), we also obtain

$$x \sin \theta_o - z \cos \theta_o = 2\Omega \sin^2 \theta_o s^2 / l_m \tag{24}$$

Therefore, we may conclude that $x_i > D\text{ctan}\theta_o$, which is consistent with the fact that the nearest possible position at which the jet can impact the opposite tube wall is $D\text{ctan}\theta_o$, when the tube ambient fluid velocity $v = 0$.

2.5 Correlation of Data

The solutions of the two parametric equations for the asymptotic jet trajectory Eqs. (16) and (17) are plotted and compared with the experimental data of Maruyama et al. [8] [9]. The comparison with seven branch angles covering the range from $30^o \sim 150^o$ is shown in Fig. 2. The tangential and normal entrainment coefficients, which are the so-called universal constants, are chosen as $\alpha = 0.11$, $\beta = 0.6$ [7].

The experimental data represent hot-wire anemometer measurements of maximum jet velocities and, in this case, may not represent the geometric center of the jet. Nevertheless, the correlation is good for branch angles $\theta_o \leq 90^o$ while the asymptotic solutions deviate significantly from the measured data for $\theta_o > 90^o$. In the latter case, the jet is projected upstream and turns abruptly near the origin, and the assumption of small deviation of θ from θ_o is violated. The fact that in all branch angle cases the predicted trajectories match with the experimental measurements near the injection point reflects the assumption we use in deriving the parametric equations (16) and (17).

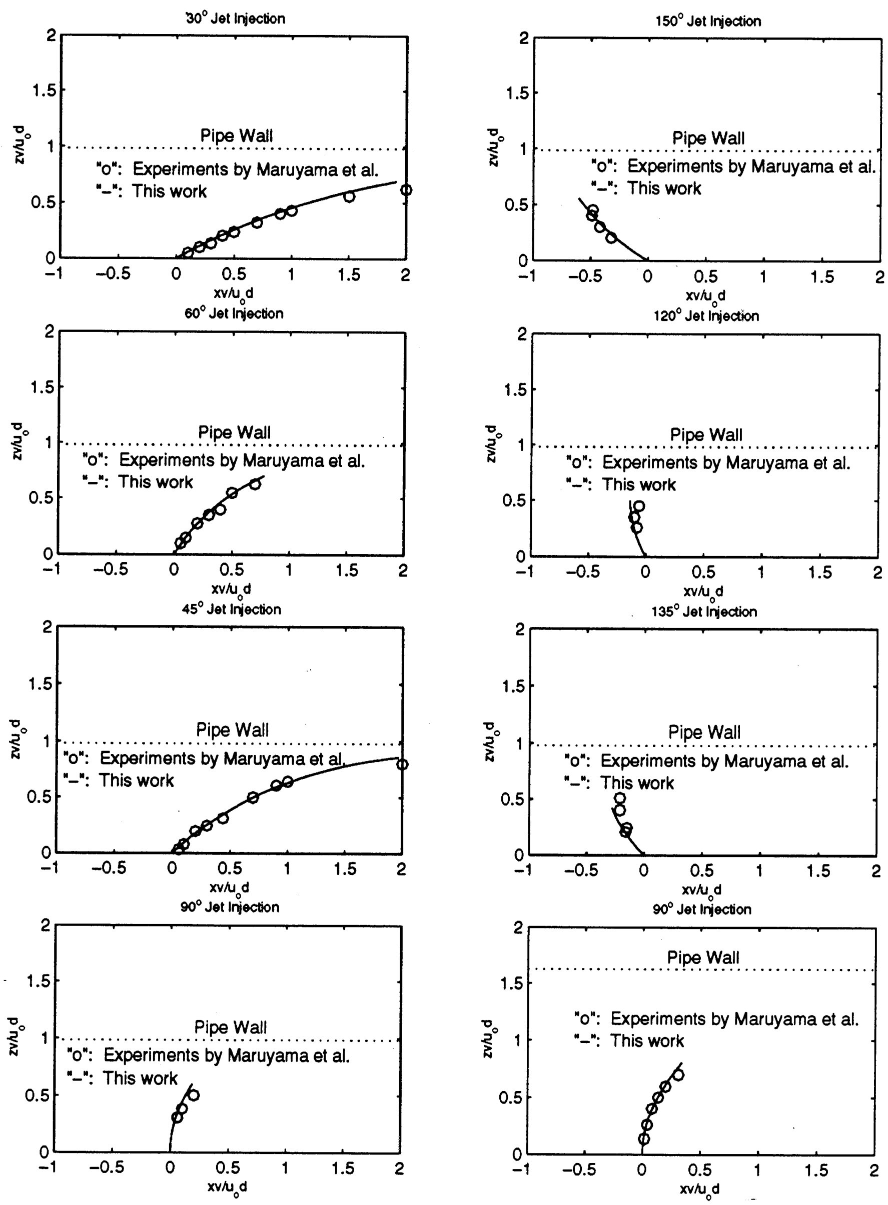

Figure 2: Mixing stream trajectories at different angles. For the bottom-right case, $d = 0.8$ cm, $D = 5.1$ cm, $R = 3.9$; For the other cases, $d = 1.3$ cm, $D = 5.1$ cm, $R = 4.0$.

3 Conclusion

The problem of a turbulent jet in a crossflow at an arbitrary injection angle is studied analytically. By employing the entrainment model and exploring the conservation equations of mass, momentum, and tracer, we derived asymptotic solutions for jet trajectory and tracer concentration of a region close to the jet injection point under the assumptions of a near region where ambient turbulence on the mixing process can be neglected relative to jet-induced turbulence. The proposed asymptotic solutions match well with the existing experimental data. In addition, a critical jet injection angle estimate is also presented.

References

[1] T.H. Chilton and R.P. Genereaux. The mixing of gases for reaction. *AIChE Transaction*, 25:102–122, 1930.

[2] S.D. Fitzgerald and E.R. Holley. Jet injections for optimum mixing in pipe flow. *Journal of Hydraulic Division of ASCE*, 107(HY10):1179–1195, 1981.

[3] L.J. Forney and T.C. Kwon. Efficient single-jet mixing in turbulent tube flow. *AIChE Journal*, 25(4):623–630, 1979.

[4] L.J. Forney and H.C. Lee. Optimum dimensions for pipeline mixing at a T-junction. *AIChE Journal*, 28(6):980–987, 1982.

[5] A.M. Ger and E.R. Holley. Comparison of single-point injections in pipe flow. *Journal of the Hydraulics Division of ASCE*, 102(HY6):731–746, 1976.

[6] D.P. Hoult, J.A. Fay, and L.J. Forney. A theory of plume rise compared with field observations. *Journal of the Air Pollution Control Association*, 19(8):585–590, 1969.

[7] D.P. Hoult and J.C. Weil. Turbulent plume in a laminar cross flow. *Atmospheric Environment*, 6:513–531, 1972.

[8] T. Maruyama, T. Mizushina, and F. Watanabe. Turbulent mixing of two fluid streams at an oblique branch. *International Chemical Engineering*, 22(2):287–294, 1982.

[9] T. Maruyama, S. Suzuki, and T. Mizushina. Pipeline mixing between two fluid streams meeting at a T-junction. *International Chemical Engineering*, 21(2):205–212, 1981.

[10] L.M. Sroka and L.J. Forney. Fluid mixing with a pipeline tee: Theory and experiment. *AIChE Journal*, 35(3):406–414, 1989.

FUNDAMENTALS OF

HEADBOX AND FORMING HYDRODYNAMICS

STATUS REPORT

FOR

PROJECT F005

Cyrus K. Aidun (PI)
Paul McKay
Xiao-Liang Ye

March 23-24, 1998

Institute of Paper Science and Technology
500 10th Street, N.W.
Atlanta, Georgia 30318

DUES-FUNDED PROJECT SUMMARY

Project Title:	Fundamentals of Headbox and Forming Hydrodynamics
Project Code:	FORM
Project Number:	F005
PAC:	Papermaking
Division:	Engineering
Project Staff	
Faculty/Senior Staff:	C. Aidun
Staff:	P. McKay, S. Ye
FY 97-98 Budget:	$147,000
Allocated as Matching Funds:	
Time Allocation	
Faculty/Senior Staff:	25%
Support:	75%
Supporting Research	
M.S. Students:	A. Vorakunpinij
Ph.D. Students:	C. Park
External:	

RESEARCH LINE/ROADMAP: Paper Machine Productivity and Quality.

Improving Paper Machine Productivity and Product Quality Through Headbox and Forming Section Analysis, Modifications, and Application of New Control Systems.

PROJECT OBJECTIVE:

The objectives of this project are to:

(1) Better understanding the paper and board forming processes

(2) Develop novel methods for analysis and control of paper forming

(3) Develop more effective headbox design and paper forming procedures

PROJECT BACKGROUND:

Scope:

Based on the Headbox & Paper Forming questionnaires, the top three issues of importance are:

i. CD nonuniformities (basis-weight, streaks, fiber orientation, moisture, filler and fines distribution ...)

ii. Enhance CD properties (stiffness), ring-crush, STFI, ...

iii. Understand and improve formation (fiber dispersion in the headbox and on the forming wire, ...)

The long-term issue of importance is:

iv. Design an optimized headbox and forming section

Tasks completed during 1996-97:

1. Fix the IPST paper machine for high-speed flow visualization studies of the flow in the headbox and the jet/wire interaction
2. Design a generic headbox (G1) for the IPST pilot paper machine
3. Construct a computational model of the generic headbox
4. Install a narrow section of a commercial headbox (G2) in the CE Hydraulics Lab for laser Doppler velocity and turbulence measurements
5. Fabricate and install the G1 headbox on the IPST machine
6. Prepare a set of guidelines for achieving good fiber orientation (will be complete by the Spring PAC meeting)

Progress toward goals:

1. A flow loop has been constructed for measuring the pressure drop across individual tubes as a function of the flow rate. This flow loop is also being used to evaluate the new tubes with spiral fins that are under development using water.
2. The laser-Doppler velocimeter (LDV) measurements of the streamwise velocity component through the new tubes are complete. These measurements provide the streamwise velocity profile of the flow and the effect of swirl on the streamwise flow characteristics. These measurements need to be repeated with an upgraded LDV system to measure the azimuthal velocity component as a function of the spiral fin pitch and flow rate (Swirl number).
3. Computational prediction of the streamwise velocity component of the flow in individual tubes has been completed, and the results show good agreement with the LDV measurements.
4. Preliminary LDV measurements of the velocity profile in the converging zone of the G1 Headbox have been completed (Xulong Fu, MS project). These measurements need to be repeated at higher flow rates with an upgraded LDV system to measure the secondary velocity field in the headbox.
5. The LDV system for the G2 headbox has been installed. The measurements with and without the sheets (vanes) inside the headbox have been completed.

SUMMARY OF RESULTS:

The details of the results are provided in an annual report for this project. In this section, we simply summarize the results and their applications.

Immediately applicable results:

1. Methods to quantify and compare the results from high-speed digital imaging and image analysis of various forming sections have been developed. This method can be used as a diagnostics tool for characterization of the forming section. Application to four headboxes with different design features shows that the structure of the forming jet depends strongly on the flow properties inside the headbox. For example, the forming jet from headboxes with the extended sheets from the tube block shows a completely different structure compared to those from the headboxes without the

sheets. It appears that the sheets reduce the size of the turbulent eddies as well as the turbulent kinetic energy inside the headbox.

2. A method based on one-dimensional cross-correlation of the high-speed digital images of the forming layer has been developed and tested for surface velocity measurement of the forming jet. This method provides more accurate measurement of the forming jet velocity. The preliminary results show that there is considerable streamwise velocity variation on the jet surface. Current results show that the velocity profile does not have a correlation with the streaks. Further refinement of the procedure, including the hardware and extension to on-line analysis of the images and velocity measurements, are planned for the next six months.

3. The flow characteristics in a headbox with and without the sheets have been examined and compared with accurate measurements of the mean velocity as well as the turbulent fluctuations using an LDV system. The results show that the role of the sheets is to reduce the scale of turbulence as well as reduce the turbulent kinetic energy.

RESULTS

The results are presented in this section with additional detail. The focus is on characterization of the forming jet and the headbox hydrodynamics. The first section outlines a method based on one-dimensional cross-correlation of the digital images to obtain the surface velocity profile of the forming jet. This method provides more accurate measurement of the forming jet. The second section outlines the results from LDV measurements of the velocity field and turbulent fluctuations inside a headbox with and without the Lexan sheets.

I. VELOCITY PROFILE OF THE FORMING JET

Undergraduate Intern: Matthew Montminy

The forming jet velocity profile can have a significant impact on the physical properties of paper. In particular, the hydrodynamics of streaks on the forming table can strongly influence the small-scale physical characteristics of the product [2]. In order to study the details of the forming hydrodynamics, measures of the surface velocity profile are required. Laser Doppler Anemometry (LDV) is a useful technique, but it is limited in that it can only produce data for one physical point at a time, and it cannot be used to analyze fiber suspension flows. Other methods use point correlation to measure the surface velocity at a point. In this section, we outline a method to obtain the surface velocity profile for a section of the forming jet.

This method involves cross correlation of subsequent high-speed digital images to determine the surface velocity profile of the forming jet. Use of cross-correlation methods to obtain velocity field is not a new practice. Cross-correlation flow meters [3] and Particle Image Velocimeters (PIV) are well established methods. The PIV, in particular, is a powerful method for velocity field measurements [4]. This method, however, is limited to transparent fluids with well-defined seeded particles. The fiber suspension in the headbox and the forming section is not transparent and, therefore, not accessible by PIV methods.

This paper describes a simple method that has been used to measure the two-dimensional surface velocity profile of the forming jet. It takes advantage of the nonuniform patterns on the surface of the forming jet, recording the positions of the patterned structures using a high-speed digital camera and using cross-correlation techniques to produce a jet velocity profile.

In order to analyze the hydrodynamics of the forming table, a high-speed digital imaging system is used for high-resolution imaging of the forming jet as it leaves the headbox. The individual gray scale images, or frames, taken 1 msec apart, are digital images of 384 x 512 pixels.

Camera orientation is very important to the success of this method. It is important that the camera be positioned normal to the forming table. If the images are from a different angle, velocity measurements would have to be adjusted and projected on the coordinate axes to account for the view angle. Furthermore, the camera must be angled so that the mean flow is in a north/south or east/west direction within the images produced. This will facilitate the line-by-line cross-correlation method described below. Samples of digital images are shown in previous publications [2].

These sample images show the type of data obtained by the digital camera. The camera picks up the detailed surface features of the forming jet. These features include turbulent patterns as well as mean flow streaks, crests, and troughs in the surface of the fluid. The movement of these patterns during the 1 msec time lag between frames cross-correlated to estimate the forming jet surface velocity profile.

In order for this method to be most effective, the images must have strong contrast with well-defined features. The original images may or may not have sharp contrast, depending on the lighting situation, the pattern of the forming jet, and other surrounding conditions. To account for this, contrast is enhanced using image analysis procedure [5]. Then, two subsequent frames are compared to see how far the features of the image move during the 0.001 sec interval between exposures. This program outputs a scalar value for the streamwise surface velocity component of the forming jet.

Figure 1a shows two subsequent digital photographs of a section of a forming jet. Notice that the second image is very similar to the first, with the surface features shifted slightly to the left. The cross-correlation method takes advantage of this similarity by comparing the two images. It determines the distance that the features of the second image have been shifted relative to the first. This distance, the "lag", is then divided by the time elapsed between exposures to provide an estimate for the jet velocity profile.

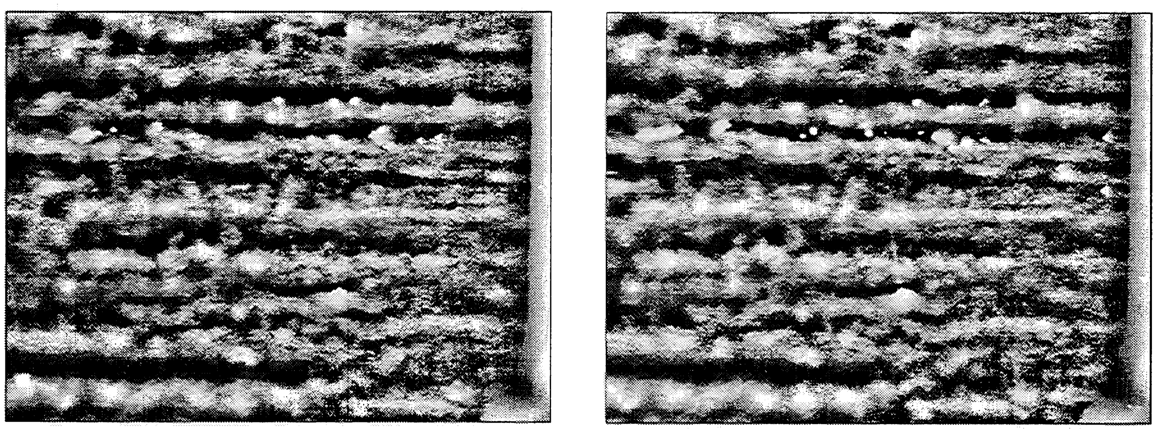

Figure 1a. Digital images of the turbulent flow on the forming table, taken 1 msec apart. The machine direction is from right to left, and the photograph on the left is taken first. Notice the patterns due to turbulence superimposed on the mean streak patterns within the images. This method uses patterned features in the images to estimate the surface velocity profile of the forming jet. Each image represents a 4.7" x 6.3" region of the forming table.

The features are compared via analysis of the gray scales, or light intensities, of the digital images. The signals compared in this method are the gray scale values of bands of pixels aligned in the machine direction. Since this is the direction of mean flow, almost all of the motion occurring during the lag between the two frames occurs in this direction. Figure 1b shows an example of these bands.

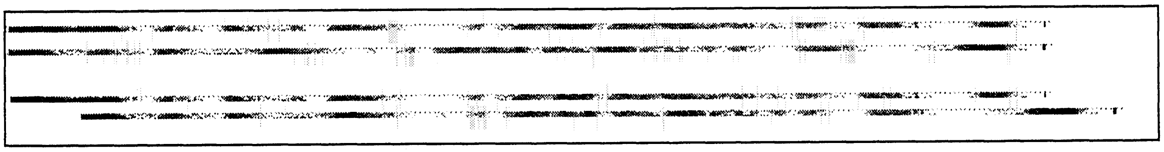

Figure 1b. The top two lines are line segments from the two digital images similar to those used in the cross-correlation program. At the bottom, the two images are lined up according to their respective gray scale values. The displacement of the bottom line is equal to the lag, or the distance the line of fluid has moved within the 1 msec time interval between exposures.

Gray scale intensities are converted to numerical values, and a FFT one-dimensional cross-correlation is carried out. If bands running the entire width of the image are used in the cross-correlation, an average jet velocity profile can be generated. This profile describes the jet velocity as a function of the location in the cross-machine direction. An average jet velocity profile generated for the case shown in Figure 1a and 1b is given in Figure 1c.

The trendline shown in Figure 1c is a five-point moving average of the raw data produced by a cross-correlation routine. This graph shows the type of data that can be obtained via line-by-line cross-correlation of the entire image. One-dimensional cross-correlation can also be used to determine the local jet velocity at most points along the machine and cross-machine directions. This is done by choosing a different interrogation area. Instead of the entire bands used to determine the average velocity profile, subsets of these bands are used to determine local jet speeds.

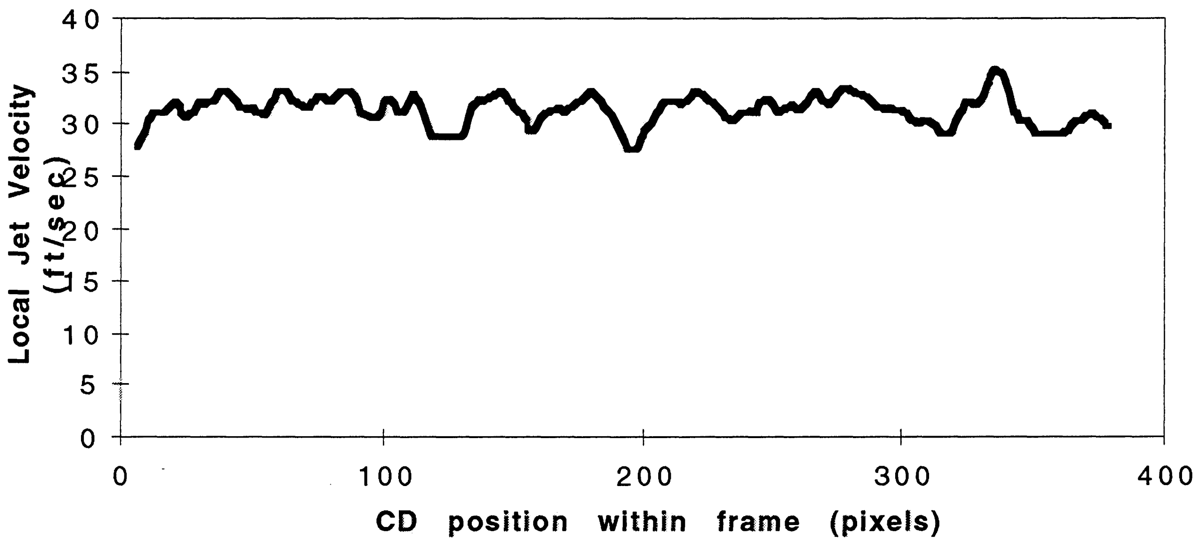

Figure 1c. Average forming jet velocity profile determined by line-by-line cross-correlation.

To map the local jet speed profile of the forming jet, interrogation bands 64 pixels long, aligned along the mean flow direction, are defined. These interrogation bands are centered on each pixel of the image. Corresponding interrogation bands (bands centered at the same pixel location) from the two subsequent images are cross correlated. The location of the correlation peak specifies the distance that the fluid surrounding the point has moved between exposures. As the time interval between the two images is known, the data can be used to calculate the local velocity of the forming jet.

The 1-D cross-correlation method, outlined above, does not provide the value of velocity for every point in the image. Since each interrogation band is 64 pixels long, and the local velocity at each pixel is determined by centering such a band at the pixel, velocity values for areas to the extreme right and left of the image (within 32 pixels of the edge) are not available.

With the interrogation band length of only 64 pixels used in this method, small inconsistencies between the two images can cause relatively large errors. Even in the small time frame of 0.001 sec, many of the turbulent patterns within the digital frames may be distorted. For this reason, an estimate of the average jet velocity based on the total flow rate at the opening of the slice is used in the program, along with a set of user-defined tolerance values.

The tolerance of the program is left to the discretion of the user. If the correlation peak is not within the allowed parameters, it is discarded. More details on this method are provided in the annual report.

II. EFFECT OF FORMING SHEETS ON HYDRODYNAMICS

Co-investigators: P.J.W. Roberts and A. Kovacs

Two sets of experiments were done to measure velocities at the jet exit and in the headbox. Both sets of experiments were done with and without the guide sheets in place. All measurements are at a flow rate of 50.5 L/sec ±3% (800 gpm) with a slice opening of 12.7 mm (0.5 inch). The headbox width is 406 mm (16 inches), so the average jet velocity at the exit is 9.8 m/sec. The headloss in the headbox is somewhat higher with the sheets than without.

Measurements at the Jet Exit:

Vertical profiles of the variation of the horizontal streamwise, u, and cross-flow velocity, v, at the jet exit were made at five horizontal locations as shown in Figure 3. The horizontal locations were at y = 2, 4, 8, 12, and 14 inches. The vertical coordinate, z, of the point of measurement is the distance from the Lucite attached to the lower surface of the slice. The laser probe is placed below the Lucite looking upwards as shown in Figure 2. Three measurements were recorded at each location. Data were obtained both with the separating plastic sheets inside the headbox and with them removed.

The mean streamwise and cross-flow velocities are shown in Figures 4 and 5. Typical streamwise velocities are greater then the average velocity at the jet exit due to the vena contracta effect. It can be seen that the streamwise velocity is not exactly uniform. The variation of velocity over the cross section is about 3% of the mean value. Without the sheets, the variation is almost 10%. The results also imply some asymmetry of the flow about the jet exit centerline. The flow closer to the headbox inlet (y = 14 inches) is less uniform than farther away (y=2 inches).

The cross-flow velocity is very small, essentially zero, with the sheets installed, implying essentially straight streamlines parallel to the headbox axis with negligible secondary circulations. The magnitudes are substantially higher without the sheets. For this case, the velocities are generally negative to the left of the headbox centerline and positive to the right. This implies diverging flow to the headbox walls. At the far wall (y = 14 inches) especially, the velocities are negative near the free surface and positive near the middle and lower boundary. This implies a rather strong secondary circulation within the jet, which is suppressed by the sheets.

The streamwise and cross-flow variations of turbulence intensity (proportional to the normal Reynolds stresses) are shown in Figures 6 and 7. They are shown as the magnitude of the root mean square (rms) value of the velocity fluctuations about the local mean value.

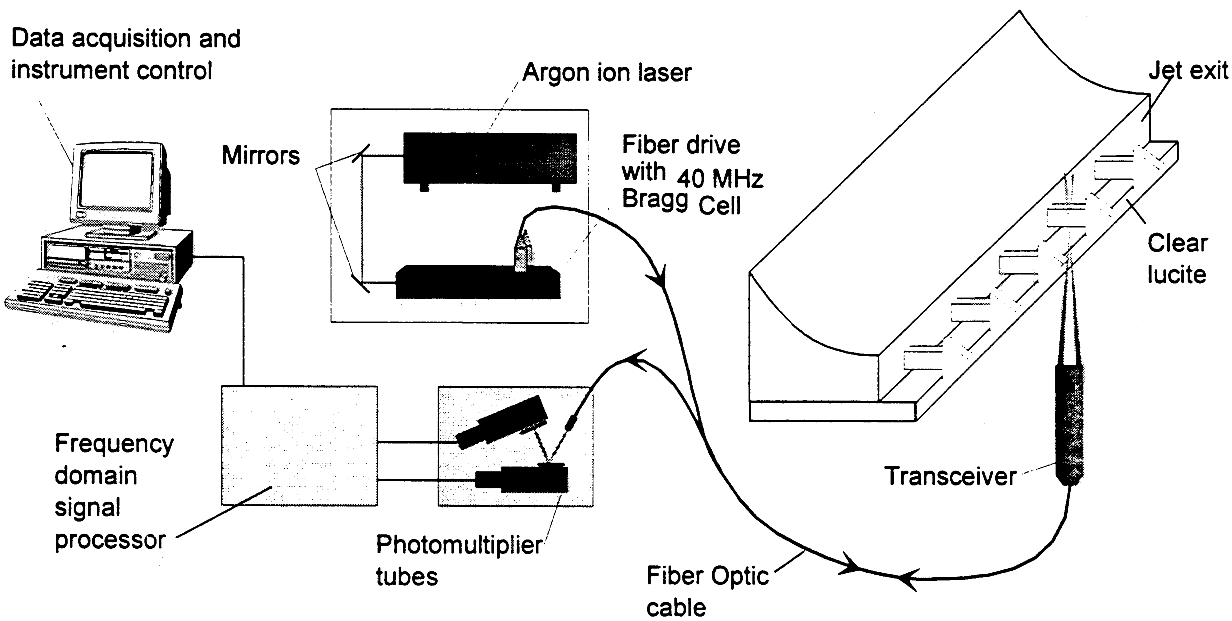

Figure 2. Schematic Depiction of LDV Experimental Configuration

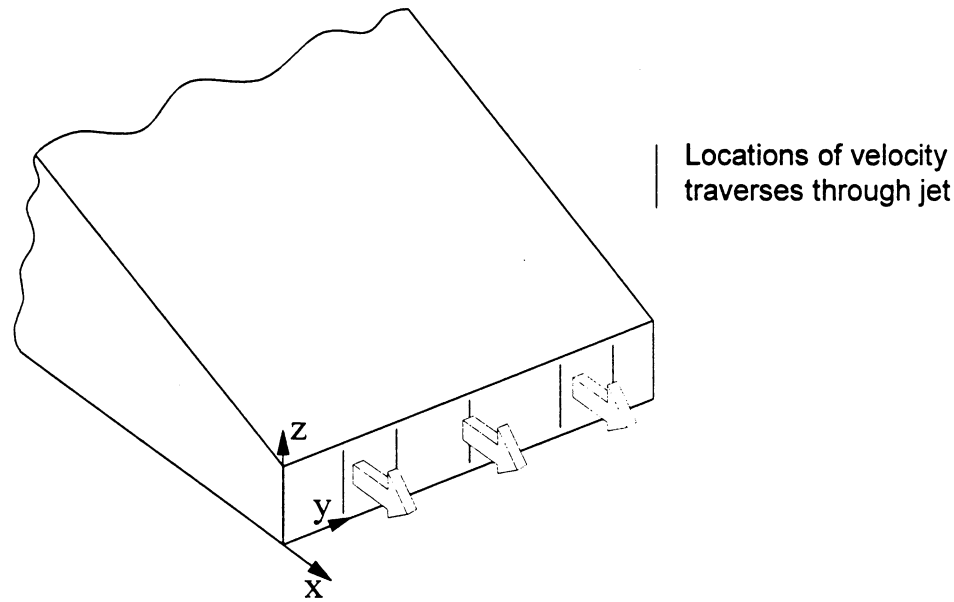

Figure 3. Coordinate System Used for Velocity Measurements

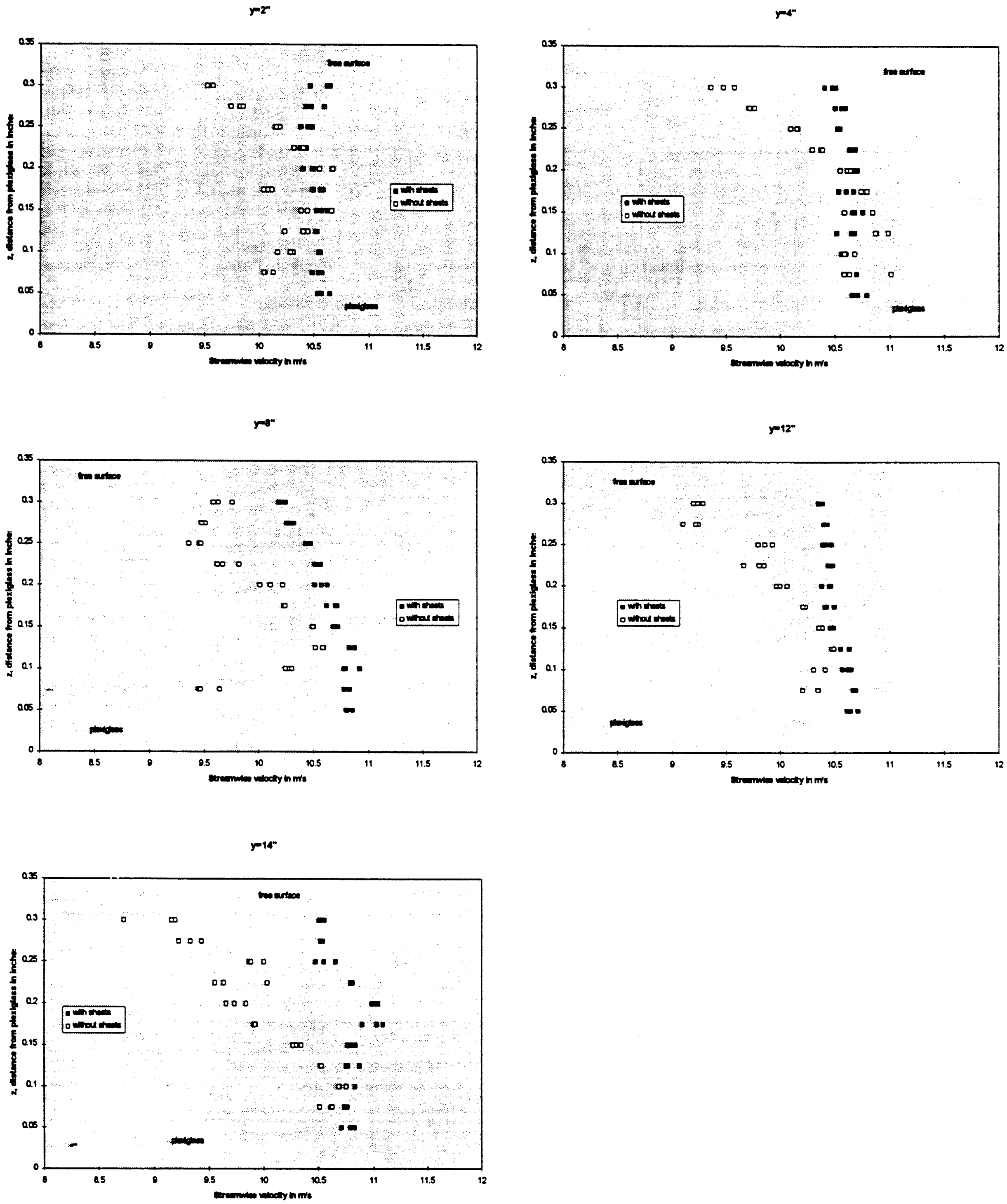

Figure 4. Mean Streamwise Velocity, u at the Jet Exit. With and Without Sheets.

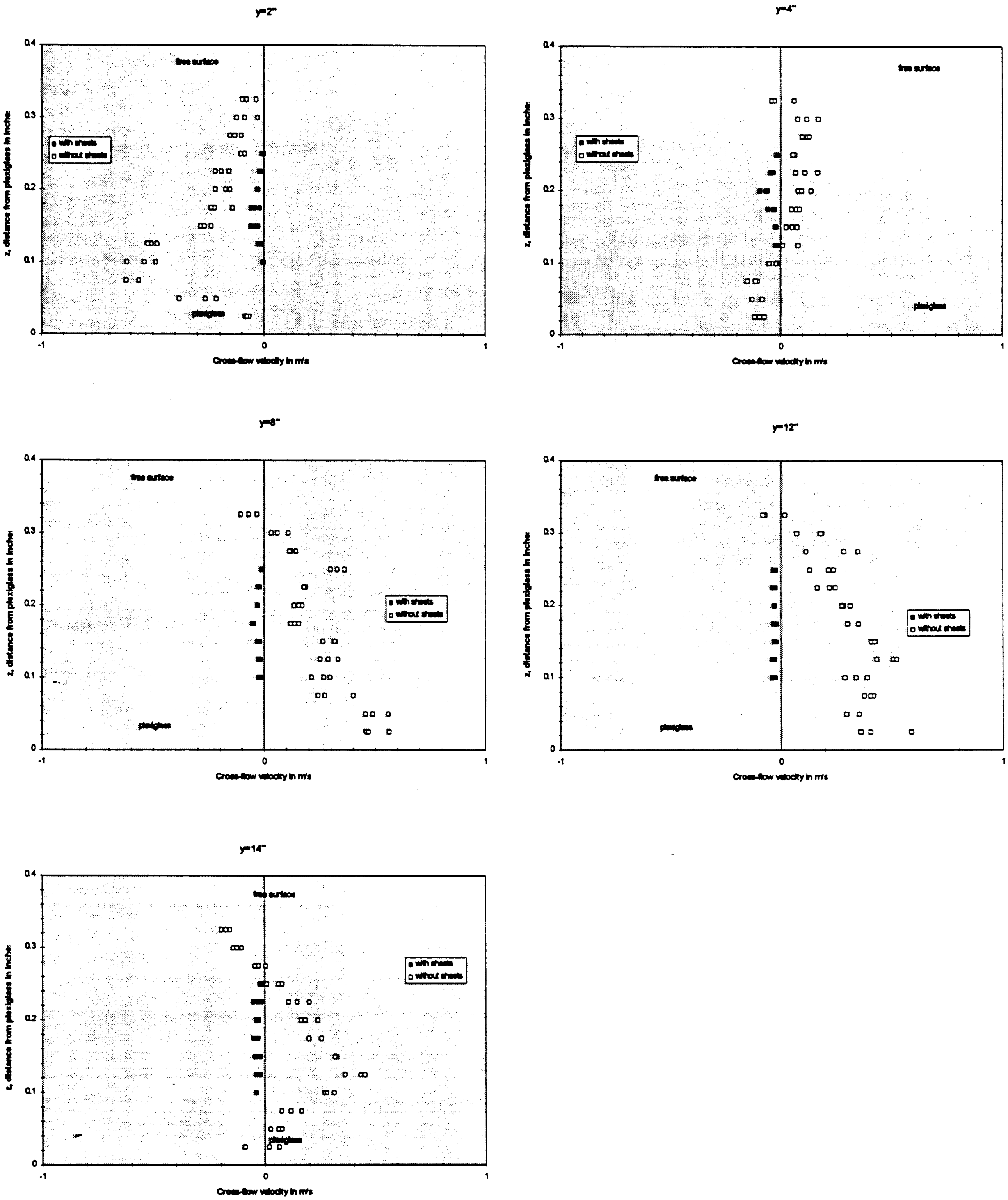

Figure 5. Mean Crossflow Velocity, v at the Jet Exit. With and Without Sheets.

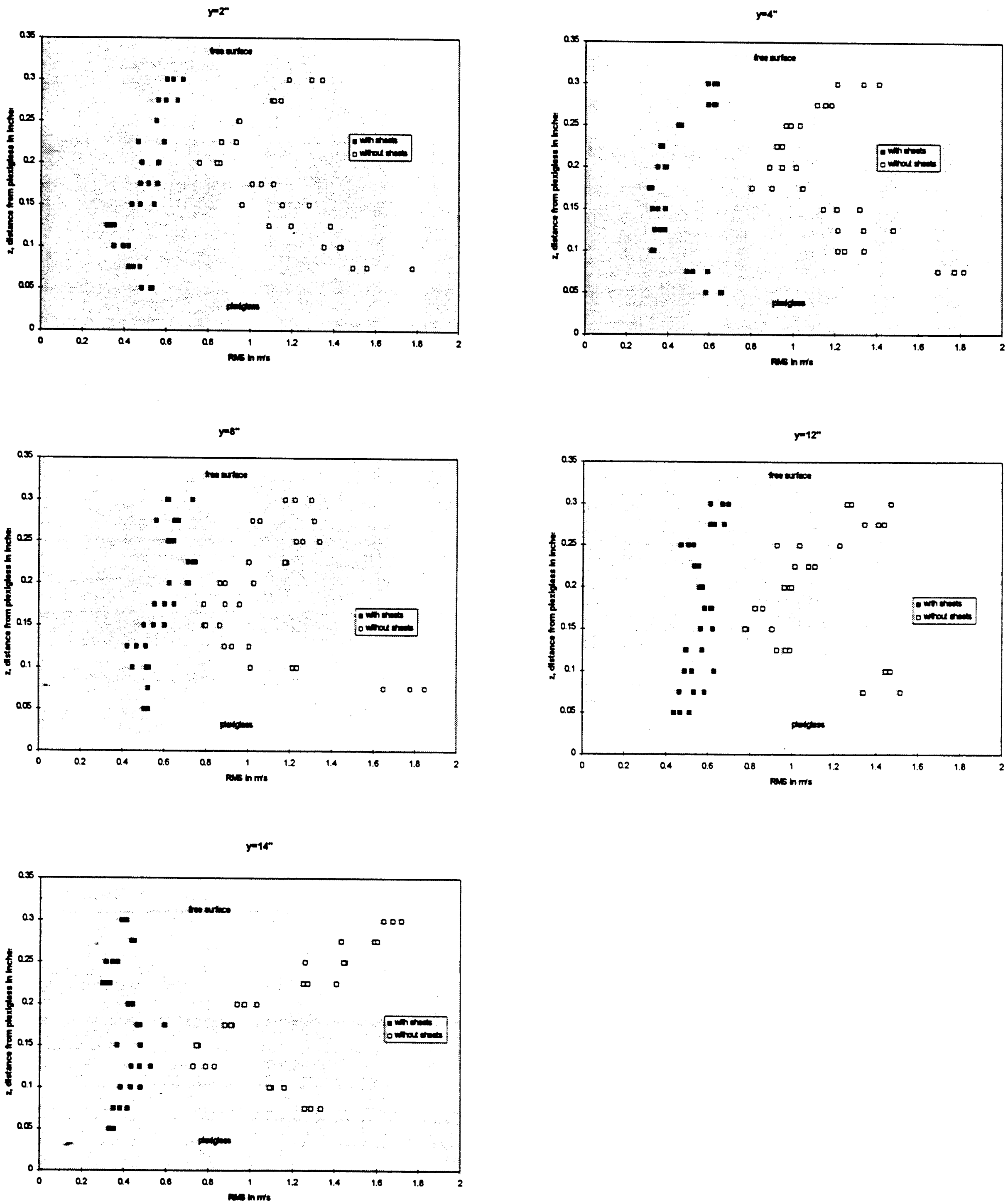

Figure 6. rms of Streamwise Velocity, u' at the Jet Exit. With and Without Sheets.

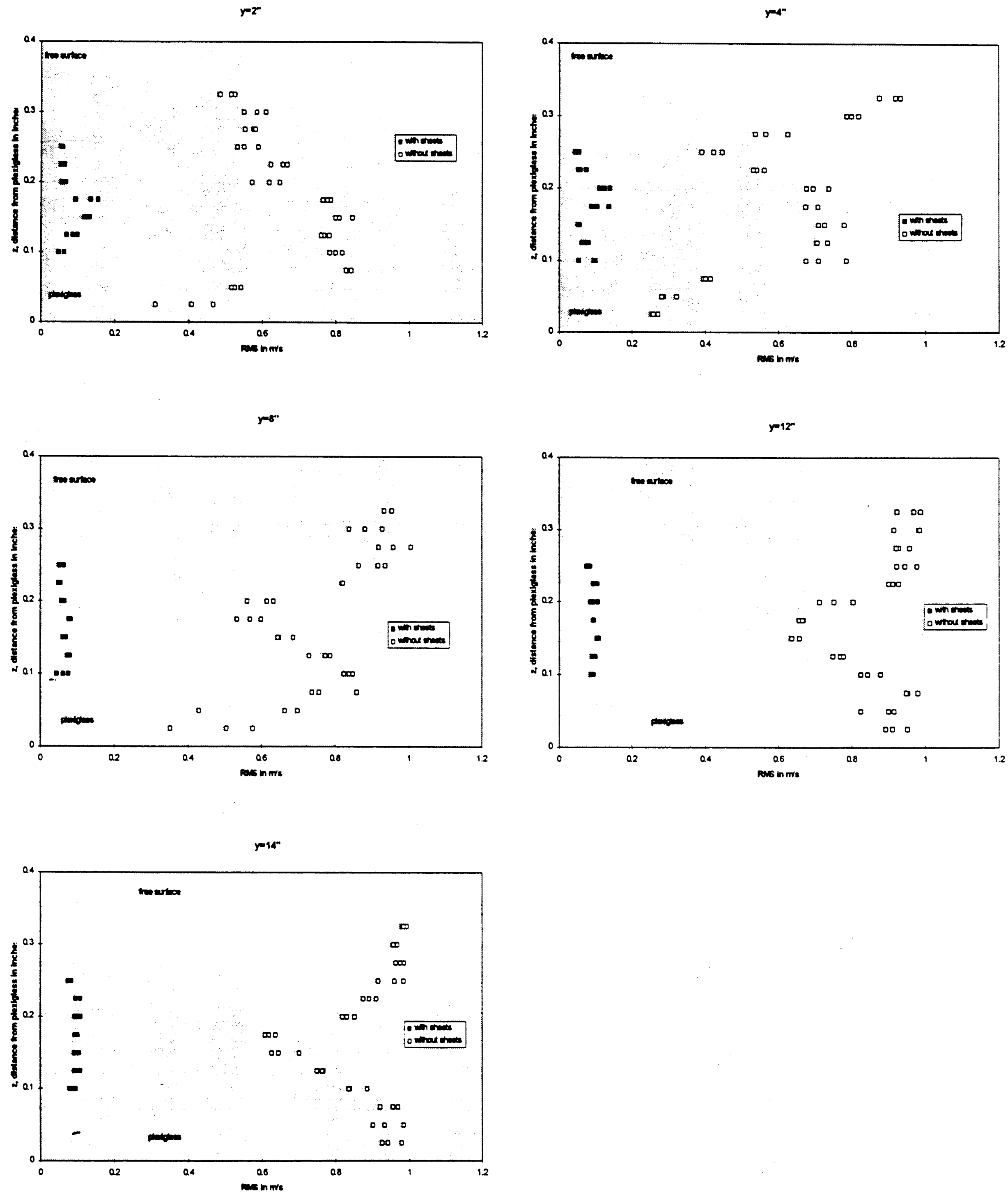

Figure 7. rms Crossflow Velocity, v' at the Jet Exit. With and Without Sheets.

The rms of the streamwise velocity is smaller and more uniform with the sheets than without. Typical streamwise values with the sheets are about 0.3 to 0.6 m/sec, corresponding to relative turbulence intensities of about 3 to 6 %. The crosswise rms values are smaller, indicating that the turbulence is not isotropic. Without the sheets the rms values are higher and less uniform. Streamwise turbulence intensities are typically 10 % or greater and are higher near the lower boundary and at the free surface.

Measurements in the Headbox:

Measurements of the streamwise, u, and vertical velocity, w, were made inside the headbox along the longitudinal axis. The measurements were made at a distance y = 3" from the Lucite wall along the centerline of the headbox. The longitudinal variations of the mean streamwise and vertical velocities are shown in Figure 8.

The streamwise velocity increases along the headbox due to the tapering cross section. Without the sheets the streamwise velocity is larger near the tube and smaller near the slice than with the sheets. With the sheets the velocity increases more uniformly along the headbox. The vertical velocities with the sheets are very small. With the sheets, the vertical velocity is quite strong, up to about 1.8 m/sec near the inlet tube bank. This velocity is positive, i.e., upwards. It is also positive near the jet exit but with a much smaller magnitude, about 0.1 m/sec.

The streamwise rms intensities are smaller with the sheets installed than without them. This is particularly true near to the inlet tube bank, where typical rms values are about twice as large without the sheets. This difference decreases with distance along the headbox until the jet exit, where the rms values are very close.

The relative turbulence decreases rapidly with distance along the headbox. With the sheets, it decreases from about 40 % near the tube bank to about 3 % near the jet exit. The high values near the inlet tubes are presumably due to the shear induced by the individual jets issuing from the tubes. This turbulence decays with distance until, by the jet exit, it has been replaced by turbulence due to shear at the top and bottom boundaries of the headbox, with typical values around 3 %.

Conclusions:

1. The streamwise velocity of the flow leaving the headbox at the jet exit is more uniform with the sheets.

2. The cross-flow velocities are very small with the sheets. This indicates the secondary circulations are virtually eliminated by the sheets.

3. Cross-flow velocities without the sheets can be quite substantial and spatially variable without the sheets. This indicates the presence of secondary circulations.

4. The magnitude of the turbulent fluctuations (expressed as their rms values) are smaller and more spatially uniform over the jet exit with the sheets than without. Relative turbulence intensities over the jet exit are typically about 3 to 6 % with the sheets and are larger without.

5. The streamwise velocity inside the headbox increases more uniformly with the sheets than without them. Vertical velocities in the headbox are essentially eliminated by the sheets but can be quite large without them.

6. With the sheets, the relative turbulence intensity decreases rapidly with distance inside the headbox. It is about 40 % near the inlet tubes and about 3 % near the jet exit. This is presumably due to the decay of the turbulence intensity associated with the multiple inlet jets.

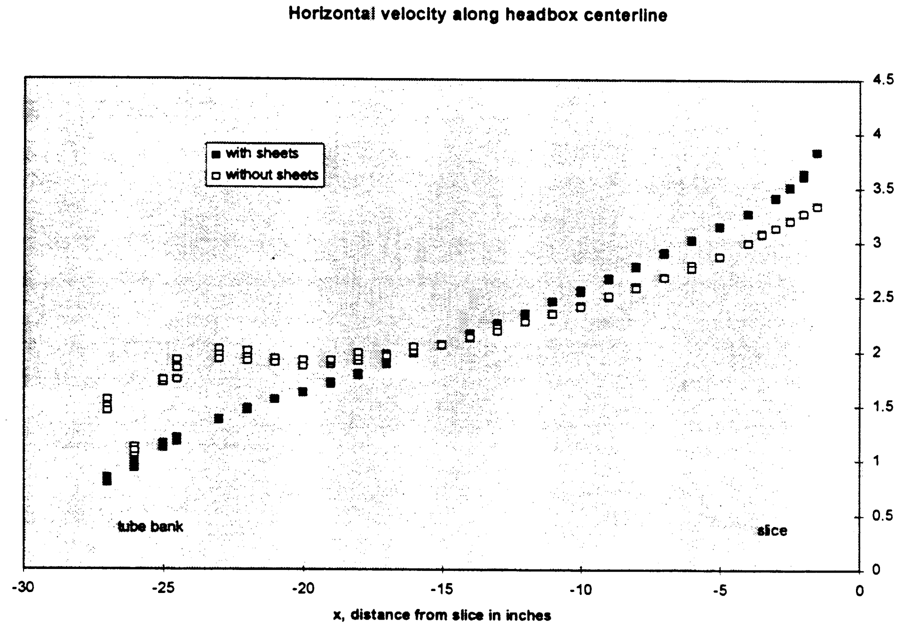

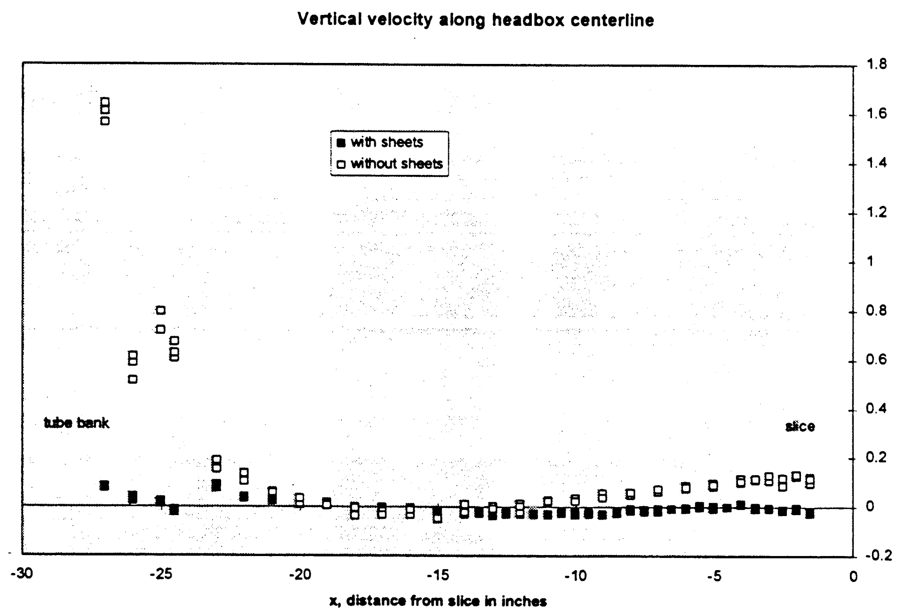

Figure 8. Mean Streamwise Velocity, u, and Vertical Velocity, v, Along Headbox Centerline

RMS of horizontal velocity along headbox centerline

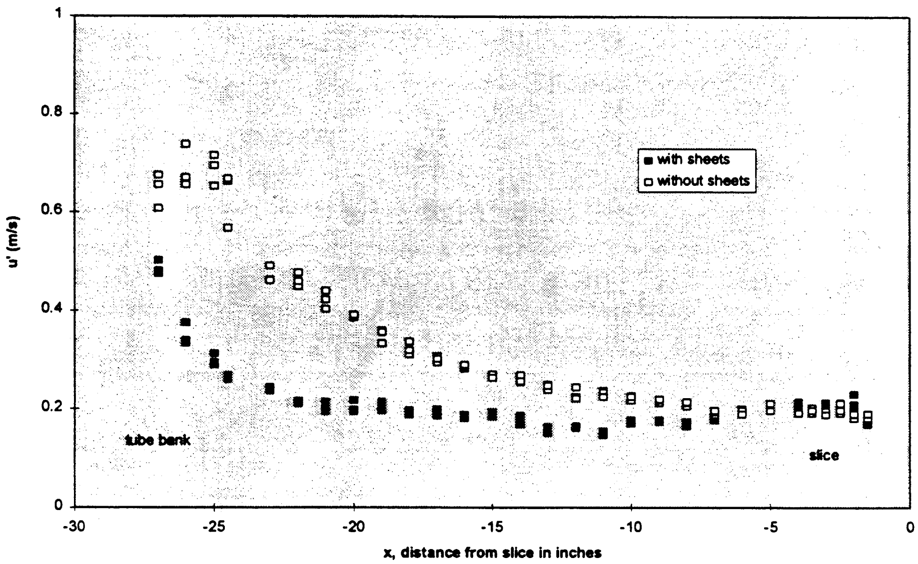

RMS of vertical velocity along headbox centerline

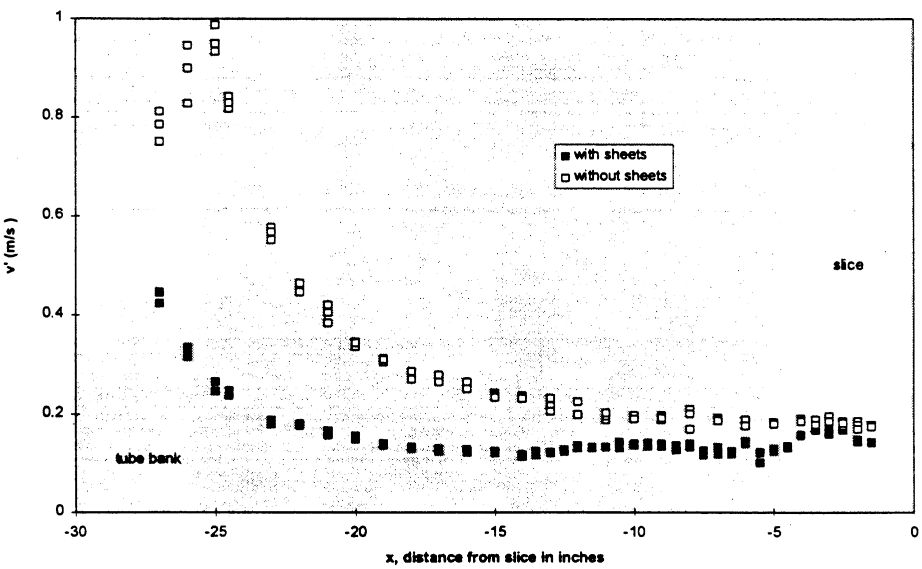

Figure 9. rms Streamwise Velocity, u', and Vertical Velocity, v', Along Headbox Centerline

References:

1. Aidun, C. K. "A Fundamental Opportunity to Improve Paper Forming". *Tappi J.*, June 1996, 55-59.
2. Aidun, C. K. "Hydrodynamics of Streaks on the Forming Table". *Tappi J.*, Vol. 80, No. 8, 155-62, 1997.
3. Beck, M. S. "Correlation in instruments: cross correlation flowmeters". *J. Phys. E. Sci. Instrum.,* Vol 14, 1981, *pp. 7-19.*
4. Frigerio, F., and Hart, D. P. "Velocity Field Measurements of a Confined Swirling Flow Using Digital Particle Image Velocimetry Cinematography." *1997 ASME Fluids Engineering Division Summer Meeting,* June 22-26, 1997.
5. Aidun, C. K., and Ferrier, C. A. "High-Speed Digital Imaging of Paper Forming: A Method for Qualitative evaluation of Paper Forming Hydrodynamics". *Joint TAPPI Engineering / Papermakers SuperConference,* Oct. 5-9, 1997; and to appear in *Tappi J.*, 1998.

GOALS FOR FY 98-99:

1. Determine the flow characteristics (turbulent Reynolds stress) in the tube section and the converging section of the headbox and the effectiveness of each section in floc dispersion.
2. Apply the cross-correlation surface velocimeter to determine the impact of the jet velocity variations on small-scale fiber orientation nonuniformity in the sheet.
3. Explore methods to measure the jet velocity profile in ZD.

DELIVERABLES:

1. Annual report for the 1997-98 fiscal year.
2. The quantitative measure of floc dispersion resulting from step diffusor tubes at various flow rates.
3. The impact of the convergence angle on floc dispersion through the converging channel of the headbox.
4. Measurement of the turbulent Reynolds stress in the tube section and in the converging section of a headbox using a two-component LDV system.
5. Annual report for the 1998-99 fiscal year.

Immediate application of the deliverables listed above:

1. It is widely reported that the tubes in the headbox destroy flocs that exist in the manifold. The study noted as deliverables 2 and 3 examines this claim using flow visualization and detailed measurements of the flow characteristics in the tube section and the converging section of the headbox. Various types of fiber flocs will be used to examine the impact of the tube section on fiber dispersion at various flow rates. The acceptable window of operation in the parameter space will be outlined. This information can be used in the mill to compare the operating parameter of member company's headbox with the range of effective floc dispersion in the tube section. The potential improvement in formation for a machine can be evaluated with this comparison.

2. The true characteristics of the turbulent flow can be obtained by examination of the Reynolds stress components in the flow. The only method to measure this quantity is with a two-component LDV system. This information along with the results from the characterization of the floc dispersion mechanism, will provide insight into the effectiveness of various flow conditions in terms of formation. This study should also be extended to the forming section.

SCHEDULE:

```
Month =>July Aug.   Sept.  Oct.   Nov.   Dec.   Jan.   Feb.   March  April  May    June

ITEM

1. Report --|
2. Step Tube -----------------------------------------------------------|
3. Conv. Nozzle                      ------------------------------------------------------------------|
4. Reynolds Stress  ---------------------------------------------------------------------------------------|
5. Annual Report for 1998-99                                                                  ----------|
```